Vibration excitation of axial compressor rotor blades

by

Gert Raubenheimer

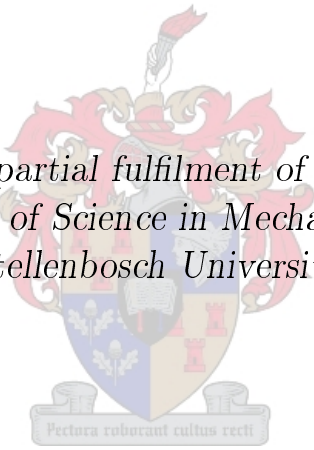

Thesis presented in partial fulfilment of the requirements for the degree of Master of Science in Mechanical Engineering at Stellenbosch University

Department of Mechanical and Mechatronics Engineering,
University of Stellenbosch,
Private Bag X1, Matieland 7602, South Africa.

Supervisors:

Mr. S.J. van der Spuy
Prof. T.W. von Backström

July 2011

Declaration

By submitting this thesis electronically, I declare that the entirety of the work contained therein is my own, original work, that I am the owner of the copyright thereof (unless to the extent explicitly otherwise stated) and that I have not previously in its entirety or in part submitted it for obtaining any qualification.

Date: .....

Abstract

Vibration excitation of axial compressor rotor blades

G.A. Raubenheimer

Department of Mechanical and Mechatronics Engineering,
University of Stellenbosch,
Private Bag X1, Matieland 7602, South Africa.

Thesis: MScEng (Mech)

July 2011

Turbomachines are exposed to several environmental factors which may cause failure of components. One of these factors, high cycle fatigue, is often caused by blade flutter. This thesis forms part of a project of the European Seventh Framework Programme (FP7), called project Future. Project Future is doing theoretical and experimental investigation into the occurrence of flutter in turbomachinery. The objective of this thesis was to evaluate the effectiveness of a gas injection system as a means of exciting vibrations on the first stage rotor blades of a compressor. Unsteady simulations of the excitation velocity perturbations were performed in the Computational Fluid Dynamics (CFD) software, Numeca FINE™/Turbo. Experimental testing on the in-house Rofanco compressor test bench, using one prototype of the 15 injector system, provided data that was used to implement boundary conditions and to verify certain aspects of the unsteady simulation results. The simulation results revealed the following: the injector bypass frequency was so dominant that the excitation frequency was hardly detectable in the majority of cases. Furthermore, several secondary frequencies were consistently present. The injector bypass frequency, as well as the secondary frequencies, occurred as a result of the convolution of Fast Fourier Transforms. While the injector bypass frequencies can theoretically be eliminated, it will not be possible to eliminate the secondary frequencies from the blade response. In conclusion, according to the CFD results, it will not be possible to excite a single excitation frequency by making use of a finite number of gas injector vibration exciters.

Uittreksel

Vibrasie-opwekking van aksiaalkompressor rotorlemme

("Vibration excitation of axial compressor rotor blades")

G.A. Raubenheimer

Departement Meganiese en Megatroniese Ingenieurswese,
Universiteit van Stellenbosch,
Privaatsak X1, Matieland 7602, Suid Afrika.

Tesis: MScIng (Meg)

Julie 2011

Turbomasjiene word onderwerp aan verskeie omgewingsfaktore wat falings van komponente kan veroorsaak. Een van hierdie faktore, naamlik hoë-frekwensie vermoeidheid, word onder andere veroorsaak deur lemfladder. Hierdie tesis is deel van 'n projek in die Sewende Europese Raamwerk Program (European Seventh Framework Programme - FP7), projek Future. Projek Future doen teoretiese en eksperimentele ondersoek na die voorkoms van lemfladder in turbomasjienerie. Die doelwit van hierdie tesis was om die effektiwiteit van 'n gasinspuiter vibrasie-opwekkingstelsel te evalueer, deur gebruik te maak van onbestendige simulasie in die berekenings vloei-meganika sagtewarepakket, Numeca FINE™/Turbo. Eksperimentele toetswerk op die plaaslike Rofanco kompressortoetsbank, met 'n prototipe van die 15 inspuiter stelsel, het inligting verskaf wat gebruik is om die inlaattoestande te spesifiseer en simulasieresultate te korreleer. Die simulasieresultate het getoon dat die frekwensie waarteen 'n lem by die inspuiters verbybeweeg, so prominent is, dat dit in die meerderheid van gevalle baie meer prominent is as die opwekkingsfrekwensie. Verder was daar ook deurgaans 'n aantal sekondêre frekwensies teenwoordig. Die teenwoordigheid van die inspuiter verbybeweeg frekwensie en die sekondêre frekwensies is die resultaat van die konvolusie van Vinnige Fourier Transforme. Alhoewel dit in teorie moontlik sal wees om die inspuiter verbybeweeg frekwensie te elimineer, is dit onmoontlik om die sekondêre frekwensies uit die lem vibrasie te elimineer. Ter opsomming, volgens die berekenings vloei-meganika resultate, is dit nie moontlik om met 'n stelsel van 'n eindige aantal inspuiters, 'n enkele vibrasie frekwensie op te wek nie.

Acknowledgements

I would like to express my sincere gratitude to the following people and organisations for their valuable contribution to my MSc project:

Project Future of the European Seventh Framework Programme (FP7), for making this thesis possible through funding and through involving Stellenbosch University as an active participant.

Project Ballast, funded by Armscor and the SA Air Force and managed by the CSIR, for the funding provided for this project.

Mr Johan van der Spuy, my thesis supervisor for facilitating my involvement in all the exciting aspects of Project Future and for his guidance, support and patience throughout the project.

Prof Theo van Backström, my co-supervisor, for his insight, guidance and support throughout the project.

The technical personnel - Mr Cobus Zietsman, Mr Ferdi Zietsman, Mr Anton van den Bergh, Mr Graham Hamerse and Mr Calvin Hamerse for their assistance and invaluable advice during the experimental work.

Mr Glen Snedden and Mr Erik Wegman from the CSIR for their efforts to successfully develop and produce a vibration excitation system of a very high standard.

Mr Andrew Gill for his patience and guidance during the experimental work.

Mr Andrew de Wet for his assistance with the Numeca software and all computer related matters.

Miss Mardelle Schoeman, for her support, patience and assistance throughout the project.

Contents

List of Figures

List of Tables

Nomenclature

Constants

$\pi =$ 3.141 592 654

Variables

A	Area	[m^2]
A_{max}	Maximum amplitude	[ ]
β_∞	Mean velocity angle	[°]
C_a	Axial velocity	[m/sec]
C_L	Coefficient of lift	[ ]
E	Corrected voltage	[V]
E_m	Measured hot wire voltage	[V]
k	Factor of influence	[ ]
L	Characteristic length	[m]
L_{ref}	Reference length	[m]
N	Rotation speed	[RPM]
Ω	Angular velocity	[Rad/sec]
ω	Frequency	[Hz]
ω_n	Natural frequency	[Hz]
ω_0	Natural frequency with blade stationary	[Hz]
r_1	Mid-span radius	[m]
ρ	Density of air	[kg/m^3]
t	Time	[sec]
T_f	Air temperature	[°C]
T_r	Reference temperature	[°C]
T_w	Wire temperature	[°C]
U	Tangential velocity	[m/sec]
$\|u\|$	Absolute velocity	[m/sec]
v	Viscosity	[kg/ms]
VE	Frequency response vector	[mm]

V_f	Flutter speed	[m/sec]
V_{ref}	Reference velocity	[m/sec]
W_∞	Mean relative velocity vector	[m/sec]
W_1	Relative velocity	[m/sec]
x	Coordinate	[m]
y_{wall}	Wall cell width	[m]
Y_1^+	Y-plus value	[ ]
ζ	Damping ratio	[ ]

Chapter 1

Introduction

1.1 Project motivation and description

Turbomachines are exposed to several environmental factors throughout their life cycle, which may lead to failure of components. These factors include erosion, corrosion, thermal fatigue, low cycle fatigue and high cycle fatigue. High cycle fatigue is a major concern and therefore it is essential that this should be addressed during the development phase of a turbomachine. Research has shown that approximately 90% of the potential high cycle fatigue problems are addressed during the developmental testing phase (El-Aini *et al.*, 1997). The remaining 10%, however, accounts for nearly 30% of the total development cost and is responsible for more than 25% of all engine distress events.

The rotating blades of a turbomachine are particularly susceptible to high cycle fatigue. This may be caused by several factors, one of which is blade flutter. Flutter is a self excited oscillation or instability at or close to the blade natural frequency which does not require any disturbance (Cumpsty, 1989). Flutter is more generally defined as the dynamic instability of an elastic body with inertia that is caused by aerodynamic forces (Agenbach, 1991). The effects of blade flutter not only result in long term high cycle fatigue damage, it may also lead to dramatic, often catastrophic blade loss in the short term.

This thesis project was completed as part of a project in the European Seventh Framework Programme (FP7), called project Future. This project is coordinated by the Swedish technical university Kungliga Tekniska Högskolan (KTH), with the involvement of 25 other partners. One of these partners is Stellenbosch University. The aims of Project Future are to do theoretical and experimental investigation into the occurrence of flutter in turbomachinery. This will provide better modelling and design methods to manage the phenomenon of flutter, specifically in the application of aircraft gas turbine engines.

The Project Future Work Description document introduces the motivation for the project as follows:

"Strong international competition is an essential driver for aircraft engine manufacturers to develop new enabling technologies that will allow them to optimize the engine cost of ownership and thus stay competitive by applying trade-offs between engine cost, performance, weight, maintenance and noise. Some of the technologies chosen by designers to fulfil the requirements of the more competitive engine configurations have a strong impact on the aeromechanical properties of components, causing them to become more sensitive to flutter problems. Examples of these technologies and their effect are:

- Higher bypass ratio engines for increased efficiency and reduced noise levels requires longer blade lengths, making the blades more sensitive to flutter.
- Wide chord and three dimensional compressor blade shapes for more compressor power result in complex structures of which the behaviour must be better understood.
- High blade loading due to continued increase in pressure level and Mach number gives stronger aeroelastic forces which makes compressor blades more sensitive to flutter.
- Blisk designs decrease manufacturing cost and lead time, but at the same time become more prone to flutter because they do not have contact surfaces that naturally add to structural damping."

The role of the Department of Mechanical and Mechatronics Engineering at Stellenbosch University (SU) in this project was to demonstrate the ability of a vibration excitation system, developed by the Council of Scientific and Industrial Research (CSIR), to excite a range of vibration frequencies on the first stage rotor blades of an in-house compressor test bench. Upon successful completion of the testing, the system will be shipped to the Technical University of Darmstadt in Germany, where the next phase of the project will be initiated. At the time of writing up this thesis, testing had not yet been completed.

The design of the exciter system that was developed was based on technology employed by the CSIR (Wegman *et al.*, 2009) and the South African Air Force (SAAF) to conduct flutter testing on aircraft. For example, the flutter characteristics of new missile, bomb and external fuel tank configurations for fighter aircraft are tested by introducing vibration into the airframe

by means of a vibration actuator, both during ground tests and during subsequent flight tests. The resulting deflection of the airframe is recorded by means of numerous accelerometers installed at crucial positions on the aircraft. The vibration actuator starts inducing vibration at a relatively low frequency and then sweeps to a high frequency, while the acceleration is recorded and monitored in almost real-time during flight testing. The recorded data can then be processed to determine the damping characteristics of the configuration at various velocities and flight profiles. The damping ratio is an indication of the tendency of the tested configuration to exhibit flutter. A very low damping ratio (approaching zero) at a specific flight regime indicates a high risk that flutter may occur at that point.

The blade vibration excitation system developed by the CSIR was based on the forced vibration frequency sweep technique as described above. The CSIR evaluated several proposed concepts for exciting vibration during the development process of this system. All of these concepts were based on the principle of inducing blade vibration by disturbing the airflow over the blade. A brief description of each will be provided below.

The first excitation concept to be evaluated was a variable pitch stator vane system. The concept involves installing a set of variable pitch inlet guide vanes upstream of the first rotor stage. The vanes oscillate at required frequencies and amplitudes in order to vary the incidence angle of flow over the blade. This causes variation in the load on the blade, resulting in the excitation of the blade at the oscillating frequency. Figure 1.1 shows pictures of the concept as installed on the Darmstadt compressor test bench.

The second concept to be considered was that of a rotating slotted cylinder, positioned in front of the rotor blades. The rotation of the cylinder in the air flow allows air to flow through the slot, alternated by forcing the air to flow around the cylinder. The alternation causes a disturbance in the flow of air around the blade. This causes variation in the load on the blade, resulting in the vibration excitation of the blade at twice the rotating frequency. The slotted cylinder concept is illustrated in Figure 1.2.

Although both the above mentioned concepts were able to demonstrate required excitation levels, they were rejected because they also caused excessive disturbance of the steady flow conditions. The mechanical implementation of both of these concepts would also be too complex and prone to failure.

The concept ultimately selected as the most suitable option was that of excitation by means of gas injection. This system comprises of 15 air injectors, each consisting of a valve mechanism, a compressed air supply and a nozzle piece. The nozzle piece directs air in the desired direction. Two nozzle design

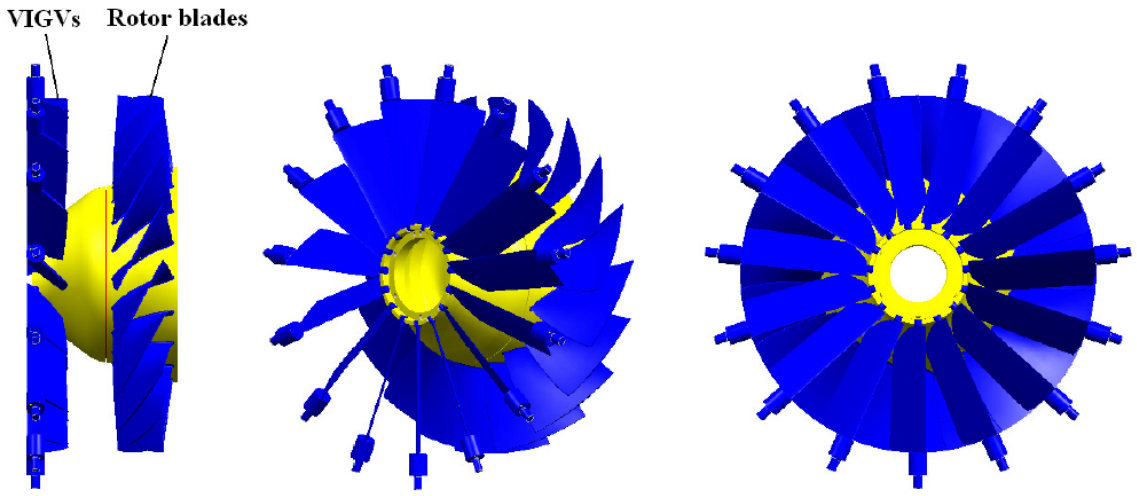

Figure 1.1: Oscillating variable pitch inlet guide vanes (Holzinger *et al.*, 2008)

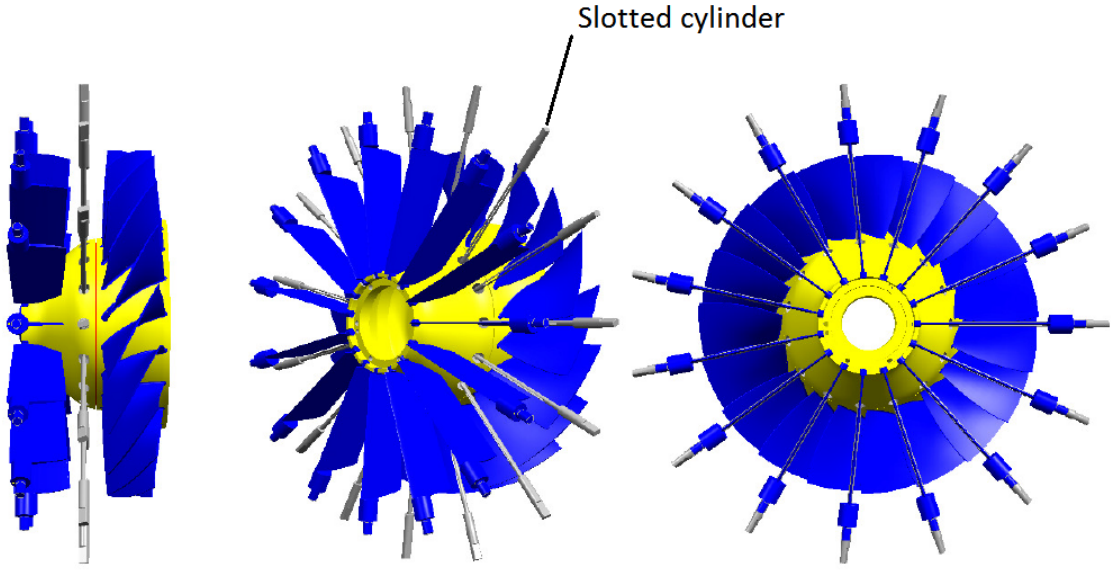

Figure 1.2: Rotating slotted cylinders (Holzinger *et al.*, 2008)

options were considered: the injection air from the casing towards the hub (radial injection), or the injection of air directly onto the rotating blades (axial injection). Figure 1.3 shows the gas injector system installed on the Darmstadt compressor test bench. The axial injection design was refined to a free form axial injector, with no parts protruding into the air flow. This system causes perturbations in the velocity profile of the air flow onto the blade, causing variation in blade force which leads to blade excitation.

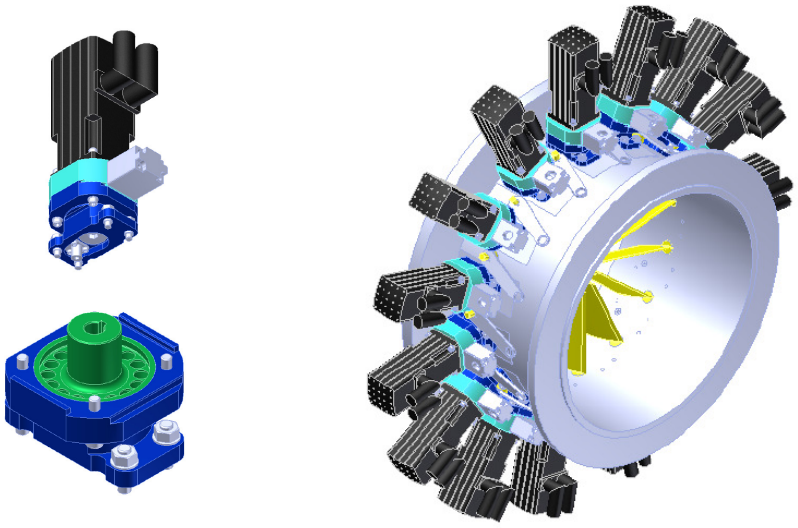

Figure 1.3: Gas injection exciter prototype and 15 exciters installed on the Darmstadt compressor rig

1.2 Project objectives

The objective of this project was to evaluate the effectiveness of the gas injection system as a means of exciting vibrations over a range of frequencies, on the first stage rotor blades of an axial compressor. The project consisted of experimental work and Computational Fluid Dynamics (CFD) simulation. The aim of the experimental work was to characterise the velocity perturbations caused by three different gas injection nozzles under a range of various exciter system operating conditions. At the time of completion of this thesis, the full 15 injector exciter system was not yet available for experimental testing. A single exciter with the various nozzle types were however available for experimental testing. The results from these tests were used to specify and verify boundary conditions for the CFD component of the thesis.

A CFD model of a section of the Stellenbosch University Rofanco compressor test bench was generated to simulate the operation of the three gas injection nozzle types, with the final aim of evaluating their effectiveness as vibration exciters. Unsteady simulations of one full revolution were performed for a number of operating conditions for the various nozzles. The data obtained from the experimental results was utilised as the input for the boundary conditions of the unsteady simulations. For a number of selected cases, the experimentally measured axial velocity perturbations, caused by the injector nozzles, were correlated with the unsteady simulation results of the corresponding test points. The variation in the flow around the blade as a result of the various nozzle types, was analysed and processed to provide the variation in the blade force perpendicular to the blade root. Fast Fourier Transforms (FFTs) were performed on the blade force data in order to evaluate its effectiveness as a source of excitation at desired frequencies.

More specifically and in more detail, the objectives of the project were as follows:

- Modification of the compressor inlet casing to accommodate the installation of the 15 exciters.
- Installation of a half-bridge strain gauge arrangement on two first stage compressor blades, as well as a slip ring assembly to relay current to and from the strain gauges while the compressor is rotating.
- Verification of the effectiveness of the strain gauge arrangements to measure blade deflection, as well as blade vibration. Tests were performed with the compressor stationary as well as operating at 3000 RPM.
- A preliminary evaluation of the effectiveness of the gas injection system was performed by using a single exciter to inject air onto a strain-gauged blade, while keeping the compressor stationary.
- Characterisation of the gas injection exciter nozzle velocity profiles (radial, axial and production axial), with the compressor operating at 3000 RPM. This was achieved by measuring the velocity profile perturbations in front of the first stage rotor blade, which occurred as a result of excitation at various frequencies and injector mass flow supply rates. These measurements were performed with a hot wire anemometer.
- Construction and verification of a single passage CFD model of all 3 stages of the Rofanco compressor.
- Construction of a section of the first rotor stage (based on the single passage CFD model) for unsteady simulation, including inlet boundaries for the various injection nozzles.

- Establish a good correlation between the simulation results and the profile measured during experimental exciter characterisation, by iteratively adjusting the injection nozzle inlet boundary conditions to alter the velocity perturbation profile in front of the blade.
- Performance of unsteady simulations of one revolution to determine the variation in the blade force perpendicular to the blade root as a result of velocity perturbations.
- Evaluation of the frequency response function of the variation in the blade force perpendicular to the blade root, to verify if the intended excitation frequency is sufficiently prominent to excite blade vibration.
- Evaluation of the blade response in the frequency domain, to verify if the intended excitation frequency is sufficiently prominent to excite blade vibration.

Chapter 2

Literature review

A literature review was undertaken to gain a better understanding of the methods employed in the aircraft industry to test for flutter. The literature suggests that vibration excitation is one method of testing for flutter. Further research was therefore done to gain a better understanding of vibration on compressor blades. Finally, a brief study was made of the flow over a compressor blade in order to assess the possibility of exciting vibration in the blade by altering the flow over it.

2.1 Flutter testing on aircraft

As mentioned in chapter 1, flutter is a self excited oscillation or instability at or close to the blade natural frequency which does not require any disturbance. It is the dynamic instability of an elastic body with inertia that is caused by aerodynamic forces (Cumpsty, 1989). It is usually found in structures that are subject to high aerodynamic loading, like wings, aircraft tail structures and control surfaces. Flutter starts at a certain speed V_f , called the flutter speed or critical speed. As the speed increases, the structure becomes unstable. If the speed is not decreased, the structure can fail. Flutter is not a reaction to forced vibration, i.e. it does not occur as a result of being exposed to vibration at its natural frequency, or any other particular frequency. The risk of flutter or the flutter characteristics can however be determined by calculating the damping ratio for specific flow conditions, by exposing the blade to forced vibration.

In the past, flutter testing on aircraft has been performed successfully by using two methods (Scanlan and Rosenbaum, 1951). The first method involves installing a vibration exciter on the wing or empennage, exciting vibration on the structure and then measuring the peak response as a function of airspeed. The response is measured by accelerometers or strain gauges which are installed at critical positions on the airframe structure. The data is then sent to

a ground station, where it is recorded and analysed. At each airspeed setting, the peak response of the resonant frequency is measured. As the speed at which flutter will occur is approached, the resonance frequency peak response increases, so that the flutter speed of the aircraft can be determined by extrapolation.

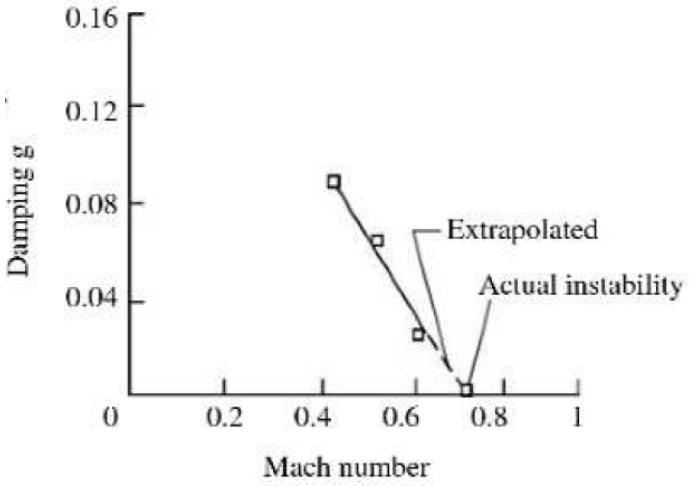

Figure 2.1: Damping trend for limited amplitude instability (Kayran, 2007)

The second method involves determining the rate of decay of the structure after it has been deflected by either a gust, a rapid deflection of the control surfaces, or any other means. Once again the airframe response is measured by accelerometers or strain gauges and the data is sent to a ground station for analysis. The decay rate is then determined as a function of airspeed and as the speed at which flutter will occur is approached, the decay rate approaches zero. Plotting the decay rate as a function of airspeed and then extrapolating to a decay rate of zero, indicates the speed at which flutter will occur. The decay rate is a function of the damping ratio, such that a damping ratio of zero also occurs at the flutter speed. Kayran (2007) explains that the most widely used indicator of stability is the variation of modal damping associated with variation in airspeed. Damping ratios are evaluated for all the significant modes at a number of sub-critical airspeeds. A polynomial curve is fitted to the damping ratio trends and then extrapolated to determine the flutter speed. (See figure 2.1).

The damping ratio can be determined by making use of the peak amplitude method. According to this method, the damping ratio of a structure is determined by plotting the magnitude of the frequency response (modulus) as a result of vibration excitation, for a range of frequencies (White and Walker,

1982). The bandwidth at the maximum amplitude A_{max} (see figure 2.2), divided by $\sqrt{2}$ is used to determine the damping ratio. If there is light damping, the resonance frequency will be the frequency at which the maximum amplitude response will occur. The damping ratio is calculated as follows:

$$\zeta = \Delta\omega/\omega_n \tag{2.1.1}$$

where ζ is the damping ratio, $\Delta\omega$ is the bandwidth at $A_{max}/\sqrt{2}$ and ω_n is the natural frequency. According to Kayran (2007) the airworthiness regulation MIL-A-8870C (1993) requires that the structural and aerodynamic damping ratio for any critical flutter mode, must be at least 0.03. Any critical flutter mode should be within the cruising speed and altitude envelope. (In this instance the article used the term damping coefficient, but it is assumed that the intention was to refer to the damping ratio.) Regulation also requires that the excitation technique used, must be capable of exciting all structural modes that are able to contribute to the various critical flutter conditions. The excitation technique must provide adequate energy to excite selected modes in order to accurately assess the stability from the response data.

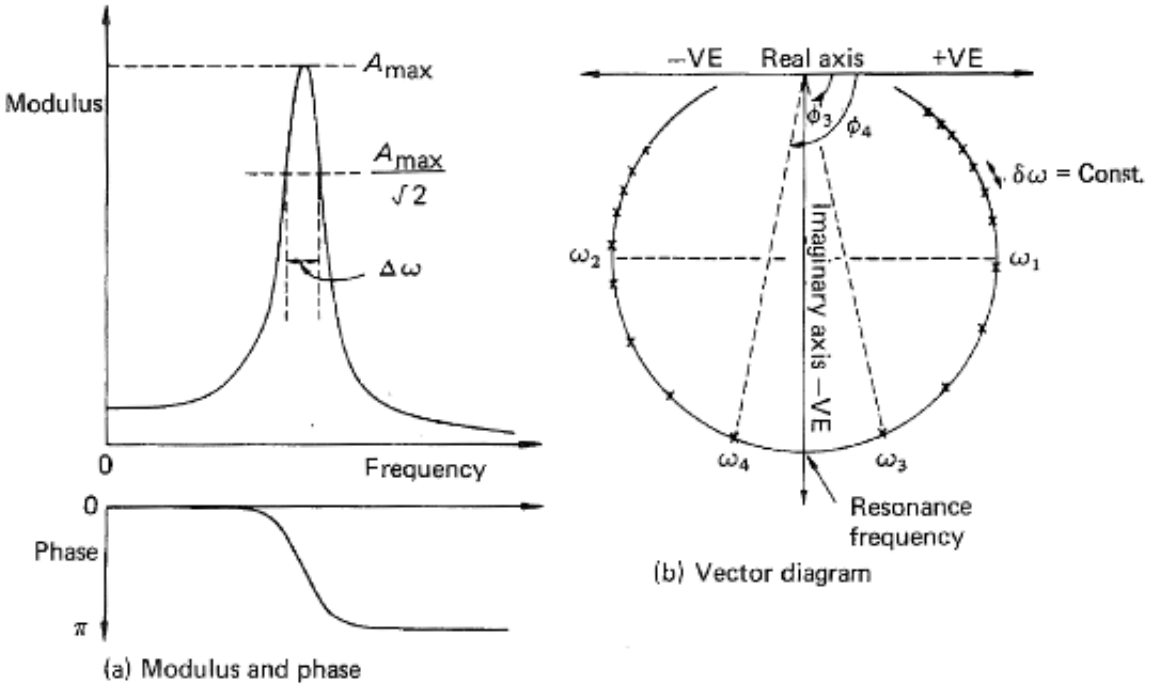

Figure 2.2: Frequency response function of a single degree of freedom system (White and Walker, 1982)

The CSIR and the SAAF use the second method, which involves calculating the damping ratio to determine the flutter speed. For example, new missile, bomb and external fuel tank configurations for fighter aircraft are flutter tested using this method. Vibration is excited by means of rotating mechanical vibration exciters that are fitted to the aircraft. On the Cheetah aircraft for example, the exciters are fitted under the wing tip. The exciter induces vibration at a fixed frequency or in the form of a frequency sweep at various airspeed settings. Data is processed in almost real time in a ground telemetry station, to produce flutter test results.

2.2 Vibration and forced vibration in compressor blades

When comparing compressor stator and rotor blades, problems with vibration are mostly found in rotor blades (Cumpsty, 1989). Rotor blades are more susceptible to vibration because damping occurs less frequently than on stator blades. The reason for this is that the high centrifugal load results in a very tight fit at the blade root-disk interface. The tight fit leaves very little freedom for rubbing and therefore very light damping. A stator blade on the other hand does not tighten up and the small amount of movement available at the root is therefore enough to provide damping against vibration.

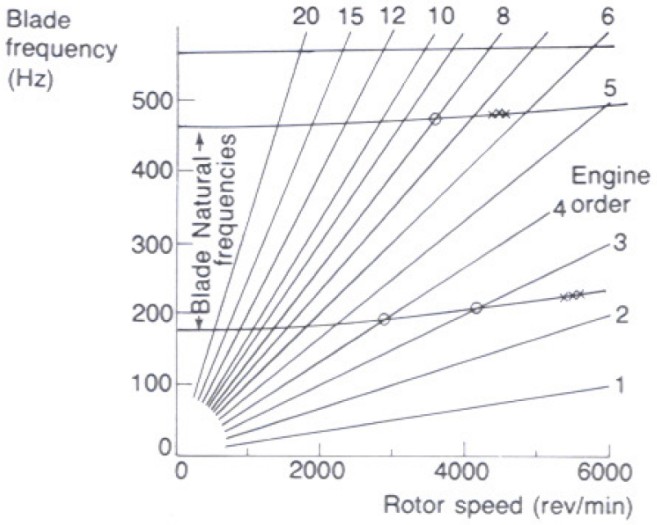

Figure 2.3: Blade natural frequency plotted with engine orders (Cumpsty, 1989)

Forced vibration is found when the rotor passes through disturbances in the air flow which are usually stationary, like the wake of an upstream stator. Forced vibration becomes a problem when excitation coincides with the natural frequency of the blade. To induce forced vibration, all sources (with the exception of stall cells) must be at the harmonics of the rotational frequency of the rotor itself. The rotational frequency of the rotor shaft and its harmonics are often referred to as engine orders. Figure 2.3 shows engine orders as lines from the origin as the engine speed increases, plotted against frequency on the vertical axis. The blade natural frequency range is also indicated on the vertical axis. Where a blade frequency coincides with an engine order, a potential problem exists.

2.3 Blade vibration modes and natural frequency

Three types of blade vibration modes exist; namely bending, torsion, and edge vibration. The bending mode is also referred to as the flapping mode. The respective mode frequencies are not related; for example the torsion mode frequency can be higher than both the first and the second bending modes. Figure 2.4 from Armstrong and Stevenson (1960) shows a typical example of the four lowest blade vibration modes with their respective frequencies.

The blade natural frequency is influenced by a number of factors. The first factor is the type of material. The ratio of the Youngs modulus or the shear modulus to the density of the blade material determines the natural frequency, but because it is very similar for most materials that are used for blades, it has a negligible effect. In other words, the effect of changing the material type on the natural frequency is small.

Another factor is the blade rotational speed. The centrifugal force has the effect of stiffening the blade and so increases the blade bending mode frequencies. Rotational speed has virtually no effect on the torsional mode. According to Cumpsty (1989), the effect of the rotation speed on the natural frequency can be expressed as:

$$\omega_n^2 = \omega_0^2 + k\Omega^2 \tag{2.3.1}$$

where ω_n is the natural frequency, ω_0 is the natural frequency with the blade stationary, Ω is the angular velocity of the shaft and k is the factor by which Ω influences ω. Therefore the higher the rotation speed, the higher the blade

natural frequency will be.

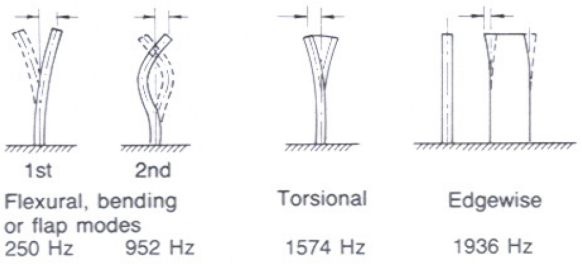

Figure 2.4: Blade vibration modes (Armstrong and Stevenson, 1960)

Finally, the last factor to influence the natural frequency is temperature. Compressor blades can operate at temperatures of up to 300°C or higher. The blade operating temperature can therefore differ significantly from the normal outside temperature, which might have an influence on the blade natural frequency. The higher the temperature, the lower the natural frequency will be. Temperature has an effect on all modes of vibration.

2.4 Blade vibration measurement

The most common method of measuring blade vibration involves the installation of strain gauges on the blade and measuring its deflection. Several studies have employed this method to verify the performance of more advanced technologies. For example, Lawson and Ivey (2005), as well as Knappet and Garcia (2008), verified the performance of blade tip timing by comparing it with the results from a strain gauged blade. These studies were done on rotating blades. Figure 2.5 shows the schematic lay-out of a typical blade tip-timing system.

Ghouti *et al.* (2003) used this method to verify the results of a test performed to relate blade deformation to the deformation measured on the torsion shaft itself. In this experiment, a stationary blade on a torsion shaft was used. The blade was subjected to forced vibration and the response on both the blade and the torsion shaft were analysed and compared.

Several other non-interference methods for measuring blade vibration have been tested. While the non-interfering nature of these methods make them more appealing, they are also more costly and complicated. Furthermore, in the referenced studies, it is frequently mentioned that using strain gauges and a slip ring is a good and trusted method of measuring and analysing blade

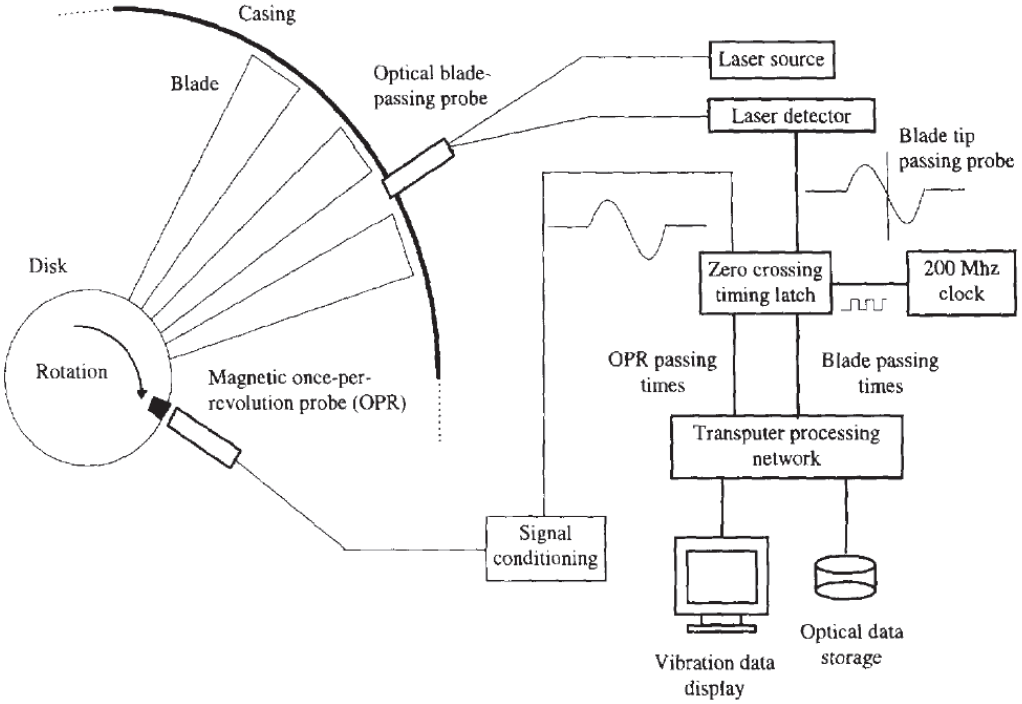

Figure 2.5: A typical blade tip-timing system (Heath and Imregun, 1996)

deformation and vibration on compressors.

2.5 Variation in blade flow velocity as a means of inducing vibration

In chapter 1, it was explained that gas injection was the selected concept of blade vibration excitation for this project. The design intention of this concept was to periodically change the flow over the blade to excite vibration at a desired frequency. An axial excitation nozzle would periodically increase the axial velocity, C_a, whereas radial excitation would periodically decrease C_a. The possible effect of a variation in C_a will now be discussed.

Figure 2.6 from Sayers (1990) shows a diagram of the lift and drag force directions and the velocity triangle of flow over a compressor blade.

Sayers gives the lift coefficient C_L as a function of the mean velocity vector, W_∞ and the lift force, L (perpendicular to the mean velocity vector). Rearranging the equation in Sayers (1990) shows that L is given by the following equation:

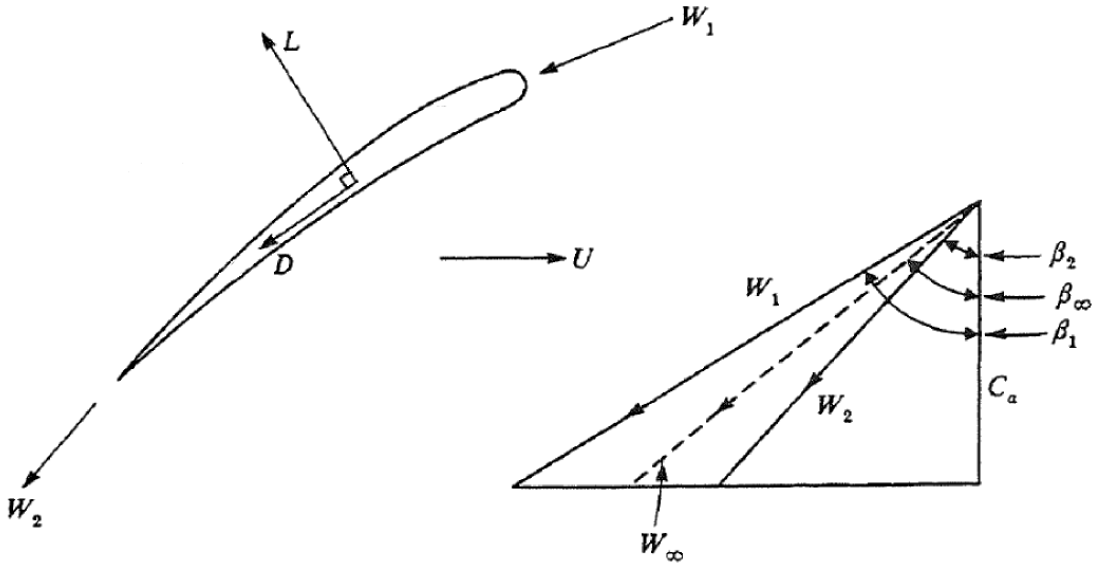

Figure 2.6: Lift and drag forces on a compressor rotor blade (Sayers, 1990)

$$L = C_L 0.5 \rho W_\infty^2 A \tag{2.5.1}$$

where ρ is the density and A is the area of the blade given by the product of the chord c and the blade length l. It is known that an increase in the angle of attack of an airfoil results in an increase in C_L until the point of stall. The angle of attack, α, is given by:

$$\alpha = \gamma - (90 - \beta_\infty) = \gamma - \beta_\infty - 90 \tag{2.5.2}$$

where γ is the blade stagger angle. An increase in β_∞ will therefore lead to an increase in C_L, which will increase L. From the velocity triangle in figure 2.6 it can be seen that a decrease in C_a, the axial velocity, will result in an increase in β_∞. An increase in the angle of attack will also cause an increase in the drag force D, which means that the resultant force on the blade caused by the increase in L and D will also increase. It is therefore possible for the resultant blade force perpendicular to the blade root to increase as a result of a decrease in C_a.

On the other hand, it is also clear from equation 2.5.1, that a decrease in W_∞ will cause a quadratic decrease in the blade lift force L. From the velocity triangle in figure 2.6 it can be seen that a decrease in C_a will result in a decrease in W_∞. A decrease in W_∞ will also cause a decrease in the drag force D, which means that the resultant force on the blade caused by L and D will also decrease. In this case it is clear that a decrease in C_a may cause a

decrease in the blade force perpendicular to the blade root.

The discussion above suggests that the effect of a variation in C_a will depend on which component of the blade lift force is more dominant. If the effect of C_L is more dominant, axial excitation will cause periodic decreases in the blade force perpendicular to the blade root and radial excitation will cause periodic increases in the blade force perpendicular to the blade root. If the effect of W_∞ is more dominant, axial excitation will cause periodic increases in the blade force perpendicular to the blade root and radial excitation will cause periodic decreases in the blade force perpendicular to the blade root.

Chapter 3

Methodology

3.1 Experimental testing

3.1.1 Exciter characterisation

Three exciter nozzle types were characterised by conducting experimental testing on the Rofanco compressor test bench. The effect of the pulsating air injection was assessed by measuring the perturbations of the axial velocity at a position 10 mm in front of the first stage rotor blades (approximately 80 mm downstream of the nozzle). Measurements were done with a hot film anemometer. The results were processed to assess whether the excitation frequency could be detected and to determine the velocity perturbation profile.

The performance of the respective excitation nozzles were assessed at low, medium and high frequency settings (60 Hz, 650 Hz and 1200 Hz). Each frequency was assessed at a low, medium and high exciter air supply setting.

During the exciter characterisation, the compressor was operating at 3000 RPM and at a relatively high mass flow rate setting to ensure a high inlet velocity. The requirement for a high inlet velocity is to create conditions that resemble, as closely as possible, the high velocity operating conditions of the Darmstadt transonic compressor rig for which the system is designed.

3.1.2 Strain gauge blade vibration measurement system verification

As mentioned in chapter 1, this thesis project did not entail the experimental testing of the full 15 exciter system. It did however include the installation and verification of a strain gauge blade vibration measuring system in preparation for the 15 exciter system testing.

A half-bridge strain gauge arrangement was installed on two opposing first stage rotor blades with approximately the same first mode flapping frequency. The strain gauges were orientated to measure the strain induced by deflection of the blade in the direction of the first flapping mode. The strain gauge wires were routed through the inside of the hub towards a slip ring that connected the strain gauges with the bridge amplifier and the data acquisition station.

The functionality of the strain gauges was verified as follows. Firstly, by doing a simple impact test with the compressor hub in a stationary position, to establish whether it accurately measures the first flapping mode natural frequency. The strain gauge output was then calibrated in terms of blade force loading and blade tip deflection. The mean blade deflection was measured at 3000RPM for various mass flow rate settings and this result was compared to the output from the equivalent simulations (see section 3.2 that follows). Finally, the blade vibration amplitudes at the first flapping mode were measured for various mass flow rate settings at 3000RPM, to establish a baseline for the vibration characteristics.

3.2 Simulation

The first step in the simulation process was to generate a basic CFD model of the full Rofanco compressor. The model was generated as a single passage in Numeca AutoGrid, the solving was performed in Numeca FINE™/Turbo and the post processing in Numeca CFView. A number of solver variables were simulated close to the design point at 3000RPM. The results were compared to the results from experimental work previously performed. Based on these simulations an optimal CFD model of the Rofanco could be established.

This model was then used to perform further simulations at 3000RPM and at various mass flow rate settings. The output of these simulations was a simulated characteristic pressure ratio vs mass flow rate curve of the Rofanco compressor. The model was verified by comparing the characteristic curve of the simulation results with the measured experimental results. The refined baseline model formed the basis of the unsteady simulation model.

The ideal unsteady model would have consisted of a grid with all three stages and all the blades from each stage. However, because of limitations in computational power and also the time cost of a large model, the grid was reduced to a size that could be managed with the available computational capabilities. This was done by making use of periodic boundaries. Periodic boundaries can be applied when periodicity is present in the flow domain. Periodicity is defined as the quality of recurring variation at regular intervals.

Applied to this CFD model, periodicity refers to the regular occurrence of, for example, the rotor blade as a variation in the grid. With a total number of 43 identical rotor blades in the first stage, the blades represented a periodicity of 43. In the case of the exciter nozzles, the 15 identical exciter nozzles around the circumference of the compressor represented a periodicity of 15. To accommodate a grid that was large enough to contain at least one exciter and a number of blades, but small enough to allow usage of existing computational power, the number of blades was approximated to 42 and the number of exciters to 14. The unsteady grid was therefore modelled as 3 blades and one exciter, resulting in a periodicity of 14 (42/3 and 14/1). The grid generation approach is explained in detail in section 5.3.

The compressor inlet was extended upstream of the first rotor blade to accommodate the injector inlet patches. A number of wall cells on the inlet boundary face were re-identified to form the inlet faces (or patches) for the axial and production axial nozzles. Cells on the shroud wall were re-identified to form the inlet patches for the radial nozzle. This approach approximated the circular nozzles as square nozzles. Due to the multi grid solver approach used in the Numeca FINE™/Turbo, modifying the grid to represent the true circular shape of the nozzles would have added a significant time cost to the processing time.

Boundary conditions were then based on measured experimental data for the steady inlet velocity profile, the varying nozzle velocity profiles and the outlet pressure. Unsteady simulations were then performed to correlate the axial velocity profiles 10 mm in front of the rotor blades, with profiles measured during the experimental characterisation of the exciters. The nozzle velocity profiles were then iteratively altered until satisfactory velocity profiles were achieved.

The final step was to perform unsteady simulations for one full compressor revolution. From the solution output, the variation in the resultant force on the blade perpendicular to the blade root was then calculated and plotted for each time step. A FFT was then performed on the force time series to establish to what extent the excitation frequency was present in the variation in the blade force. In reality, the variation in blade force perpendicular to the blade root would be the input that would excite vibration at the first flapping mode of the blade.

Chapter 4

Experimental Testing

4.1 Rofanco Compressor description and lay-out

4.1.1 Components and schematic lay-out

The Rofanco Compressor is a three stage axial compressor with all the rotor blade rows mounted on a single hub and all the stator blades mounted to the outer casing. Each rotor stage has 43 blades, while each stator stage has 41 blades. In front of the first rotor stage is a set of 36 inlet guide vanes (IGVs). The IGVs were however removed from the actual compressor to accommodate the exciter injectors. The hub has a diameter of 300 mm and the casing inner surface has a diameter of 420 mm.

A bell-mouth inlet casing is located in front of the IGVs. The outlet of the compressor forms a venturi, where an anemometer is located. A throttling valve that is used to adjust the mass flow rate of the compressor, is located downstream of the venturi. The hub is connected directly to a 15 kW three phase direct current (DC) electrical motor. The electrical motor speed and direction of rotation is controlled by the control unit. Figure 4.1 gives a schematic lay-out of the various components of the compressor.

On the Rofanco Compressor, three parameters are monitored for basic performance measurement of the compressor. A hand-held taco meter is used to measure the compressor speed. The pressure ratio is determined by calculating the difference between the output from pressure taps on the casing, located in front of the first rotor stage and downstream of the last stator stage. The volume flow rate is measured by the anemometer in the venturi downstream of the compressor. By assuming that the air density is approximately equal to atmospheric pressure, the mass flow rate can be calculated. At a certain rotation speed, the compressor will produce a specific pressure ratio for a given

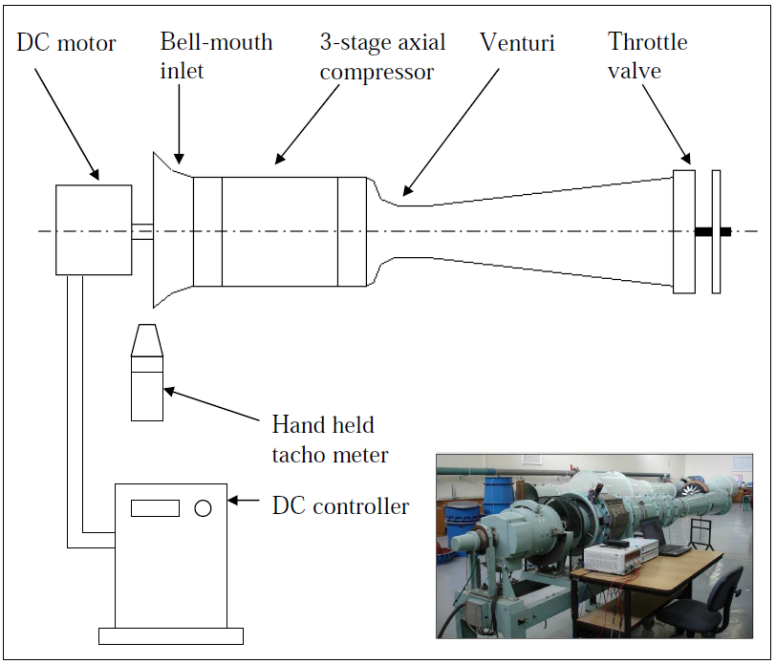

Figure 4.1: Schematic lay-out of the Rofanco compressor test bench

mass flow rate. A performance graph illustrates the relationship between the pressure ratio and the mass flow rate for various speed settings. All test points described in this report were specified as a function of a specific mass flow rate setting.

Two attachment channels are located on the compressor casing, which can be used to attach various measuring equipment, such as pressure probes and hot wire anemometer traverse brackets. The holes in these two channels are positioned in such a way as to provide access to the compressor flow path. Through these holes a measurement probe can be traversed through various radial positions at any of the stages.

4.1.2 Blade geometry

All blades, both rotor and stator, have NACA65 profiles with a chord length of 30 mm and a maximum thickness of 3 mm. The blade stagger and camber angles are provided in table 4.1.

4.1.3 Design point performance specifications

At 101.3 kPa atmospheric pressure and 20 °C, the Rofanco design point produces a pressure ratio of 1.026 at a mass flow rate of 2.66 kg/sec.

Table 4.1: First stage rotor blade profile

Blade section radial position (mm)	Blade profile stagger angle (degrees)	Blade profile camber angle (degrees)
150.0	38.00	31.04
165.0	45.00	23.48
180.0	49.40	17.93
195.0	53.00	13.85
210.0	56.10	10.90

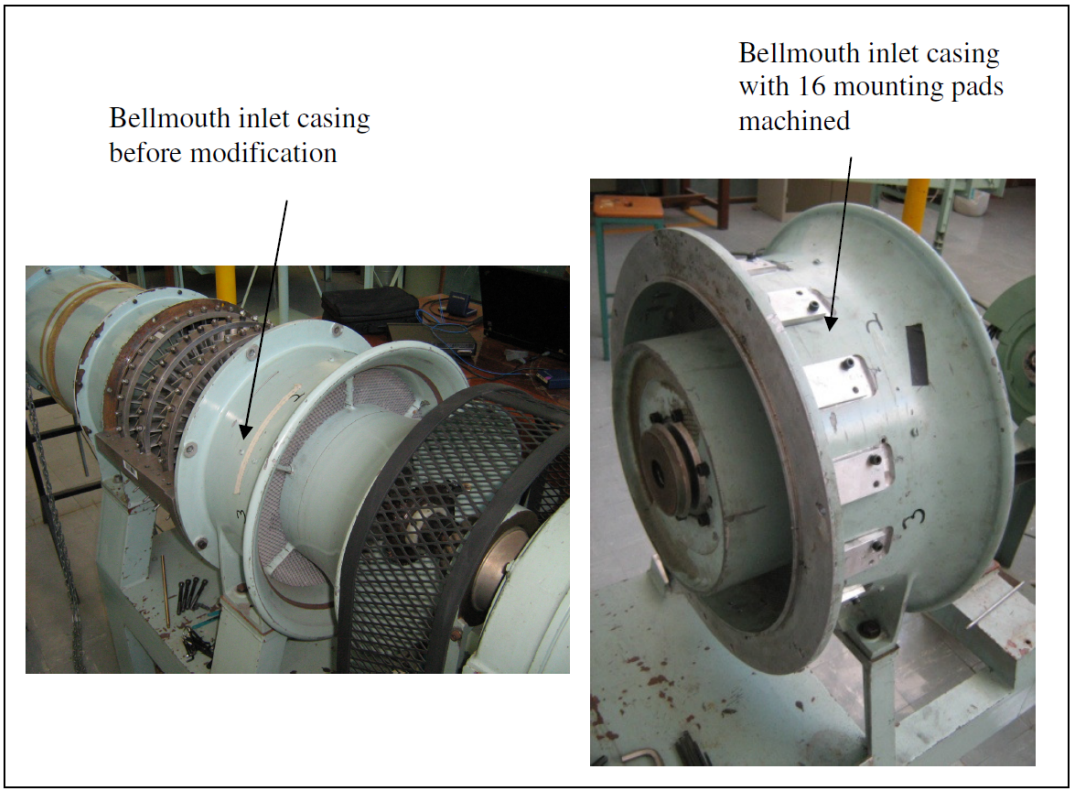

Figure 4.2: Two pictures showing the bell-mouth before and after modification

4.1.4 Modifications to Rofanco Compressor required by this project

In order to prepare the test bench for the requirements of Project Future, a number of alterations and design modifications had to be made. To make provision for the 15 exciters, the bell-mouth was removed and 15 equispaced exciter attachment points were machined into it. A 16^{th} point was machined

to line up perfectly with one of the measurement equipment attachment channels. Sixteen blank-off pads were manufactured to fill the exciter nozzle access holes when the compressor was operating without the exciters. A single exciter was fitted to this point to allow for exciter characterisation to be performed as described in section 4.4. Figure 4.2 depicts the bell-mouth before and after the modification.

Two blades were each fitted with a half-bridge strain gauge arrangement to measure blade vibration. A slip ring was installed as an interface between the strain gauges on the rotating hub and the stationary bridge amplifier. Wires from the strain gauges were routed inside the hub, through the compressor shaft and then via the slip ring to the strain gauge amplifier.

4.2 Excitation equipment

The first prototype exciter, developed and manufactured by the CSIR, was tested as a single exciter used for exciter characterization. This prototype could be fitted with either a radial or an axial exciter nozzle. A single production exciter model, fitted with a more advanced axial nozzle (the production axial nozzle), was subsequently made available for testing at Stellenbosch. This model was also used for exciter characterization. The production axial nozzle was an improvement on the first axial nozzle, because it provided axial excitation focussed on the blade tip, without the disadvantage of a probe that is inserted into the airflow. A description of the various nozzles is provided in section 4.2.1.

4.2.1 Single Exciter System

The single exciter system consists of a speed controller, an electric motor, a valve mechanism, three types of injector nozzles, a volume flow rate meter and a differential pressure gauge. Figure 4.3 shows a schematic lay-out of the single exciter experimental set-up. Compressed air is supplied to a valve mechanism which is able to open and close at a desired frequency. The pulsating air is then injected through the nozzle into the compressor inlet air flow. The pulsating injection causes velocity perturbations that excite vibration in the downstream blades.

The valve mechanism consists of a rotating disc with 16 equispaced holes. The disc is located inside the valve housing and is held in position by two bearing assemblies. The housing has an air inlet at the top and an air outlet opening at the bottom. The outlet is positioned on the pitch circle diameter

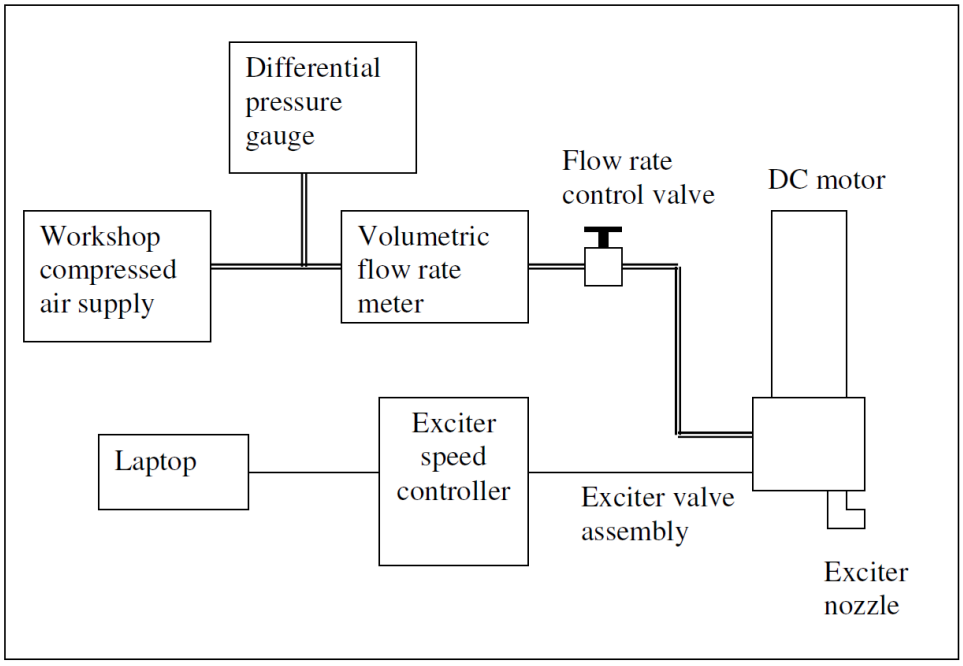

Figure 4.3: Schematic lay-out of the single exciter set-up

of the holes in the rotating disc.

The valve housing cavity is constantly filled with compressed air. When a hole in the rotating disc slides over the outlet, air flows out of the housing at a rate determined by the pressure of the air supply to the housing. The continuous sliding of rotating holes past the outlet opening produces a pulsation of air at a frequency of 16 times the rotational speed of the disc. The rotating disc is connected to a variable speed DC motor. Figure 4.4 illustrates the exciter assembly and clearly shows the rotating disc. The motor produces 1.15 Kw and for this project was operated at a maximum speed of 4500 RPM. The exciter was therefore able to produce a maximum frequency of 1200 Hz.

The speed controller is connected to a laptop, from which the user interface allows the operator to control the valve speed and acceleration. The mass flow rate of the excitation is monitored by means of the volume flow rate meter that is connected upstream of the flow rate control valve. A pressure gauge is also connected near the volume flow rate meter upstream from the flow rate control valve. The gauge indicates the pressure difference between the static pressure of air that flows through the volume flow rate meter and atmospheric pressure. The pressure difference is used to calculate the density of air that flows through the volume flow rate meter, which can then be used to determine the mass flow rate of the exciter.

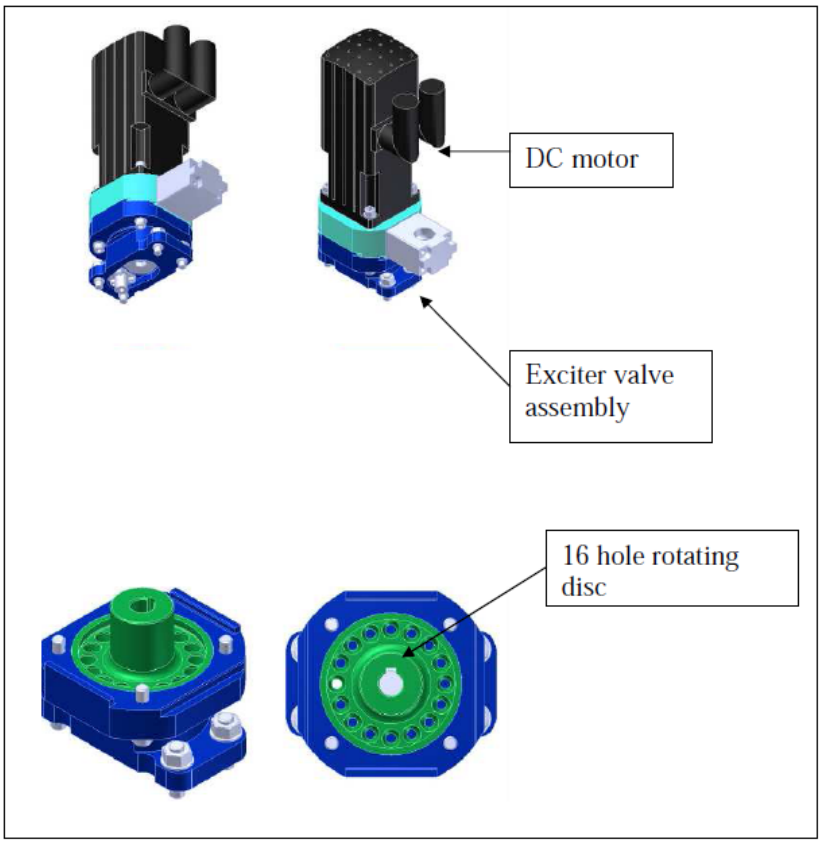

Figure 4.4: Exciter

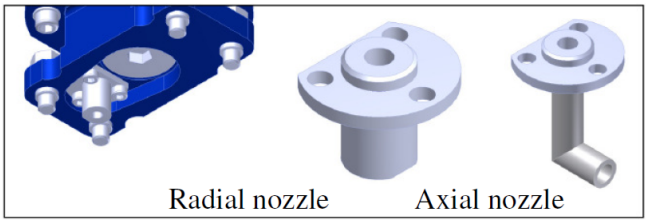

Figure 4.5: Radial and axial nozzles

Three types of injector nozzles were tested. The first radial and axial nozzles are shown in figure 4.5. The radial valve injects air at 90° to the air flow, from the casing towards the hub. The axial injector is inserted into the air flow and redirects the air from the valve housing through 90° to provide a focussed excitation in the region of the blade tip.

The third nozzle, the production axial nozzle (figure 4.6) has a curved flow path that guides the air flow from the nozzle through approximately 90°, but the nozzle exit is machined so that it is located flush with the casing. In other words, this nozzle provides a focussed excitation in the region of the blade

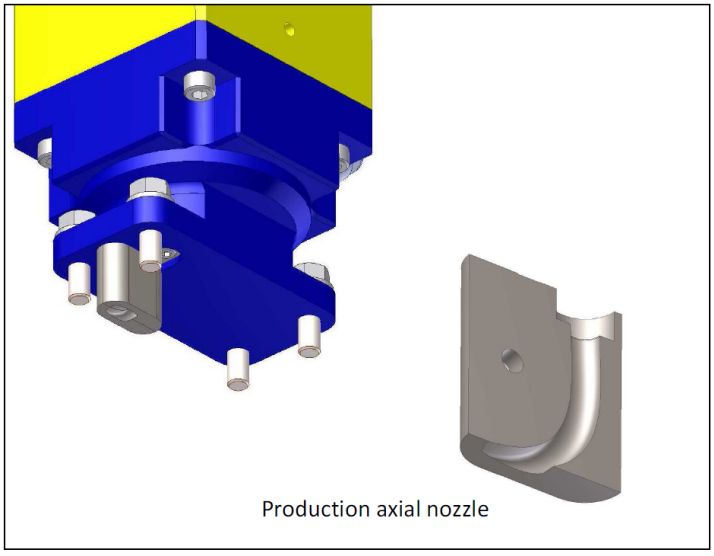

Figure 4.6: Production axial nozzle

tip, without the disturbance caused by a probe that is inserted into the air flow. Figures A.3, A.4 and A.5 in Appendix A show schematic drawings of the position of the first stage rotor blades relative to the exciter nozzles and the hot wire anemometer sensor. The position of the exciter nozzles relative to the rotor blades was determined by physical properties of the compressor bell-mouth and outer casing. Ideally the nozzles should have been positioned as close as possible to the blades. However, due to the interface characteristics of the bell-mouth and outer casing, it could only be positioned as shown in Appendix A. The hot wire anemometer will be discussed in the next section.

4.3 Excitation measuring systems

4.3.1 Hot wire anemometer

A hot wire anemometer was used to characterise the velocity perturbation profiles, both in front of the first stage rotor blades and at the nozzle exit. This sensor was chosen for its ability to measure very small fluctuations in velocity in real time. The hot wire anemometer measures the small changes in voltage caused by the changes in temperature associated with the variation in air velocity. It is a known fact that the variation in static temperature drop, associated with increased airspeed, must be taken into account when calibrating the hot wire anemometer (Ball *et al.*, 1999). For the purpose of the characterisation of the exciter velocity profile, the temperature variation associated with the relatively low axial velocity (40 m/sec) was, however, considered as negligible. It was therefore not taken into account when the hot wire

was calibrated. At the exciter nozzle exit, where the velocity is expected to be around 300 m/sec, the effect of the variation in temperature was significant and was therefore taken into account for the correction of the hot wire voltage output. The following equation from Ball *et al.* (1999) was used:

$$E^2 = E_m^2 \frac{(T_w - T_r)}{(T_w - T_f)} \tag{4.3.1}$$

where E is the corrected voltage, E_m is the measured hot-wire voltage, T_w is the wire temperature, T_r is the reference temperature at which the hot wire was calibrated and T_f is the air temperature.

A single direction hot wire anemometer with a resistance of 8.895 Ω was used. The probe was mounted on a traverse in such a way that it would record the axial velocity Vz. The traverse made it possible to measure various radial positions on one tangential position.

The hot wire sensor was used with the TSI IFA-100 hot wire amplifier. The 0 to 5V output signal was connected to a National Instruments NI USB 6218 multifunction signal hub and recorded via the Data Logger software. All hot wire measurements were taken at a sampling rate of 25 kHz. Figure 4.7 gives a schematic layout of the hot wire anemometer set-up.

4.3.2 Half-bridge strain gauges

Two of the first stage rotor blades were each fitted with a half bridge strain gauge arrangement. On each blade, two strain gauges were attached - one on each side of the blade root. The strain gauges were positioned such that they could be configured as a half bridge that measured the first flapping (bending) mode. Figures A.1 and A.2 in Appendix A show the positions of the strain gauges on the two blades in detail. The two modified blades, blade 3 and blade 25, were positioned opposite each other to measure nodal diameter excitation, as required by Project Future. The two blades were chosen to have approximately the same first mode flapping natural frequency. For both blades, the frequency was measured as 642 Hz by Duvenhage (2009). Figure 4.8 shows the position of a strain gauged blade on the hub, as well as a picture of a strain gauge attached to the suction side of a blade. The technical specifications of the strain gauges are found in Appendix A

The strain gauge arrangements were connected to a bridge amplifier via a slip ring system. The slip ring was manufactured by M-Tek and is described as an 8 Circuit Slip Ring Interface, with part number SC049-000000-04. The slip ring was mounted on an attachment bracket to ensure concentricity between

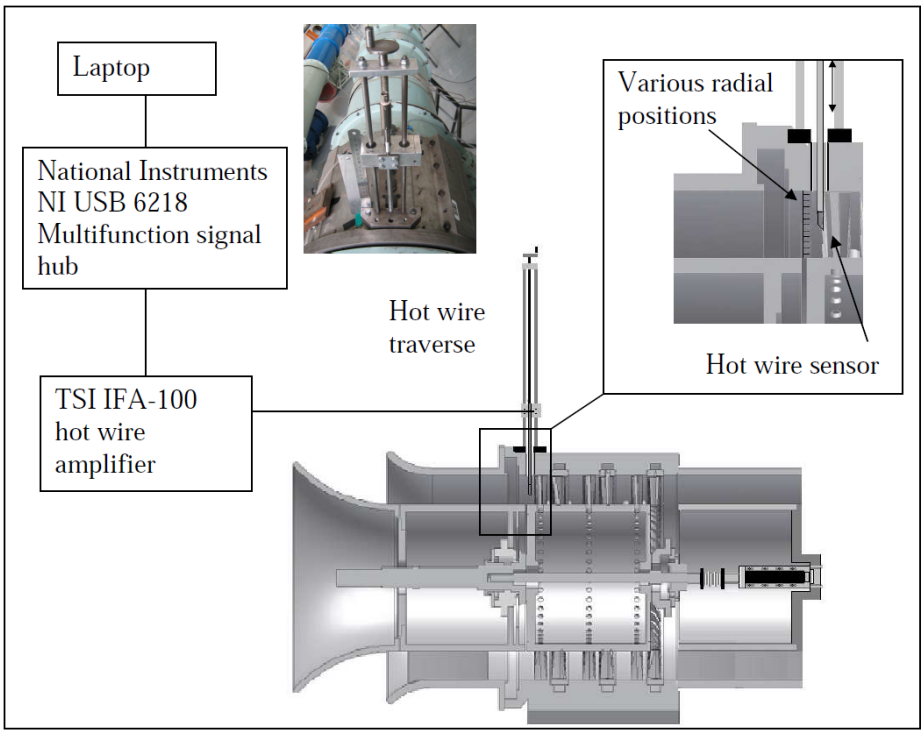

Figure 4.7: Schematic lay-out of the hot wire anemometer set-up

the compressor shaft and the slip ring. A flexible coupling connected the slip ring to the compressor shaft. Thin copper wires were routed from the strain gauges into the hub through small holes, along the inside of the hub to the rear of the compressor, down the outer rear face of the hub and then along the inside of the shaft through the flexible coupling into the slip ring. From the slip ring, the cables were routed through the rear outer casing towards the amplifier. Figure 4.9 illustrates the layout of the slip ring system.

The strain gauges were connected to a HBM KWS-3020 B bridge amplifier. The 0 to 5V output signal was connected to a National Instruments NI USB 6218 multifunction signal hub and recorded on a PC with the Data Logger software. During all measurements, the settings on the HBM were as follows:

- Excitation voltage: $5V$
- Range: 1 mV/V at 10 V

All strain gauge measurements were taken at a sampling rate of 25 kHz. Figure 4.10 gives a schematic layout of the strain gauge blade vibration recording set-up.

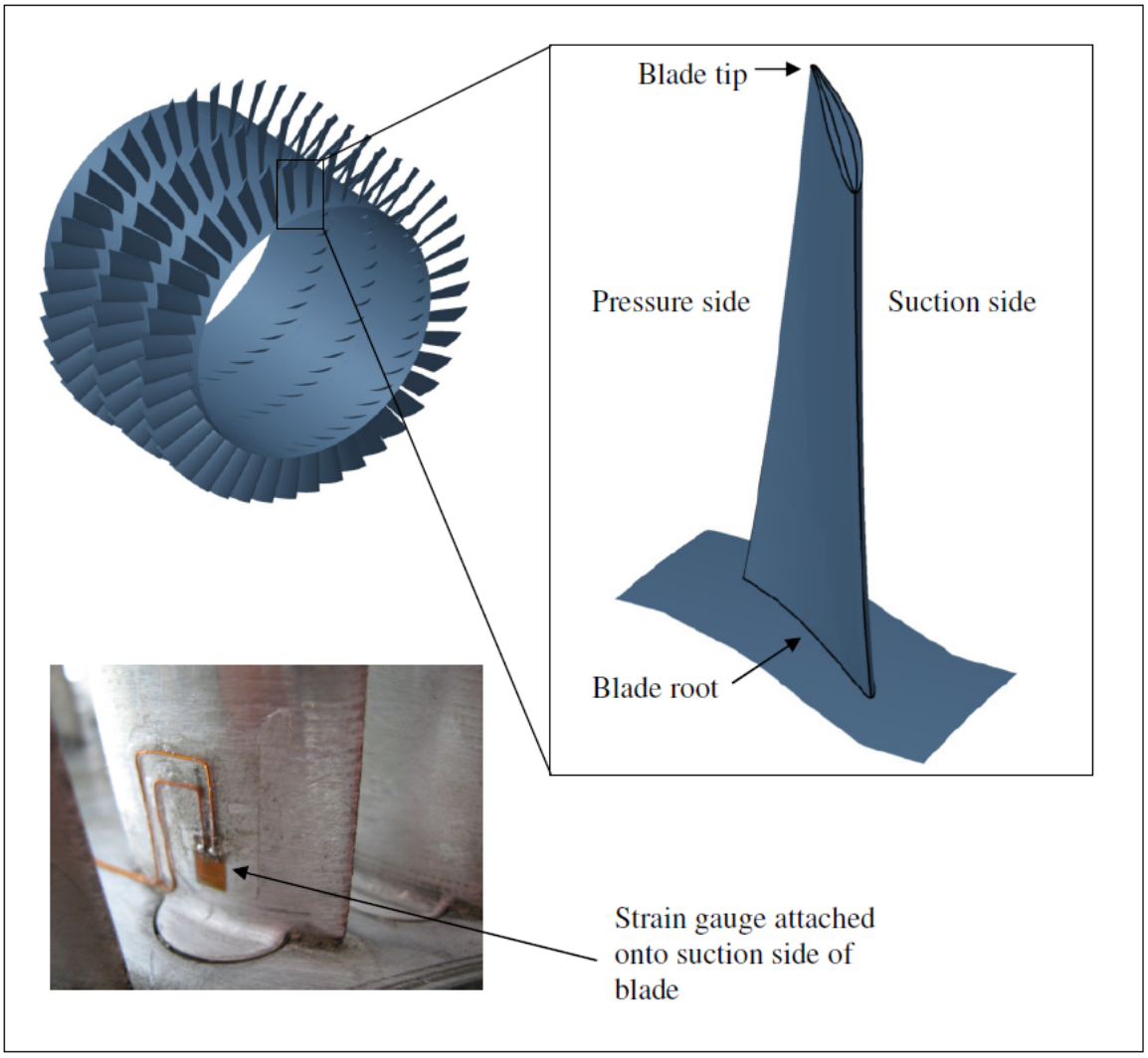

Figure 4.8: Schematic lay-out of the position of a strain gauged blade on the hub

4.4 Exciter downstream velocity profile characterisation

4.4.1 Description

For the exciter characterisation, the required injection nozzle was fitted to the exciter, which in turn was fitted to attachment point no 16. This ensured that the nozzle was positioned directly upstream of the hot wire anemometer. The axial positions of the various nozzle types relative to the hot wire and the first stage rotor blades are shown in section A.3. Preliminary testing showed that the velocity perturbation caused by axial injection was focussed on the first 20 mm from the casing inwards (towards the hub). For this reason, measurements with the hot wire were taken from a radial position of 0.208 m (2 mm

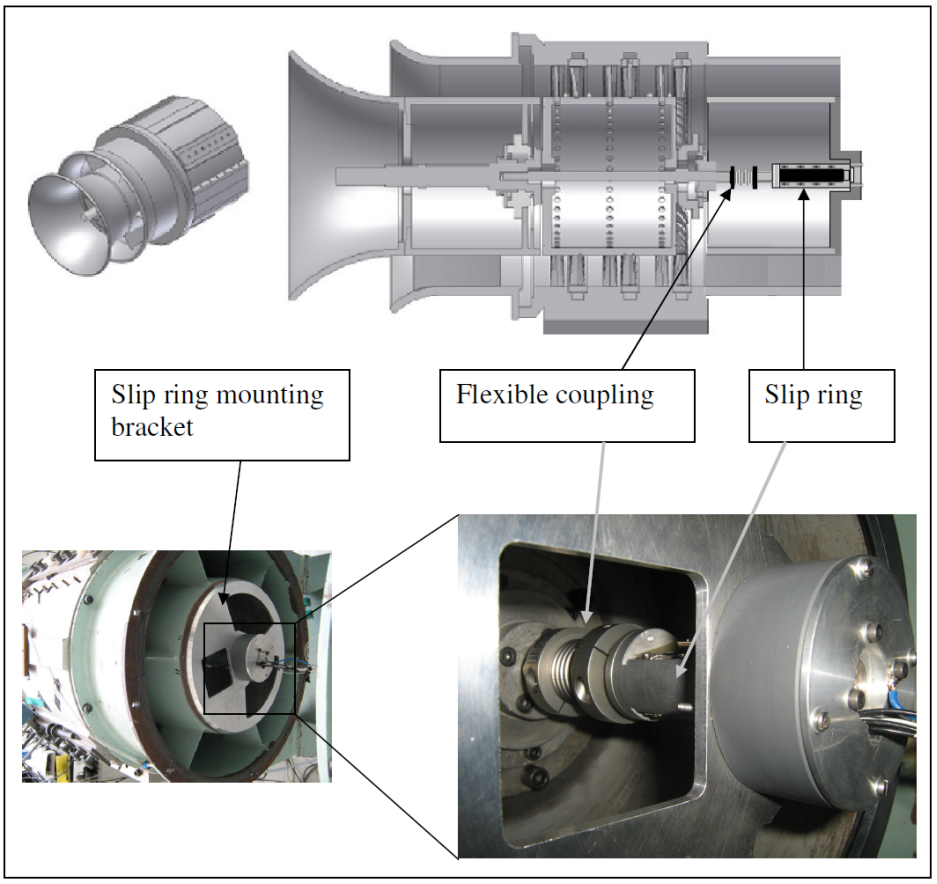

Figure 4.9: Schematic lay-out of the slip ring installation

from the inside of the casing), to 0.19 m in increments of 2 mm. Preliminary testing further showed that velocity perturbations caused by radial injection were distributed all the way between the hub and the casing. Measurements with the hot wire were taken from a radial position of 0.205 m (5 mm from the casing), to a position of 0.155 m (5 mm from the hub). In the case of the production axial nozzle, the perturbations were focussed on the outer third part of the rotor blade and to a lesser extent, on the remaining two thirds of the blade. For this reason, measurements of the perturbations caused by the production axial nozzle were taken from a radial position of 0.155 m (5 mm from the hub), to a position of 0.185 m, in increments of 5 mm. From the radial position of 0.19 m to a position of 0.208 m (2 mm from the casing), measurements were taken in increments of 4 mm.

4.4.2 Test points

Exciter characterisation was done for all three nozzle types. The objective was not only to acquire data that could be used to verify the simulation work

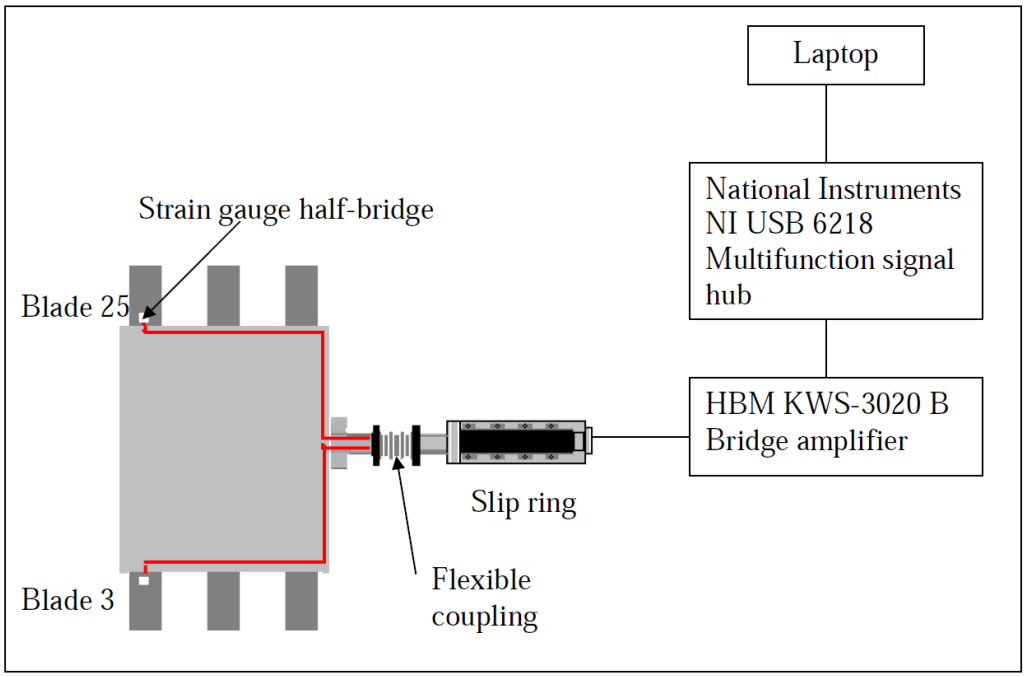

Figure 4.10: Schematic lay-out of the strain gauge blade vibration recording set-up

described in chapter 5, but also to assess the behaviour of the exciter at various settings. The approach was to test each nozzle at a low, medium and high frequency to evaluate the effect of varying the frequency. At the medium frequency setting, the nozzle was tested at a low, medium and high exciter mass flow rate, in order to evaluate the effect of varying the mass flow rate. Each nozzle was tested at 60 Hz, 650 Hz and 1200 Hz with the exciter supply rate set to 23.8 x 10^{-3} kg/sec. In addition, at 650 Hz, each nozzle was tested at an exciter air supply rate of 13.8 and 19.9 10^{-3} kg/sec. It must be noted at this stage that, due to leakages in the injector valve mechanism, the mentioned mass flow rate figures were not the mass flow rates of the air injected into the compressor.

4.4.3 Results: FFT of velocity perturbation

As an initial investigation, the ability of the nozzles to excite the desired frequency was assessed. The radial position of the highest velocity perturbation was determined by inspection and for that point an FFT was performed on the time dependent velocity data. Appendices K and L, show that without exception, for all frequencies and injector mass flow rate settings, the excitation frequency was clearly the most dominant frequency present. Furthermore, the first and second harmonic of the excitation frequency was distinguishable. This suggests that the wave form produced by the injector mechanism was not

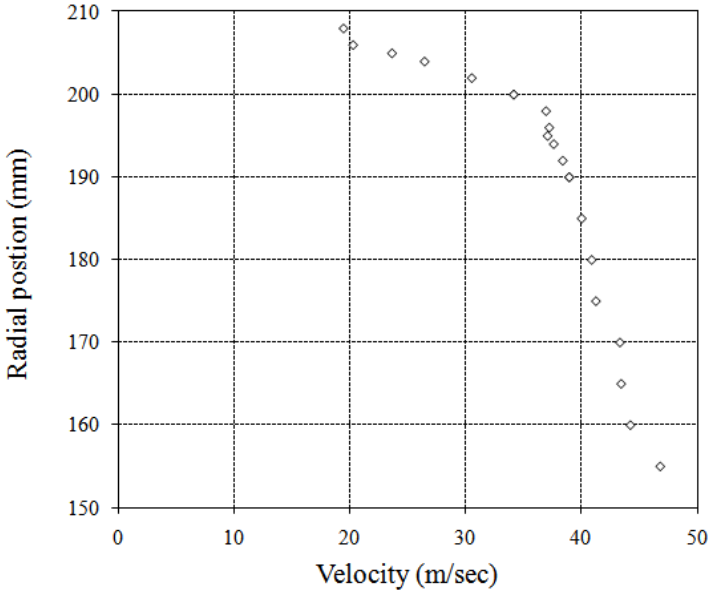

Figure 4.11: Mean axial velocity for various radial positions at 2.8 kg/sec mass flow rate

purely sinusoidal, but that it represented a slightly rectangular, or even saw tooth form. With the confirmation that the excitation frequencies were clearly detectable, the velocity profiles were analysed in more detail.

4.4.4 Results: Velocity perturbation profiles

It is known that flow in front of the first stage rotor is axial, and it was assumed that the velocity perturbation due to excitation approximately 90 mm downstream of the nozzle, would also be axial. The graphs in Appendices B, C and D report the axial velocity perturbation relative to the mean velocity on the x-axis and the radial position of the perturbation on the y-axis. The minimum and maximum velocity perturbation for each radial position were plotted and connected with a bar, to indicate cycling between the minimum and maximum. Figure 4.11 shows the axial velocity profile without excitation and a clean inlet, i.e. with no nozzle partially obstructing air flow. This profile differs from results found by previous tests, like that of Roos (1995). Measurements taken to verify the axial velocity profile are provided in Appendix J.

The results for the axial nozzle (Appendix B) showed that the maximum velocity perturbation occurred at the 0.208 radial position in all cases, which is 2 mm from the blade tip. Figures B.4, B.5 and B.6 of the axial excitation experiments show that increasing the injector mass flow rate at a fixed frequency setting, resulted in a larger velocity perturbation. It also caused an increase in the difference between the mean steady velocity profile and the minimum

velocity. In other words, for higher mass flow rates, the minimum value of the perturbation became significantly more than zero. Figures B.3, B.6 and B.9 show that an increase in excitation frequency at a fixed injector supply mass flow rate, caused the maximum velocity perturbation to decrease slightly and the minimum to increase significantly. At 60 Hz, for example, the minimum value was 6 m/sec higher than the mean velocity profile, while at 1200 Hz it was 20 m/sec higher. For all frequencies and exciter mass flow rate settings, the radial position of the maximum excitation remained at 208 mm. Therefore, for axial excitation, an increase in injector mass flow rate will increase the level of blade excitation and an increase in frequency will decrease the blade excitation level.

The graphs in Appendix C show the velocity perturbations caused by excitation with the radial nozzle. Figures C.4, C.5 and C.6 show that, at a constant frequency, an increase in the mass flow rate causes the area of the highest velocity perturbation to be closer to the blade root. It is also clear that the maximum velocity perturbation remained approximately 25 m/sec in all three cases. Therefore, because of the higher bending moment associated with a force closer to the blade tip, it appears that a lower radial injector mass flow rate will result in a higher level of blade excitation. A comparison of figures C.3, C.6 and C.9 show that an increase in frequency at a fixed injector mass flow rate, results in a decrease in the magnitude of the velocity perturbations. It also shows that an increase in frequency did not cause the position of the maximum perturbation to vary significantly.

A comparison of the production axial excitation results presented in Appendix D, suggests at first glance that this nozzle was not as successful as the first prototype axial nozzle at producing velocity perturbations focussed on the blade tip. Results show that the maximum velocity perturbation occurred at the 0.19 m radial position, one third the length of the blade from the blade tip. It must be noted at this point, that the system was designed for a compressor that operates at transonic axial velocities. At high axial velocities, the injected air will be 'pushed' against the casing, resulting in a perturbation that will be more focussed on the blade tip. Therefore, in a transonic compressor, the production axial nozzle will most likely perform as good, or even better than the prototype axial nozzle.

Figures D.2, D.3 and D.4 of the production axial excitation tests show that increasing the injector mass flow rate at a fixed frequency setting, resulted in a larger velocity perturbation. It also caused an increase in the difference between the mean steady velocity profile and the minimum velocity. Figures D.1, D.4 and D.5 of the production axial nozzle, show that an increase in excitation frequency caused the maximum velocity perturbation value to decrease slightly and the minimum perturbation value to increase significantly.

Therefore, the excitation by means of the production axial nozzle will increase as the injector mass flow rate is increased and will decrease as the excitation frequency is increased.

4.5 Characterisation of exciter nozzle velocity variations

As explained in the methodology chapter (Chapter 3), the injection nozzle inlet boundary conditions were based on experimentally measured nozzle velocity variations. Due to spatial and technical limitations, it was not possible to measure the nozzle velocity variation whilst operating inside the compressor. These experiments were therefore done on a test bench outside of the compressor. Another limitation was the size of the hotwire compared to the nozzle diameter. The nozzle diameters are approximately 4 mm and the hot wire length is about 3 mm. Relative to the nozzle diameter the hot wire is large, which meant that it could not capture the velocity fluctuations accurately in the presence of significant turbulence. However, given the limitations, an attempt was made to measure the injector nozzle velocity profiles. This served as a starting point from where the simulation nozzle velocity profiles were iteratively altered.

Similar to the nozzle velocity profiles, an attempt was made to measure the temperature profiles associated with the velocity variations with a thermocouple. Due to the sampling rate limitations of the temperature measuring equipment, only the mean temperature could be measured. Similar to the velocity variation profile, the temperature results were also used for the specification of the nozzle inlet boundary conditions in the set-up of the CFD model.

4.5.1 Description

For the axial and radial nozzles, the hot wire and the thermocouple were positioned 2 mm away from the nozzles, in line with the extended centre lines of the nozzles. For the production axial nozzle, it was not yet known to what extent the air flow was deflected by the nozzle shape. To measure the flow direction and velocity variations of the production axial nozzle, a hot wire x-probe was utilised. The position of highest velocity was determined by inspection and the test bench was set up as depicted in figure A.6. The thermocouple was positioned as indicated in the figure.

As with the excitation velocity profile tests, each nozzle was tested at 60 Hz, 650 Hz and 1200 Hz, with the injector supply rate set to 23.8 x10^{-3} kg/sec.

At 650 Hz, each nozzle was also tested at an injector air supply rate of 13.8 and 19.9 x10^{-3} kg/sec.

4.5.2 Results

The results in Appendix M show that in most cases, for all frequency and mass flow rate settings, the variation in the velocity took on the form of an approximate sinusoidal wave. Figure 4.12 gives the result for 60 Hz radial excitation at 23.8 x 10^{-3} kg/sec, clearly showing the sinusoidal wave form. For high frequency and mass flow rate settings of the axial nozzle the wave form became distorted, which was probably due to turbulent flow at the nozzle exit as a result of the 90° bend in the nozzle. Also, for all nozzles and settings, it was clear that the valve mechanism did not ensure a minimum velocity of zero. Instead, it was more in the region of 25 to 50 m/sec, even as high as 160 m/sec for high frequency and mass flow rate settings of the axial nozzle.

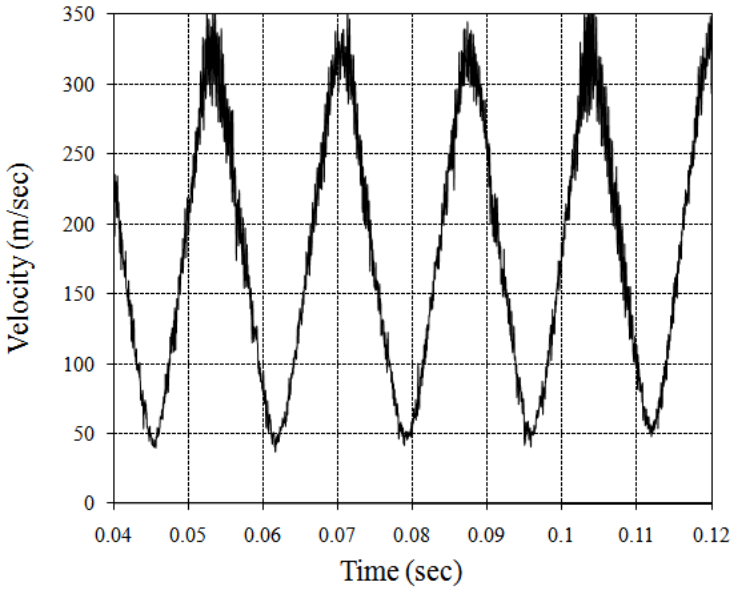

Figure 4.12: Radial nozzle velocity profile near the nozzle outlet with a 60 Hz excitation and a supply mass flow rate of 23.8 x 10^{-3} kg/sec

Along with the velocity variation, Appendix M also gives the variation in flow direction of the production axial nozzle. The graphs show that the angle varied around 0°, with periodic increases of up to 25° with respect to the direction of axial flow. These peaks coincided with the periodic increase in velocity during one excitation cycle.

The results from the temperature measurements are presented in table 4.2. The table shows that the average temperature decreases as the nozzle exit velocity increases. For the axial excitation unsteady simulations, the temperatures were assumed to be the same as those measured for the production axial nozzle. During the testing it was noted that the measured temperatures increased when the exciter was operated for extended periods, typically 3 to 5 minutes. This occurred as a result of energy released by friction inside the valve mechanism. All results listed in table 4.2 were therefore taken after allowing a sufficient cooling down period.

Table 4.2: Temperature results for characterisation tests for CFD purposes

Excitation Frequency (Hz)	Mass flow rate (x 10^{-3} kg/sec)	Prod. Axial nozzle Temperature ($^\circ$)	Radial nozzle Temperature ($^\circ$)
60	23.8	10.4	9
650	13.8	16.6	15
	19.9	12.8	10
	23.8	10.1	9
1200	23.8	8.2	7

4.6 Blade Deflection and Vibration

The blade deflection and vibration were measured by the half-bridge strain gauge arrangements on blades 3 and 25 of the first stage rotor (see section 4.3.2). The blade deflection and vibration measurements consisted of three phases.

Phase 1 entailed an impact test with the blades stationary, to verify the ability of the vibration measuring system to record the high frequency vibration of the first mode flapping frequency.

In the second phase, the strain-gauged blades were positioned in front of a single axial exciter. The exciter was then operated at various settings while the blade was kept stationary. The purpose of this test was to evaluate the effectiveness of the strain gauges to record vibration and also a preliminary evaluation of the excitation concept.

In the third phase, the compressor was operated without the presence of any excitation at a speed of 3000 RPM. The mass flow rate was decreased from a very high mass flow rate to the point when compressor stall occurred. The aim of this test was to establish a baseline of blade deflection and vibration

during various points of operation without any excitation. The processed data in 4.6.4 shows the blade deflection and FFTs of the blade deflection for various mass flow rates at 3000 RPM.

4.6.1 Half-bridge strain gauge calibration

The strain gauge measuring system was calibrated by applying a known force to the tip of the blade. This was done by pulling the blade with a chain hoist via a spring scale. The blade tip displacement was measured with a dial gauge and the displacement and corresponding strain gauge voltage output was then recorded.

For the calibration, the blade was considered to be a simple cantilever beam that bends perpendicular to its attachment point, the blade root. Due to spatial constraints, the force could not be applied perpendicular to the blade root. The force vector perpendicular to the blade root was considered for all calculations and the force component along the blade root axis was ignored. The resulting blade tip displacement was measured perpendicular to the axis of the blade root.

Figures 4.13 and 4.14 show the relationship between tip displacement and strain gauge voltage output for blade 3 and blade 25 respectively. The graphs suggest that a linear relationship exists between blade tip displacement and voltage output. The relationship for each blade can be described as:

Blade 3: Tip displacement = 0.1468 x Strain gauge voltage output

Blade 25: Tip displacement = 0.1871 x Strain gauge voltage output

The relationship between the tip load and the tip displacement is presented in Appendix E. All further measurements of tip displacement and blade vibration will be given in terms of blade tip in the direction of displacement perpendicular to the blade root.

4.6.2 Phase 1: Impact test

4.6.2.1 Experimental procedure

The compressor casing was removed for the impact test, in order to expose the blades. The blade being tested was deflected manually and then suddenly released, similar to the action of plucking a guitar string. The blade deflection output from the strain gauges was recorded.

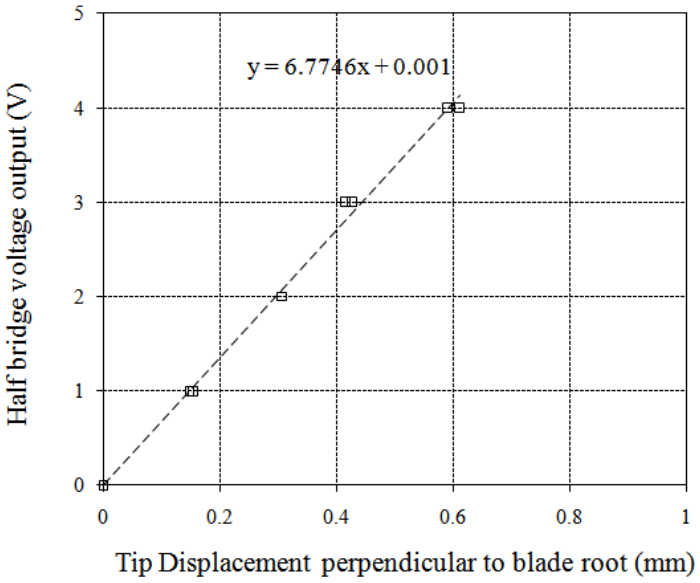

Figure 4.13: Blade 3 tip displacement perpendicular to blade root vs half bridge voltage output

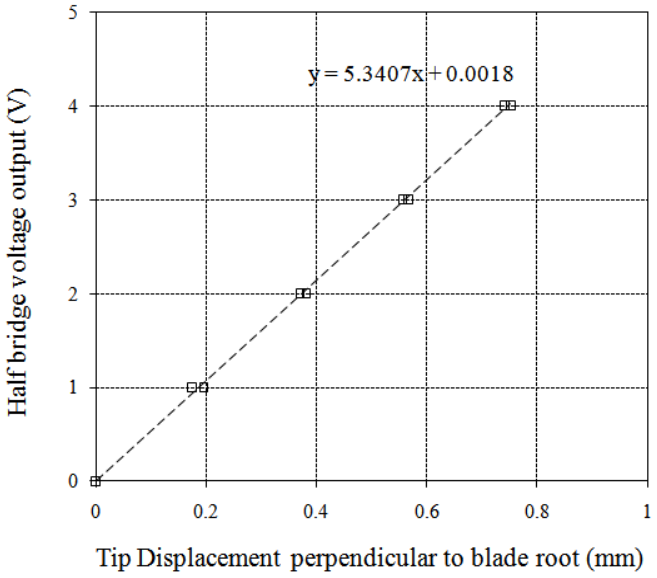

Figure 4.14: Blade 25 tip displacement perpendicular to blade root vs half bridge voltage output

4.6.2.2 Test results

Figure 4.15 shows the result of the impact test for blade 3. As expected, the tip displacement decayed exponentially. An investigation into the period of the cycle shows that it was 1.5 x10^{-3} sec. When converted into the frequency this equates to 654 Hz, the first mode flapping frequency. It is noted that this number is slightly more than the initial measurement of 642 Hz (Duvenhage, 2009). Considering however, that these measurements were taken before the blade was fitted with the strain gauges, it is possible that the difference can be attributed to a change in the blade property, as a result of the strain gauges.

Blade 25 gave a similar output, exhibiting the same exponential decay as blade 3, but with a natural frequency of 649 Hz. Figures 4.16 and 4.17 give the FFTs of the impact test strain gauge output. These graphs clearly show the first mode flapping natural frequency for blade 25 and blade 3 respectively.

4.6.3 Phase 2: Single exciter testing

4.6.3.1 Experimental procedure and test points

A single exciter was fitted to attachment point 15 on the compressor bell-mouth. Blades 3 and 25 were then respectively positioned directly in the flow path of the injector nozzle. This test was only done with the axial injector nozzle, as the radial injector injects air towards the hub and would only be effective when the compressor was running and the air moving towards the blades. The position of the exciter with respect to the rotor blade was identical to that of the exciter characterisation with the hot wire (figure A.3 in Appendix A).

Each blade was exposed to excitation at various frequencies and mass flow rate settings. These test points were similar to the test points used for the characterisation of the exciters as described in section 4.4, except for the fact that the frequency settings of 300 Hz, 659 Hz and 900 Hz, were also included. The test points were therefore 60 Hz, 300, Hz, 650 Hz, 900 Hz and 1200 Hz and at each frequency setting the injector supply mass flow rate was set to 12.8, 19.9 and 23.8 x10^{-3} kg/sec.

4.6.3.2 Test results

All the results show that the excitation frequency was detectable on the FFT. Figure 4.18 illustrates the FFT of the tip displacement perpendicular to blade root of blade 3, as a result of 300 Hz excitation at 23.8 x 10^{-3} kg/sec. The peak in the region of 650 Hz shows that the first flapping mode frequency was

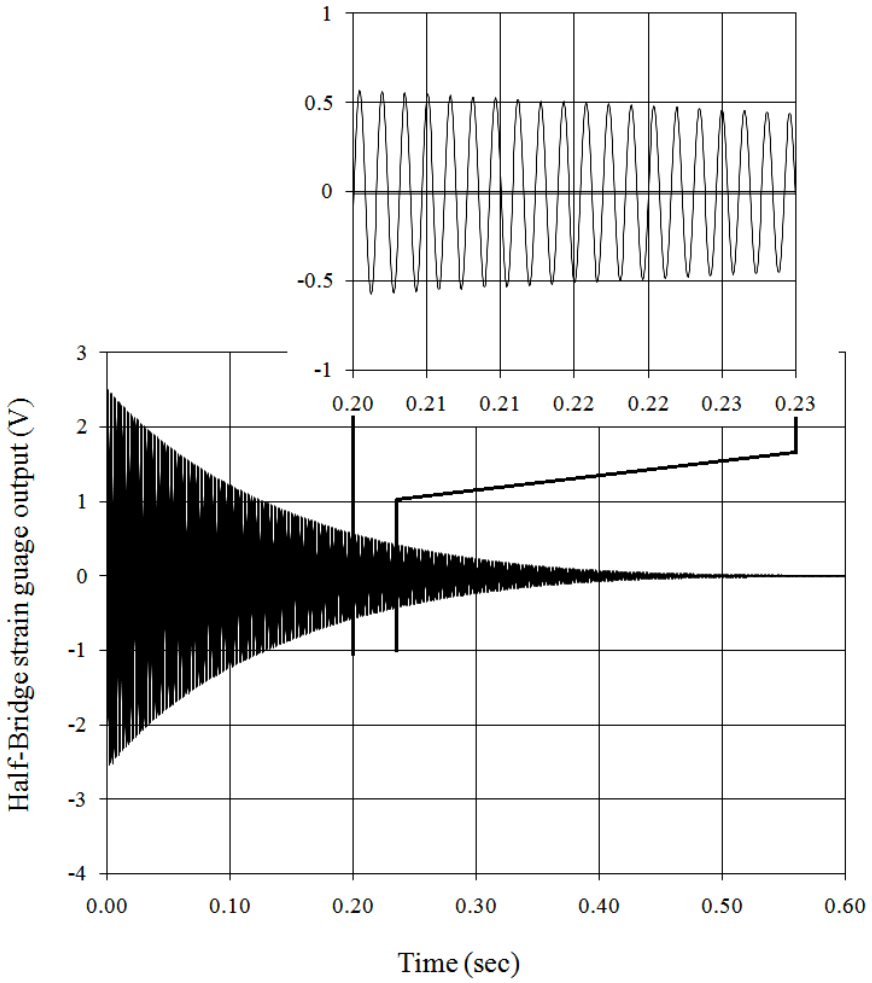

Figure 4.15: Strain gauge half-bridge response to impact test on blade 3

excited by exposing the blade to a 300 Hz excitation. The natural frequency was present as the most prominent frequency, with the excitation frequency visible to a lesser extent. The first harmonic of the excitation frequency was also prominent.

Figure 4.19 illustrates the FFT of the tip displacement perpendicular to the blade root of blade 25, as a result of 300 Hz excitation at 23.8 x 10^{-3} kg/sec. This graph shows similar behaviour when compared to blade 3. The natural frequency was present as the most prominent frequency, while the first harmonic of the excitation frequency was also very prominent.

Figures 4.20 and 4.21 show a comparison of the blade tip amplitudes at the excitation frequency measured for various excitation frequencies and mass flow rate settings. It shows that a fixed injector mass flow rate setting resulted in significantly larger blade vibration amplitudes when the excitation frequency

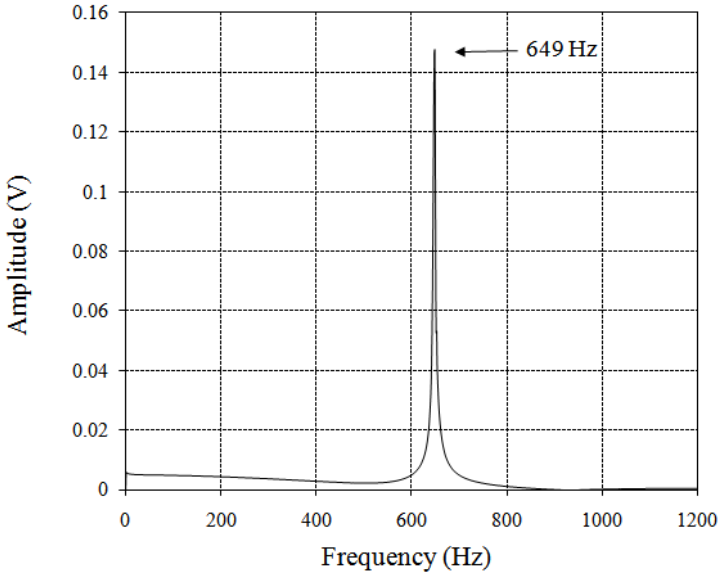

Figure 4.16: FFT of the half-bridge strain gauge impact test output of blade 25

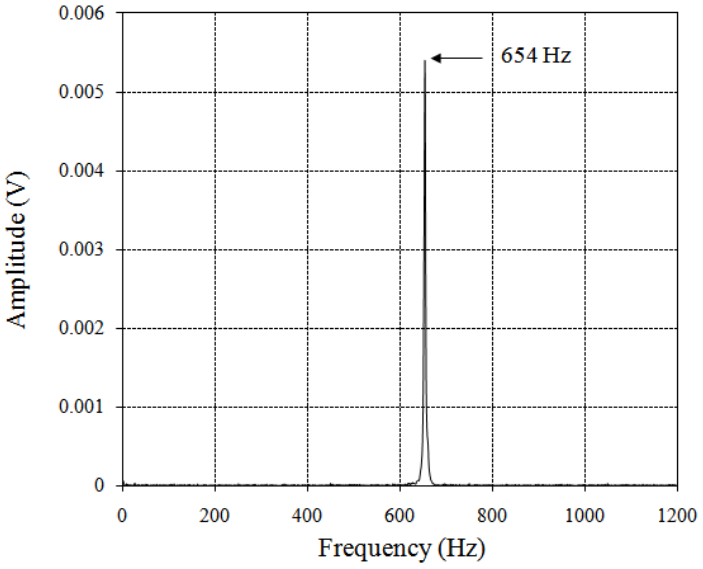

Figure 4.17: FFT of the half-bridge strain gauge impact test output of blade 3

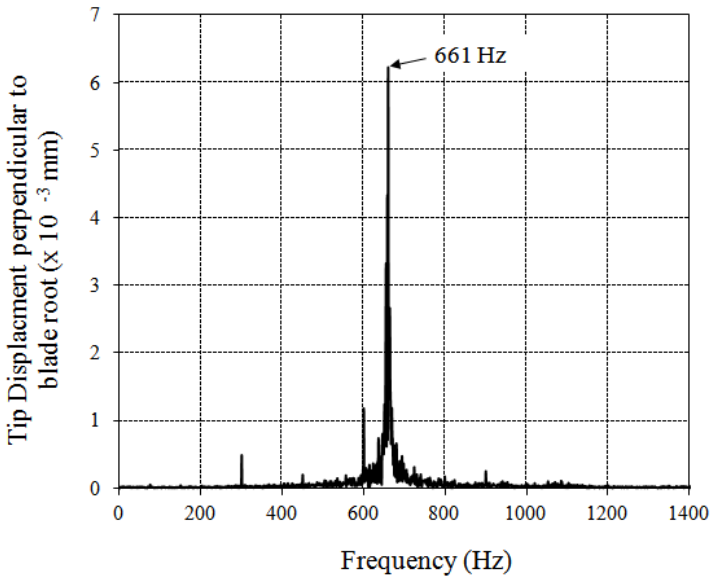

Figure 4.18: FFT of the blade 3 tip displacement perpendicular to blade root as a result of 300 Hz axial excitation with a supply mass flow rate of 23.8 x 10^{-3} kg/sec, with the blade stationary

approached the blade natural frequency. It also shows that an increase in injector mass flow rate at a fixed excitation frequency resulted in an increase in the blade vibration amplitude.

Appendix E presents a comparison of the blade tip displacement amplitudes at the natural frequency (first flapping mode of approximately 650 Hz), measured for various excitation frequencies and mass flow rate settings. It shows that the vibration amplitude at the blade natural frequency increased when the excitation frequency approached the value of the blade natural frequency. Various excitation frequencies were tested at a fixed injector mass flow rate setting. It also shows that an increase in injector mass flow rate at a fixed excitation frequency, resulted in an increase in the blade vibration amplitude.

Furthermore, Appendix E presents a comparison of the blade tip displacement amplitudes at the first harmonic of the excitation frequency. The behaviour of the blade at the first harmonic of the excitation frequency is similar to the behaviour at the blade natural frequency and the excitation frequency.

4.6.3.3 Conclusions from results

The results suggested that excitation at any frequency from 60 Hz to 1200 Hz, will excite vibration at the natural frequency. Excitation frequencies closer to

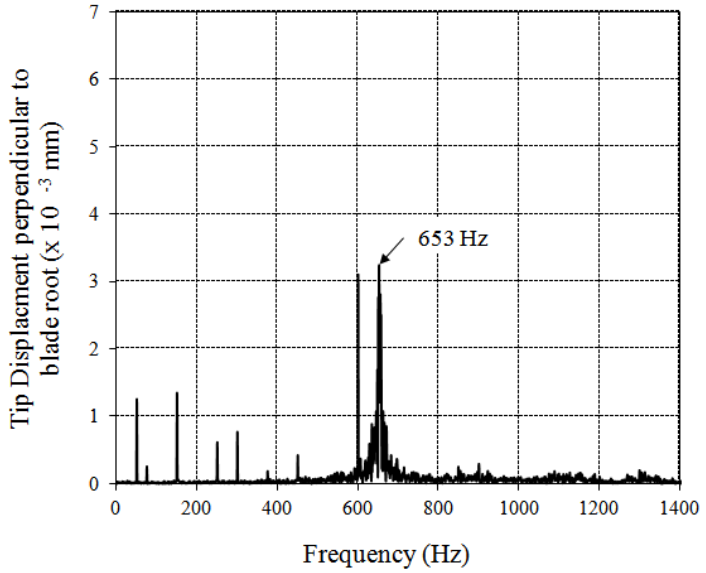

Figure 4.19: FFT of the blade 25 tip displacement perpendicular to blade root as a result of 300 Hz axial excitation with a supply mass flow rate of 23.8 x 10^{-3} kg/sec, with the blade stationary

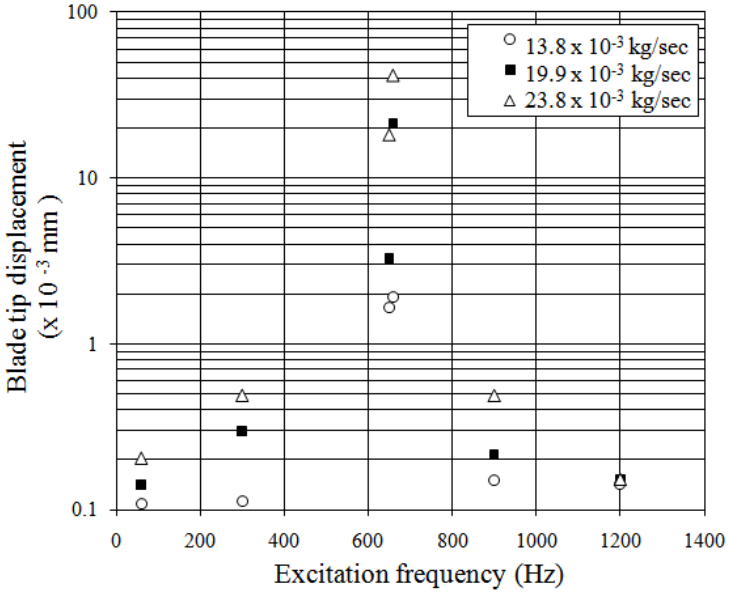

Figure 4.20: Summary of blade 3 tip displacement vibration amplitude at the excitation frequency plotted for various excitation frequencies and supply mass flow rates

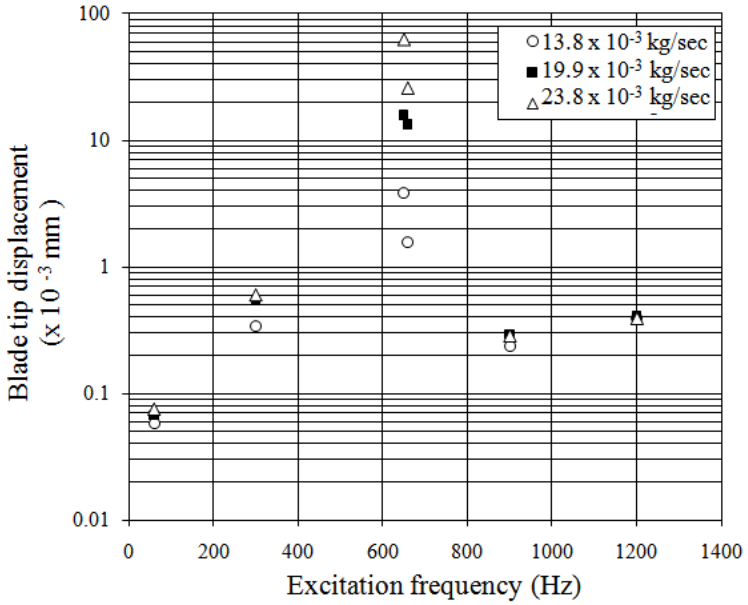

Figure 4.21: Summary of blade 25 tip displacement vibration amplitude at the excitation frequency plotted for various excitation frequencies and supply mass flow rates

the natural frequency resulted in higher amplitudes of vibration at the natural frequency. The results also showed that an increase in the injector mass flow rate cause a higher level of excitation (higher vibration amplitudes). The testing with the blade stationary suggested that the strain gauge half-bridge arrangements worked effectively as a vibration monitoring system and that blade vibration with the compressor rotating should be detectable.

4.6.4 Phase 3: Vibration and deflection baseline at operating design point

The aim of Phase 3 was to do the final verification of the strain gauge vibration measuring system and to establish a baseline of the blade vibration and deflection characteristics. For these tests the compressor was operated through its complete range of mass flow rate settings at 3000 RPM. The blade response to the change in compressor performance was analysed in terms of blade mean deflection and blade vibration.

4.6.4.1 Experimental procedure and test points

The compressor speed was set to 3000 RPM and the mass flow rate was decreased from the maximum achievable setting of 3.075 kg/sec to the point of compressor stall. Compressor stall initiated around 0.9 kg/sec, reaching full stall at 0.788 kg/sec. Table 4.3 describes the mass flow rate settings of the various test points.

Table 4.3: Mass flow rate settings for vibration and deflection baseline test

Mass flow rate (kg/sec)		
3.073	3.068	3.059
3.043	3.014	2.976
2.936	2.880	2.799
2.729	2.673	2.585
2.436	2.223	1.938
1.601	0.992	0.788

4.6.4.2 Test results

Figure 4.22 illustrates the results of the blade tip deflection as a function of the mass flow rate for both blade 3 and blade 25. The blade tip deflection increased as the mass flow rate decreased, until the point of stall was reached. This was the result of an increase in the load on the blade associated with the pressure ratio increase at lower mass flow rate settings. When the compressor entered stall at approximately 0.9 kg/sec, separation around the blade caused the load on the blade to decrease. The decrease in the blade load resulted in a decrease in the blade tip deflection. While the mean blade load in the region of the stall decreased, the blade vibration at its natural frequency increased sharply (see figure 4.23). This was most likely the result of blade excitation that occurred because of a rotating stall cell circulating inside the stage. The possible presence of a rotating stall will be discussed in more detail later in this section.

Figure 4.23 illustrates the amplitude of the blade vibration at the natural frequency (expressed in terms of blade tip deflection perpendicular to the blade root), as a function of mass flow rate. These results were obtained by performing an FFT of the blade deflection data and then plotting the amplitude of vibration at the natural frequency. The graph shows that the blade vibration decreased as the mass flow rate decreased and the load on the blade increased. This suggests that an increase in the blade load, also led to an increase in the damping of the blade. When the blade stalled and the load decreased rapidly, the damping decreased and the blade vibration intensified. Probably even more important, as mentioned before, the presence of a rotating stall cell

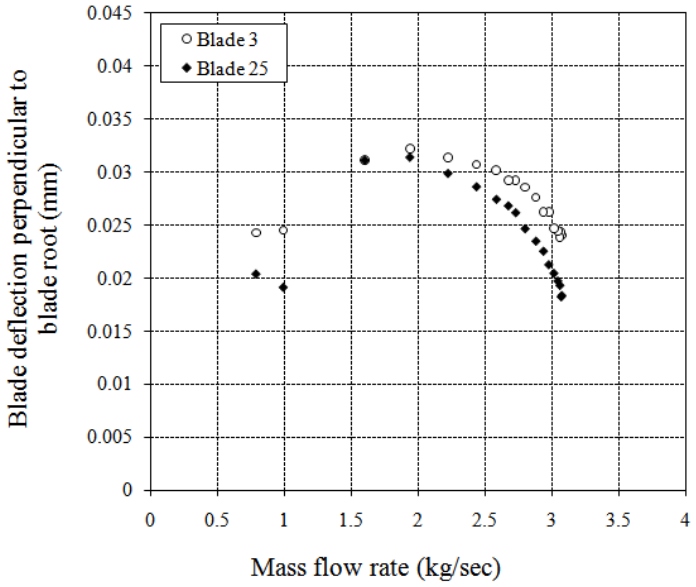

Figure 4.22: Mean blade tip deflection perpendicular to the blade root for various mass flow rate settings at 3000 RPM

could have acted as a means of vibration excitation, which would have also caused blade vibration to intensify.

Figure 4.24 illustrates the effect of the compressor mass flow rate on the mean tip deflection and vibration of blade 3. The blade tip response at 3.068 kg/sec and 0.788 kg/sec are plotted for a time span of 0.004 seconds. Figure 4.24 shows that while both settings had approximately the same mean value, the amplitude of the blade vibration at 0.788 kg/sec was significantly higher. The periods of both waves (0.0015 sec) confirm that the blade was vibrating at its natural frequency of approximately 650 Hz. It can also be seen that the 0.788 kg/sec wave had an underlying vibration with a period of approximately 0.033 sec. This period equates to a frequency of 30 Hz. According to Japikse and Baines (1994), a single rotating stall cell circulates along the circumference of the compressor at a fraction of the rotation speed. The 30 Hz vibration in the blades possibly indicates the presence of a rotating stall cell. In these tests the compressor rotation speed was set at 50 Hz (3000 RPM). A rotating stall cell of 30 Hz therefore represents a fraction of 0.6 of the rotation speed. Figure 4.25 illustrates an FFT of the blade deflection at 0.788 kg/sec. It clearly shows the 650 Hz blade natural frequency, the 30 Hz stall cell rotational frequency that excited blade vibration and also the compressor speed of 50 Hz.

As further verification of the blade deflection, the measured results were correlated with a CFD model of the Rofanco compressor. The results from the CFD simulations (as described in section 5.2.2.2), were used to determine

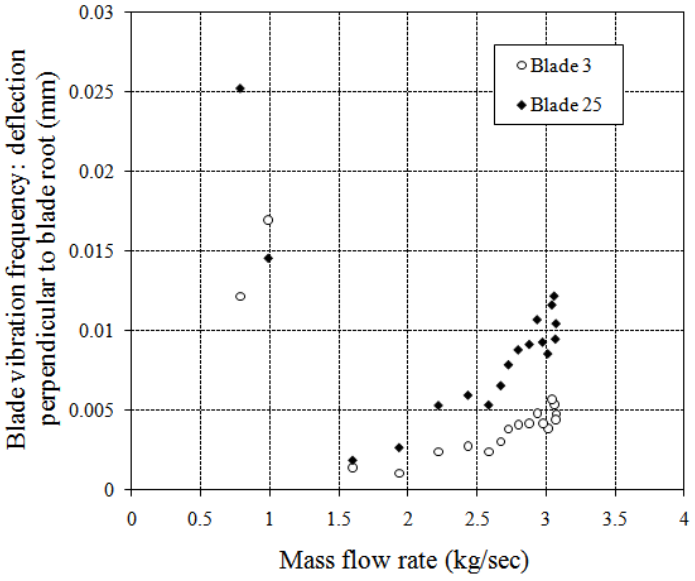

Figure 4.23: Amplitude of blade vibration for various mass flow rate settings at 3000 RPM: blade tip deflection perpendicular to the blade root

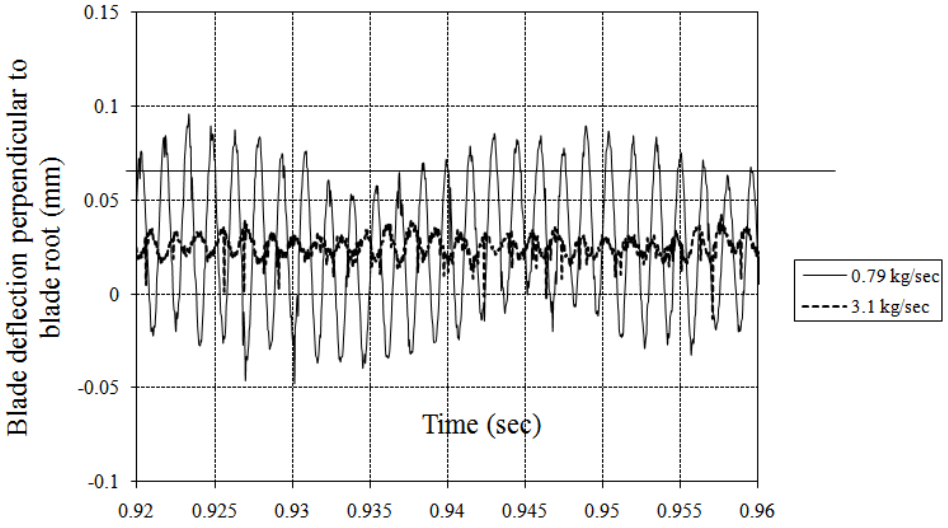

Figure 4.24: Time dependant variation in the blade tip deflection as measure for blade 3 at 3.068 kg/sec and 0.788 kg/sec compressor mass flow rate

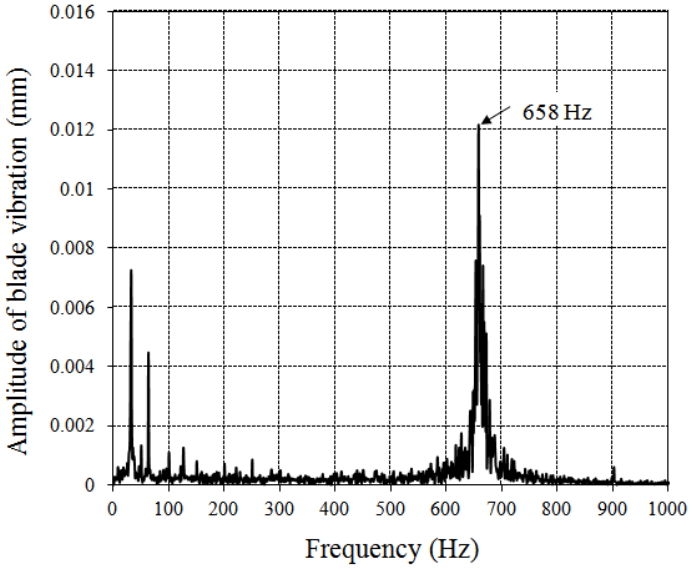

Figure 4.25: FFT of the blade tip deflection at 0.788 kg/sec compressor mass flow rate

the blade force on a blade for various mass flow rate settings. The force output from the simulation was presented as the resultant force acting on the centre of mass of the blade. Taking into account the length of the moment arm, this force was converted to a force that acted on the blade tip to make it comparable with results from experimental data. Experimental blade force results were determined by using the calibration data in Appendix E. A comparison of the simulation output and the experimental results is provided in Figure 4.26. It shows that the experimental and CFD results did indeed differ in magnitude, but that it was of the same order of magnitude. It also showed the same trend of an increase in blade force as the pressure ratio was increased.

4.7 Summary

The test results suggest that excitation at any frequency from 60 Hz to 1200 Hz will induce vibration at the natural frequency. Excitation frequencies closer to the natural frequency resulted in higher amplitudes of vibration at the natural frequency. The results showed that an increase in the injector mass flow rate causes a higher level of excitation (higher vibration amplitudes). The testing with the blades stationary suggests that the strain gauges are suitable for the purpose of vibration measurement and that blade vibration with the compressor rotating will be detectable.

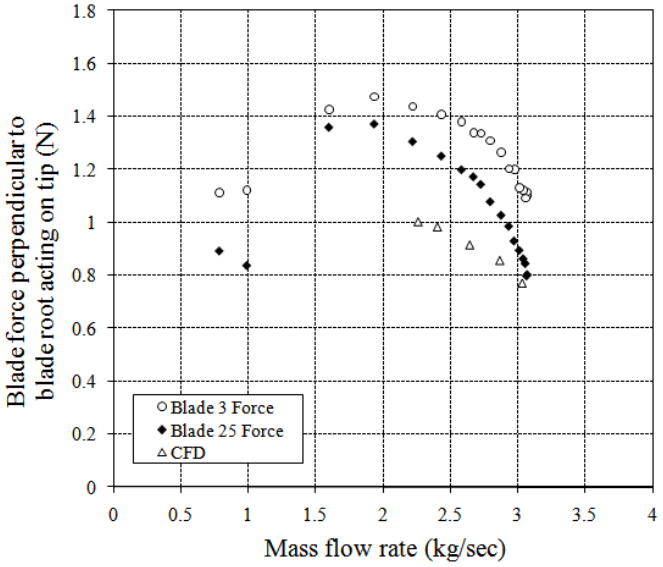

Figure 4.26: Equivalent force at blade tip perpendicular to the blade root for various mass flow rate settings at 3000 RPM: comparison of experimental and CFD results

The experimental test results showed that the strain gauges performed satisfactory as a means of measuring blade vibration and blade tip displacement. A simple impact test confirmed that the blade natural frequency (first flapping mode) was measurable with reasonable accuracy. The blade vibration and tip displacements at various mass flow rate settings produced results that correlated with what could be expected from the compressor blades. These results confirmed that the strain gauge and slip ring system worked effectively as a blade vibration and deflection measurement system.

Chapter 5

Simulation

5.1 Introduction

This chapter describes the modelling and simulation, in CFD, of the effect of the various vibration exciters on the flow around the first stage rotor blades of the Rofanco compressor. The simulation was performed using the Numeca FINE™/Turbo version 8.83 software package. The ideal would have been to model a complete compressor with all the exciters included. However, because of computer processing limitations, a sector of only 3 first stage rotor blades containing 1 exciter outlet was modelled.

The basic construction of the model is described first, followed by an evaluation of the effect of certain grid and solver settings on the simulation performance. A description of the construction of the unsteady simulation grid is then provided. Finally, this chapter includes a description on the modelling of the three injector nozzle types; namely the radial, axial and final production axial.

The effect of the nozzles was evaluated by comparing the variation in the force experienced by the blade. As an initial assessment, the variation in the blade force for one revolution was determined by performing axial excitation at 650 Hz. An FFT of the blade force response revealed that the bypass frequency of the exciter nozzles, 700 Hz (14 exciters x 50 Hz rotation speed = 700 Hz) and its first harmonic, 1400 Hz, were more prominent than the excitation frequency itself. The close proximity of the excitation frequency of 650 Hz to the 700 Hz bypass frequency, posed the risk that one might affect the other and the results might therefore have been misleading. It was therefore decided to perform the comparison of the various nozzles at 1200 Hz excitation. This would ensure that the excitation frequency was clearly distinguishable from the 700 Hz and 1400 Hz peaks.

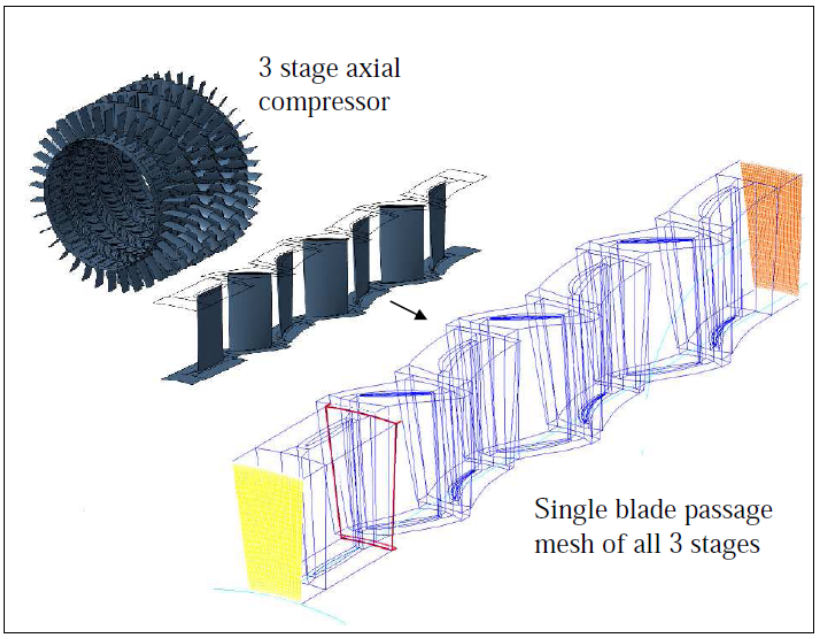

Figure 5.1: Numeca single passage approach to model the Rofanco 3 stage axial compressor

5.2 Model construction and validation

The modelling approach was validated by constructing a model of the full 3 stages of the compressor for only one blade passage. Numeca FINE™/Turbo software sets a periodicity of one blade (i.e. one blade passage is modelled), so that several stages can be modelled with a relatively low memory usage rate (Figure 5.1). Various grid variables and solver settings were investigated and compared to available experimental data. A basic model was constructed to serve as a baseline for comparison with a number of different settings. The following variations were evaluated:

- effect of different solver settings
- effect of the different rotor stator coupling methods
- effect of different wall cell width settings on performance and also on y^+-value
- effect of a variation in the number of flow paths

The optimal settings, as identified through the evaluation, were then incorporated into the final baseline model. This model was used to test several mass flow rate settings at 3000 RPM. The output of this test was plotted to form the model characteristic curve for the pressure ratio and mass flow rate at

3000 RPM. This curve was then compared to experimental test results found by Gill (2006) and Roos (1995).

5.2.1 Baseline model construction

The grid or fluid domain was set up in Numeca AutoGrid5. The grid was constructed around Numeca specific blade profiles, called geomTurbo files. These files were compiled by Gill (2006). A geomTurbo file provides the blade profile and the blade position in the compressor in terms of 3-axis coordinates in text file format. The geomTurbo files for the inlet guide vain (IGV), the 3 rotors and the 3 stators were imported and identified accordingly. The basic model was compiled with the following settings:

- Number of IGVs :36
- Number of rotor blades: 43
- Number of stator blades: 41
- Rotor speed: 3000 RPM
- Number of rotor horizontal flow paths (equal to the number of cells in the radial direction): 61
- Number of stator horizontal flow paths: 53
- Blade tip and hub gaps: Refer to table 5.1 (measured by Gill (2006))
- Wall cell width: 8.7 x 10^{-3} mm

The wall cell thickness was calculated by using equation 5.2.1 (Fin, 2010). The desired y^+ value, denoted by Y_1^+, was chosen and with the reference speed (V_{ref}), reference length (L_{ref}) and fluid viscosity (v) known, the wall cell thickness (y_{wall}) was calculated.

$$y_{wall} = 6(V_{ref}/v)^{-7/8}(L_{ref}/2)^{1/8}Y_1^+ \tag{5.2.1}$$

The three-dimensional mesh was created and the quality report showed that all recommended criteria were met. The quality report is described by table 5.2.

After setting up the mesh, it was imported into the FINE™/Turbo module. This module performs the solving of the CFD model specifically for turbomachinery.

Table 5.1: Average rotor tip gaps and stator hub gaps

	Position					
	R1	S1	R2	S2	R3	S3
Distance (mm)	0.31	0.68	0.37	0.54	0.59	0.50

In FINE™/Turbo, the model was set-up as a steady simulation, with the fluid specified as air with the properties of a real gas. The mathematical model was set to Turbulent Navier-Stokes and the turbulence model was specified as Spalart-Allmaras. The reference properties were set to a pressure of 101 300 Pa and temperature of 293 K. In the rotating machinery module, all rotating blocks were set to -3000 RPM. The rotor-stator interface was specified as conservative coupling by pitch-wise row.

The inlet boundary condition was defined by imposing total quantities and defining the velocity direction in the $z-$direction ($Vz/|V| = 1$). The absolute total temperature was set to 293 K and the absolute total pressure to 101 300 Pa. The turbulent viscosity was left as the default value of 0.0001 m^2/sec. The outlet boundary condition was defined by imposing the mass flow rate and using velocity scaling. The mass flow rate was specified as 2.63 kg/sec and the initial pressure as 101 300 Pa. The periodic boundary condition was left as the default setting. All solid boundary conditions were specified as adiabatic and rotating at a constant speed. The hub and the rotor blades were set to rotate at -3000 RPM, while the hub upstream of the rotor-stator interface, the shroud and the stator blades were set to 0 RPM.

Table 5.2: Quality report: Basic grid

	Reported	Required
Min skewness angle	30 °	$>$ 20 °
Max aspect ratio	780	$<$ 2000
Max expansion ratio	2.2	$<$ 2.5

The numerical model was set to grid level 0 0 0, the finest and final grid level. The number of grid (levels) was set to 3 and coarse grid initialisation was activated to ensure quicker convergence.

Finally, the computation steering was set a maximum of 5000 iterations and the minimum convergence criteria set to the order of -6. The simulation was set to save every 100 iterations.

5.2.2 Baseline model evaluation

The simulation was considered to be converged when the mass flow rate imbalance was less than three orders of the total mass flow rate. This meant that the difference between the inlet mass flow rate and the outlet mass flow rate was less than 0.1 % of the total mass flow rate. In this case, the mass flow rate was approximately 2.6 kg/sec. When the difference between the inlet and the outlet was less than 0.0026 kg/sec, the simulation was considered to be converged. The simulation converged after approximately 2500 iterations. At that point, the residuals were in the order of 10^{-2}.

The simulation produced a pressure ratio of 1.030 when the mass flow rate was set to 2.63 kg/sec. This was slightly higher than the pressure ratio of 1.0287 for a mass flow rate of 2.63 kg/sec, as measured by Roos (1995). Several other variables of the baseline were changed in an effort to improve the correlation of the experimental data with the simulation solutions and also to establish grid and solver setting independence. In this section, the detailed settings of the variations on the baseline model are discussed. For each case, the settings were exactly the same as for the baseline model, with the exception of the single setting or characteristic that was being investigated. All results are presented in table 5.3 along with the baseline model.

5.2.2.1 Evaluation of variations on the baseline model

Appendix F describes how different solver settings and variations on the simulation model were investigated. The variations were evaluated based on their effect on the mass flow rate vs pressure ratio results. Table 5.3 gives a summary of the findings. The results led to the conclusion that the different rotor/stator coupling methods and the tested wall cell widths did not have an appreciable effect on the pressure ratio at a specified mass flow rate. Figure F.1 in section F.2 shows that with respect to y^+ values, the wall cell width settings of 0.00512 mm and 0.0085 mm performed equally well.

Table 5.3: Pressure ratio results for a mass flow rate of 2.63 kg/sec of variations on the baseline model

Setting or variation	Resulting pressure ratio
Flow path 61/73	1.0306
Flow path 33/45	1.0311
Wall Cell	1.0306
Conservative Coupling	1.0306

The investigation of the number of flow paths showed that as long as the number of flow paths was more than 53 for stator blades and 61 for rotor blades, the effect on the pressure ratio was negligible.

5.2.2.2 Comparison of baseline model with experimental data

After testing the various settings, the optimal baseline model was used for further testing in order to correlate the simulation output with experimental test results. Several mass flow rate operating points were simulated and the resulting pressure ratio results were plotted along with the experimental results of Roos (1995) and Gill (2006). Figure 5.2 illustrates a comparison of the baseline simulation model with experimental results. The graph shows that the pressure ratio values determined by simulation were slightly higher than the experimental data in all cases. However, it could still be concluded that a good correlation exists between the simulation output and the experimental data.

5.2.2.3 Summary

Testing of the optimal model at various operating points suggested that the final baseline model was a good representation of the Rofanco compressor. The model could subsequently be used as the baseline from which the unsteady simulation models were constructed.

5.3 Excitation unsteady simulation grid generation

As discussed in the introduction, the aim of this project was to investigate the excitation of rotor blade vibration by means of pulsating air injection. The air injection disturbs the air flow around the blade in order to excite vibration at the pulsating frequency. This section describes how the grid for the unsteady simulation was generated.

The grid for the excitation simulations consisted only of the first rotor blade (no other rotor blades, stator blades or IGVs). The IGVs were omitted because they were removed from the actual compressor to accommodate the exciter injectors. All other blades were left out in order to allow for modelling of the first stage rotor to a grid size that captured as much detail as possible, without compromising the simulation with an extreme time cost.

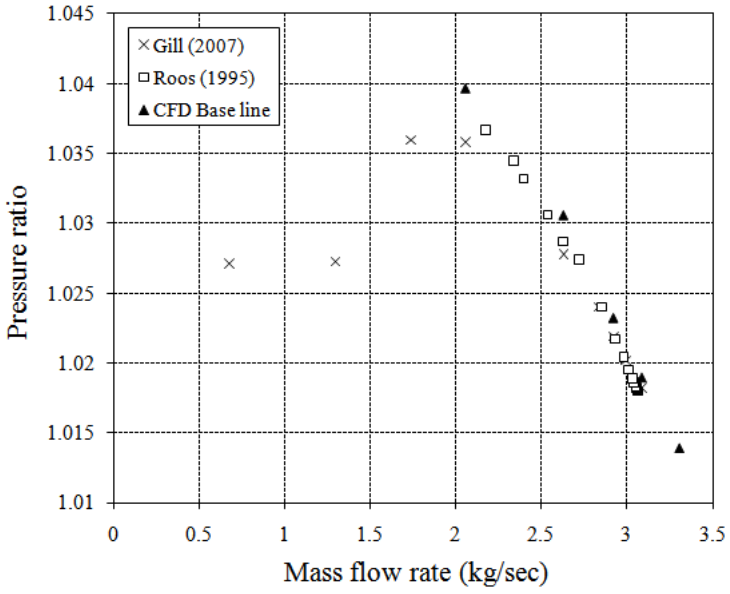

Figure 5.2: Comparison of baseline model results with experimental results

The size of the grid was limited by computer processing power and the time cost to run the simulation. The Stellenbosch high performance computing (HPC) cluster is currently able to process a Numeca simulation with a grid size of approximately 13 million cells. The ideal unsteady model would have consisted of a grid with all three stages and all the blades from each stage. However, because of limitations in computational power and also the time cost of a large model, the grid was reduced to a size that could be managed with the available computational capabilities. This was achieved by making use of periodic boundaries. In order to make use of periodicity of more than one blade passage that allows for unsteady simulation of a full revolution, the total number of blades had to be a multiple of the number of blade passages in the modelled sector. If the periodicity is one blade passage only, the number of time steps is limited to the sliding movement of one blade passage. When the mesh has rotated through the angle of one passage, the mesh moves back to its original position and starts the next cycle.

Another periodicity limitation is that the number of blades in the modelled sector must be less than the periodicity. If this is not the case, the effective periodicity is also only one blade passage and a full revolution cannot be simulated. For example, if a stage of 20 blades is modelled as 4 blades and a periodicity of 5, it would be possible to perform an unsteady simulation of one full revolution or more. If, on the other hand, it is modelled as 5 blades and a periodicity of 4, it would only be possible to perform an unsteady simulation of one blade passage. When the sliding grid reaches the end of the first passage,

it moves back to the initial position.

Applying these constraints to the Rofanco compressor meant that only one rotor stage of the compressor could be modelled. The first rotor stage of 43 blades was then approximated to a total number of either 42 or 44 blades, so that the total number of blades remained a multiple of the number of blades that were modelled. Therefore, if the total number of blades was selected as 42, the number of blade passages that could be modelled was 6 or 3. The periodicity of 7 is then larger than the number of modelled blades in the sector, which meant that a full revolution could be performed. If the number of blades is selected as 44, the maximum number of blades that could be modelled would be 4.

The next constraint was that 15 injectors had to be accommodated by the periodicity and the number of blade passages modelled. If 42 blades and 3 blade passages were modelled, the periodicity was 14, which could not accommodate 15 exciters. If 42 blades and 6 blade passages were modelled, the periodicity would be 7, which could also not accommodate 15 exciters. If 44 blades and 4 blade passages were modelled, the periodicity was 11, which again could not accommodate 15 exciters. The only approach that could accommodate the number of blades and the number of injectors in the periodicity, was to reduce the number of exciters to 14 and model the stage as if it had 42 blades. This gave the option of modelling 6 blade passages and 2 injectors, or 3 blade passages and 1 injector. Taking into account the requirement to minimise the time cost of the unsteady simulation, it was decided to model 3 blade passages and 1 exciter. It will be shown later in this chapter that the high time cost of the unsteady simulations made it imperative to make use of the smallest grid size.

With the total number of blades and the number of blade passages in the sector model clarified, the grid could be generated. For each of the three types of models, a separate grid model was generated. All three were generated by following the same process, with minor variations. Relevant grid parameters, like wall cell width and the number of flow paths were based on the findings from tests with the baseline model.

5.3.1 AutoGrid mesh setup

The first step was to initiate a new grid file in AutoGrid5, by importing the geomTurbo file for the first stage rotor blade. This geomTurbo file had to be modified by extending the hub and the casing 50 mm upstream. This changed the inlet position from the $z-$value of 0 to a value of -50 mm, so that the injectors that were located approximately 80 mm upstream of the first stage

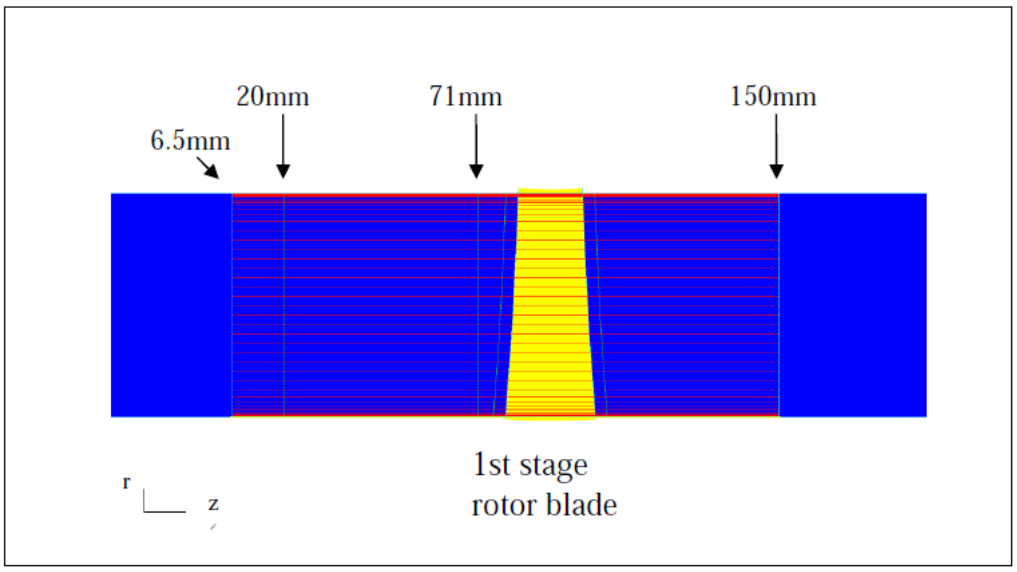

Figure 5.3: Positions of the $z-$constant lines for axial injector mesh

rotor blades, could also be modelled.

The mesh inlet and outlet boundary positions were adjusted to more suitable positions, by changing the inlet and outlet $z-$constant lines for each grid. In the axial mesh, the inlet was placed at 6.5 mm, in the production axial mesh at 10.5 mm and in the radial mesh it was placed at -50 mm. For all three grid models the outlet was placed at 150 mm.

The program was then set to Wizard mode and the following parameters were specified:

- Number of rotor blades: 42
- Rotor speed: 3000 RPM
- Number of horizontal flow paths: 77
- Blade tip gap: 0.31 mm
- Wall cell width: 5.12 x 10^{-3} mm

The next phase was to change the number of blade repetitions to 3 and to add $z-$constant lines near the positions of the nozzles, as well as where the rotor-stator interface would be defined. These positions are indicated in figures 5.3, 5.4 and 5.5.

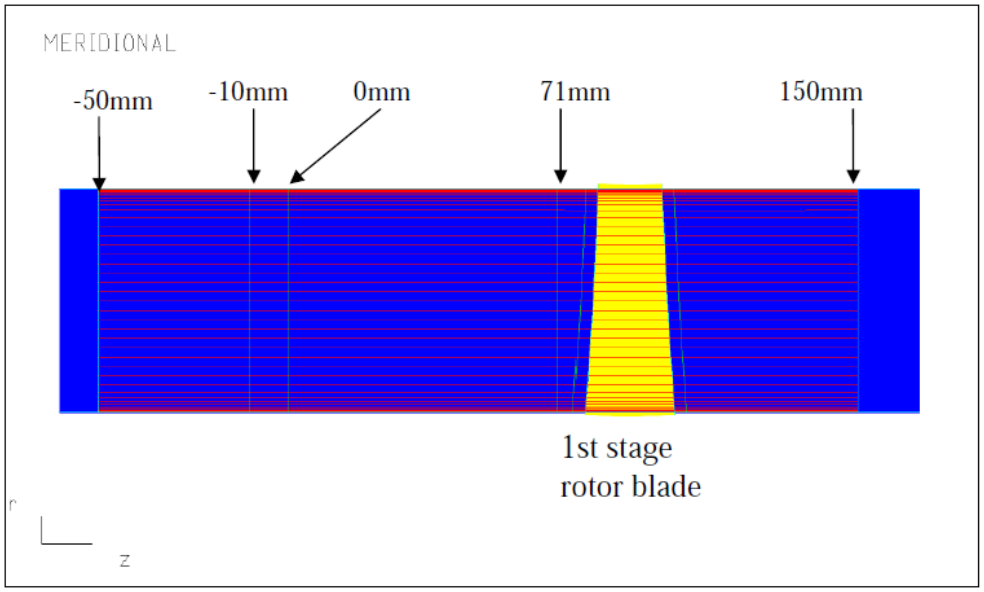

Figure 5.4: Positions of the $z-$constant lines for radial injector mesh

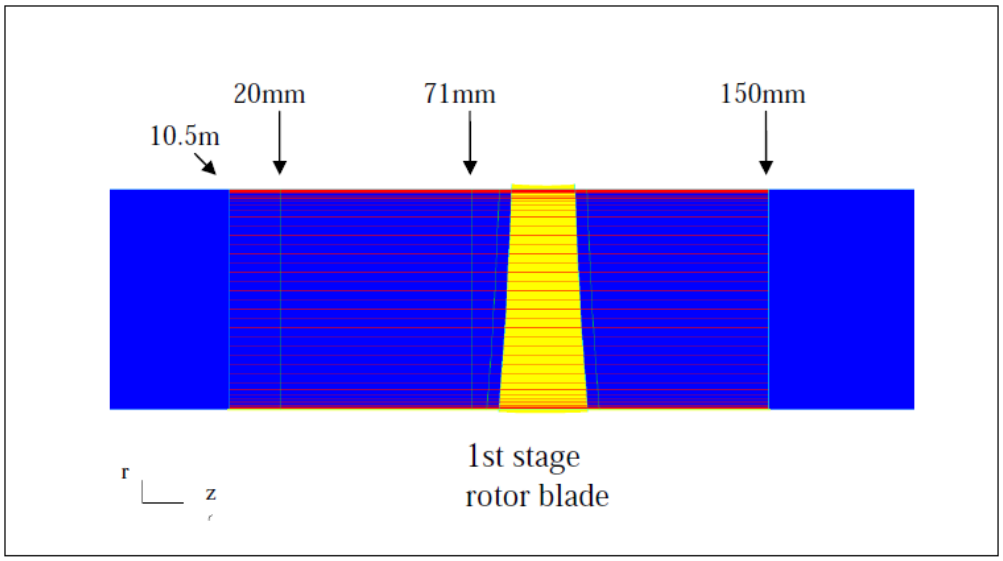

Figure 5.5: Positions of the $z-$constant lines for production axial injector mesh

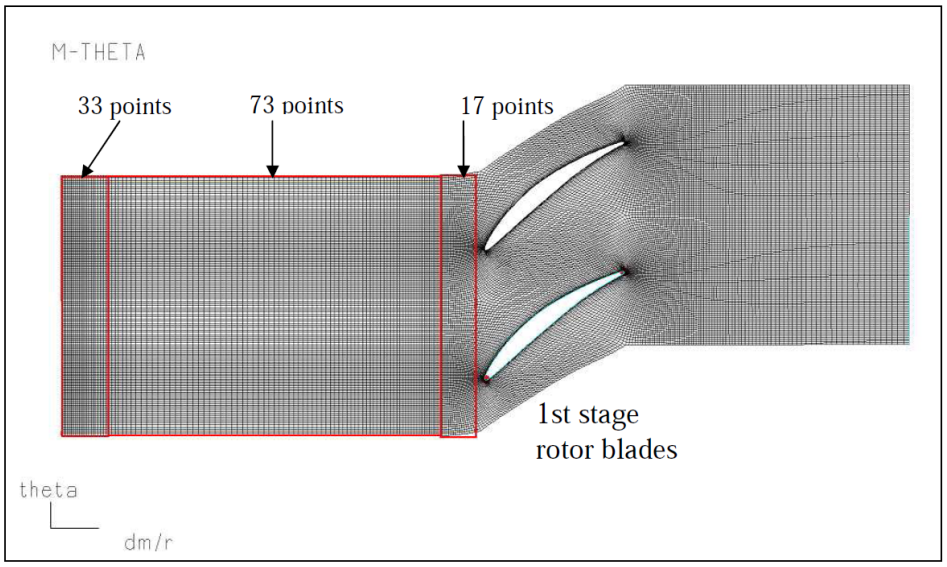

Figure 5.6: Number of points streamwise settings for the axial and the production axial injection mesh

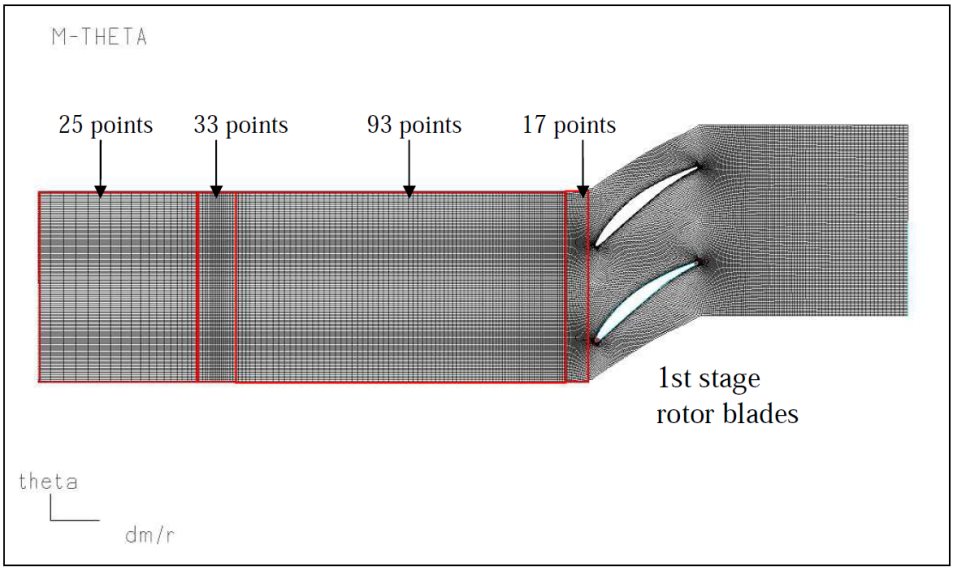

Figure 5.7: Number of points streamwise settings for the radial injection mesh

The new cell size was heavily distorted in the mesh region in front of the rotor blade. To rectify this, the number of stream wise points were changed as indicated in figures 5.6 and 5.7.

The 3-D grid was generated and the quality report showed that all recommended grid quality criteria were met. The creation of the nozzle boundary conditions and the rotor-stator interfaces were performed in IGG and is de-

scribed in the next section.

5.3.2 Grid modification in the Numeca Interactive Geometry Modeller and Grid Generator (IGG)

Before the nozzle boundary could be specified, the periodicity had to be defined. In the Periodicity window in the Grid tab, the periodicity was selected as Rotating Periodicity and the number of periods specified as 14.

A number of cell walls on the inlet boundary patch were re-identified to form the inlet patches for the axial and production axial nozzles. Cell walls on the shroud wall boundary were re-identified to form the inlet patches for the radial nozzle. This approach approximated the circular nozzle shapes as square shapes. Due to a multi grid solver approach in the Numeca FINE™/Turbo, modifying the grid to represent the true circular shape of the nozzles would have added a significant time cost (16 fold) to the processing time.

The nozzle boundary condition was created with the Edit Patch feature in IGG. A patch is in essence one of the sides of a block of cells. The inlet and outlet boundaries are examples of patches. With the Edit Patch feature, an inlet boundary patch was split with horizontal and vertical divisions. One patch then became a group of patches and each patch of the boundary conditions could be defined as required. With this approach, the nozzle inlet boundaries for the axial and the production axial mesh were created by splitting up the inlet patches where the exciters would be located. The dimensions of the split patches are shown in figures N.1 and N.2 in appendix N.

The nozzle inlet boundary for the radial excitation mesh was created by using the same approach of splitting a patch. In this case however, the solid boundary patch of the forward shroud wall was split and the resulting new nozzle patch was redefined as an inlet patch. The dimensions of the split patches are shown in figure N.3 in appendix N.

The rotor-stator interfaces were not generated merely by the presence of the 71 mm $z-$constant line inserted where a rotor-stator interface was required. At the position of the $z-$constant line, an internal face had to be created first. This was done by selecting the Insert Internal Face function in the Quick Access Pad. The block that had to be split was selected and the $z-$value of the split face was selected. (This value was the same number as the number of streamwise points defined in the block directly upstream of the blade shown earlier in figures 5.6 and 5.7).

The next step was to split the block where the face was created. This was done by selecting the block that had to be split and then selecting the Split Block at Internal Face option in the Quick Access Pad. The block was then split at the internal face and two new connecting patches were created at the interface. Following this, the connecting patches had to be redefined as undefined and then redefined as rotor-stator interfaces by using the Define Rotor/Stator Interface function in the Edit Boundary Condition window.

5.4 Excitation simulation steady initial solution

An individual project was created in FINE™/Turbo for each nozzle type. Before commencing the unsteady simulation, a fully converged steady solution was first obtained. The velocity profile of the inlet boundary condition was the same as the steady state profile that was measured during the exciter characterisation experimental tests (Figure 4.11). The use of this profile made the output of the unsteady simulations comparable with the measured experimental results.

The converged steady simulation was specified as the initial solution for the respective unsteady simulations. Each mesh required its own steady initial solution. This section describes the solver set-up for the steady simulation models.

In FINE™/Turbo the models were set up as steady simulations with the fluid specified as air, with the properties of real gas. The mathematical model was set to Turbulent Navier-Stokes and the turbulence model specified as Spalart-Allmaras. The reference properties were set to a pressure of 101 300 Pa and temperature of 293 K.

In the rotating machinery module, all rotating blocks had to be identified and grouped together, after which it was set to -3000 RPM. All stationary blocks were grouped together and set to 0 RPM. Rotor-stator faces were identified and designated as either upstream or downstream and specified accordingly.

The inlet boundary conditions were identified and grouped as either steady flow or injectors. All inlet faces were then specified as Static Quantities Imposed, with the velocity magnitude specified. In the axial and production axial injection meshes, the velocity magnitude in the $z-$direction (Vz) for both the steady flow and the injector faces were defined as the experimentally measured profile (figure 4.11). In the radial mesh, the injector inlet face was specified with a velocity magnitude of -10 m/sec in the $r-$direction (Vr). The outlet

boundary condition was defined by specifying the pressure and imposing a radial equilibrium of 100 089 Pa at a radius of 0.18 m. This value was obtained from the baseline model testing described in section F.4. The periodic boundary conditions were defined as rotating, with boundaries on the right hand side (as viewed in the positive $z-$direction) set to an angle of 25.71428571° and boundaries on the left hand side set to -25.71428571°.

As a result of the manual rotor-stator definition process described earlier, not all solid boundary faces were grouped in the appropriate sections as per the normal Numeca process. Using the filter function, all faces were identified and grouped as a Rotating Hub, Stationary Hub, Rotor, or Shroud. All components were defined as both Adiabatic and Constant Rotation Speed. The rotational speed of the Rotating Hub and Rotors was set to -3000 RPM and that of the Stationary Hub and Shroud set to 0 RPM.

The numerical model was set to a grid level of 0 0 0, the finest and final grid level. The number of grid levels was set to 3 and coarse grid initialisation was activated to ensure quicker convergence.

The simulation was considered to be converged when the mass flow rate balance was less than three orders of the total mass flow rate. The axial exciter models converged after approximately 3500 iterations and the radial exciter model after approximately 2500 iterations.

Results:

It was found that the mass flow rate result was one-seventh of the mass flow rate found for the equivalent baseline model described in section F.4. It was assumed that when specifying the periodicity as explained above, the software calculates the mass flow rate for the number of modelled passages. The total mass flow rate through the compressor is not reflected by the displayed mass flow rate result. The steady simulation results for each model were as follows:

Axial excitation:

- Actual result: Mass flow rate 0.21697 kg/sec, pressure ratio 1.0083
- Corrected result: Mass flow rate 3.0376 kg/sec

Production axial excitation:

- Actual result: Mass flow rate 0.21697 kg/sec, pressure ratio 1.0083
- Corrected mass flow rate result: Mass flow rate 3.0376 kg/sec

Radial excitation:

- Actual result: Mass flow rate 0.21703 kg/sec, pressure ratio 1.0082
- Corrected mass flow rate result: Mass flow rate 3.0384 kg/sec

The mass flow rate for the one stage model compares favourably with the value of 3.01 kg/sec measured during the baseline model testing (section F.4).

5.5 Excitation unsteady simulations solver set-up

With the initial steady solutions available, the three unsteady excitations could be simulated. An initial evaluation was done by simulating 650 Hz excitation, with a supply mass flow rate of 23.8 x 10^{-3}kg/sec per exciter (see chapter 4.4.2 for detail on the mass flow rate settings). The simulation for all three nozzle types were subsequently performed at 1200 Hz excitation, with a supply mass flow rate of 23.8 x 10^{-3}kg/sec per exciter. The injector nozzle inlet boundary velocity variation was approximated as a sinusoidal wave form.

A uniform velocity profile was assumed across the face of the nozzles. This assumption is supported by the findings of Ravinesh *et al.* (2007), who investigated the influence of the nozzle-exit geometric profile on the statistical properties of a turbulent plane jet.

The final wave forms of the nozzle inlet velocity variation were set as follows:

- 650 Hz Axial excitation: $Vz = 81 + 17.5Sin(2\pi 650t)$
- 1200 Hz Axial excitation: $Vz = 79.25 + 15.75Sin(2\pi 1200t)$
- 1200 Hz Radial excitation: $Vr = -177.5 - 147.5Sin(2\pi 1200t)$
- 1200 Hz Production Axial excitation: $Vz = 133.8 + 61Sin(2\pi 1200t)$ and $Vr = -96.25 - 43.75Sin(2\pi 1200t)$ (This resulted in a sinusoidal wave that varied between 208 m/sec and 150 m/sec at an angle of 20° with the shroud.)

For each nozzle type, the impulse amplitude and mean value were iteratively changed after every simulation run to achieve the correct nozzle inlet boundary conditions. The aim was to ensure a good correlation between the simulations and the corresponding experimental data (section 4.4), with respect to the axial velocity perturbation profiles in front of the rotor blades. Figures G.1, G.2 and G.3 in Appendix G illustrate the correlation between the experimental and the final simulation results. With this correlation, the

effect of the velocity perturbations on the air flow around the blade, as well as the resulting forces on the blade could be analysed.

The value for 'number of iterations per time step' (part of the unsteady simulation set-up) is described in detail in section 5.7. The initial solution was specified as the converged steady solution for the respective excitation nozzles described in section 5.4. The choice of the number of angular positions in the computation steering module is discussed in more detail in section 5.6. The expert parameter ICYOUT was assigned a value of 0, so that the output file would not be overwritten after each time step.

5.6 Investigation of time step size

Numeca proposes that, when performing unsteady simulations, the criteria for convergence must be the variation in mass flow, torque or efficiency, rather than the residuals. When the cyclic variation in the chosen parameter converges to a steady pattern, the simulation can be considered to be converged. For this approach, the time step size is not the determining factor, but rather to allow the simulation to run sufficient cycles until the chosen parameter converges to a steady pattern. Numeca proposes 360 angular positions per revolution. An initial run with 10 to 20 iterations per time step should then be performed until the simulation converges, usually after 1 to 2 revolutions. The simulation is then stopped and restarted, using the last step of the initial run as the initial solution and specifying 50 iterations per time step. The simulations for this thesis were performed using this approach. It was found that the initial run converged after approximately 2 revolutions. The final run of 50 iterations per time step showed no tendency to converge any further, but a full revolution with 360 angular positions per revolution was performed nonetheless.

The approach of determining a minimum time step, based on the grid size and flow velocity, was also evaluated. The Numeca FINE™/Turbo unsteady simulation employs the explicit scheme. When using the explicit scheme, the minimum size of the time step Δt is determined by using equation 5.6.1:

$$\Delta t < \Delta x/|u| \tag{5.6.1}$$

where Δx is the cell width and |u| is the mean velocity of the flow through the cell. The cell chosen to determine Δt was located at the injection nozzle inlet boundary condition. At this location the value of $|u|$ is at its highest. From that point onwards, the value of $|u|$ decreases as the injected air mixes with the steady air from the compressor inlet. The highest value for $|u|$ will yield the smallest Δt.

The calculation of the maximum time step size for radial excitation yields a maximum Δt of 1.5 x 10^{-8} sec (Δx = 5.12 x 10^{-8} m, $|u|$ = 325 m/sec). This time step size equates to 1.27 million time steps per revolution. At an average processing time of 5 min per time step, it will take 12 years to complete one full revolution. The obvious solution to this problem is to increase the cell width. The cell width of 5.12 x 10^{-8} m is specified in order to achieve optimal y^+ values. With radial excitation, where air is injected perpendicular to the boundary layer, the wall cell is the first cell of the nozzle inlet. Numeca AutoGrid does not provide the option to modify the mesh to a larger cell size, without deactivating the multigrain solver option and thereby significantly increasing the processing time.

It was therefore necessary to increase the time step size to a value that yielded a processing time cost that was more manageable. According to the stability criteria, the CFL number in the area of the injector nozzle is way above the required value of unity. The solution at the radial nozzle was therefore unstable. However, when shifting the focus to the velocity profile 10 mm in front of the blade, the CFL number was reduced to 0.71 when the number of angular positions were set to 9000. (At this position $|u|$ reached a maximum of 80 m/sec when considering all three nozzle types. Near the blade the cell width was 0.25 mm.) For 9000 angular positions, the time step size was 2.2 x10^{-6} sec.

Another area of concern was the blade trailing and leading edge. In these regions, which represented 5 % of the blade surface, the cell width was as small as 0.05 mm. With a number of angular positions of 9000 and a maximum relative velocity around the blade of 100 m/sec, the CFL number in the region of the blade leading edge and trailing edge went up to a value of 4.4. This meant that the solution was stable for 95 % of the blade surface.

The two approaches yielded very similar results. The 360 angular position approach was however favoured, because in some cases the minimum time step size approach showed no trace of the excitation frequency. It was expected that the excitation frequency would be visible on an FFT of the blade force response, even if it was relatively small compared to other frequencies.

5.7 Investigation of number of sub-iterations per time step

The number of iterations per time step is an integral part of the 360 angular position approach discussed in 5.6. For the minimum time step size approach, the choice of number of iterations per time step is crucial. With too few iter-

ations per time step, significantly different results are obtained. The smaller the time step, the less iterations are required to achieve a solution that is independent of the number of iterations. The effect of the number of iterations per time step was investigated by plotting the variation in the blade force perpendicular to the blade root for a number of time steps. Figure 5.8 illustrates the results of an investigation of a simulation with 1300 angular positions per revolution. It can be seen that the simulation converged at 5 iterations per time step. With this approach, it was found that for 9000 angular positions per revolution, the simulation converged after 3 iterations.

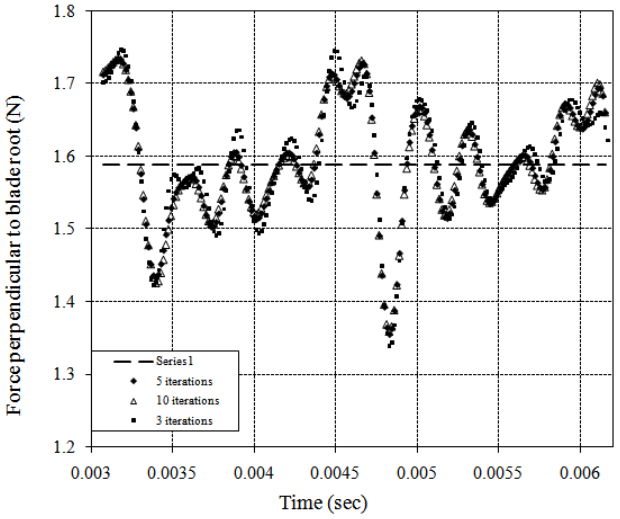

Figure 5.8: Comparison of the variation in blade force over time as a result of 3, 5 and 10 iterations per time step

5.8 Discussion of results

Figure 5.9 is a plot of the force perpendicular to the blade root for 400 time steps, as a result of 650 Hz axial excitation. This figure also presents the profiles of the stream lines and velocity distribution around one specific blade for 4 specific time steps.

The most prominent feature in Figure 5.9, is the 1.34 N minimum force value that the blade experienced at time step 317. The velocity distribution plot shows that the blade entered a region of high velocity flow at this time step. The streamline plot shows that the incidence angle of the flow decreased at this time step, relative to other time steps where higher blade force values were recorded. Therefore, at this time step the decrease in blade force was the result of a decrease in the flow incidence angle and therefore a decrease in the

blade lift force. The decrease in the flow incidence angle was the result of the increase in axial velocity, caused by the axial injection of air.

Furthermore, in figure 5.9, it can be seen that the blade experienced an increase in the flow incidence angle at time step 207 (where the blade experiences a load spike of 1.75 N), which resulted in a higher blade force. In this case however, the associated decrease in velocity is not clearly visible on the velocity distribution plot.

In section 2.5, it was stated that the lift coefficient, C_L, will be influenced by one of two factors; namely the axial velocity in front of the blade (C_a) and the relative absolute velocity of flow over the blade (referred to as the mean velocity vector, W_∞). The analysis above shows that the variation in the axial velocity was the dominant factor influencing C_L and subsequently also the force on the blade. An increase in the axial velocity would result in a decrease in the blade lift force. Further simulation results were analysed only in terms of the blade force response and the resulting frequency response.

5.8.1 Axial excitation unsteady simulation results

The variation in the force perpendicular to the blade root as a result of 650 Hz excitation, was analysed for one revolution (1300 time steps). Figure H.1 illustrates the blade force plotted for one revolution. This graph shows that the blade was exposed to an average force of approximately 1.6 N, with 14 distinct troughs where the blade passed through the injected air stream from the nozzle. Figure 5.10 focuses on the blade force for 100 time steps.

An FFT was subsequently performed on the blade force data. The resulting FFT had a resolution of 50 Hz, because one revolution is a 50^{th} of one second. Figure 5.11 presents the result of the FFT of the force perpendicular to the blade root, caused by 650 Hz axial excitation. It shows that the exciter nozzle bypass frequency, 700 Hz (14 exciters x 50 Hz revolutions = 700 Hz) and its first harmonic, 1400 Hz, were the most prominent frequencies at which the blade would be excited. The excitation frequency of 650 Hz was also detected, but at 75 % of the intensity of the 700 Hz nozzle bypass frequency. This suggests that the effect of the mere presence of the nozzle is greater than the frequency at which the nozzle is exciting. The effect of the blade passing through the focussed injector stream, 14 times per revolution, therefore had a greater excitation effect than the frequency at which the injector was pulsating.

The close proximity of the 700 Hz peak next to the 650 Hz excitation peak, raised the concern that the two frequencies might influence each other. The concern was that the FFT might not be an accurate representation of

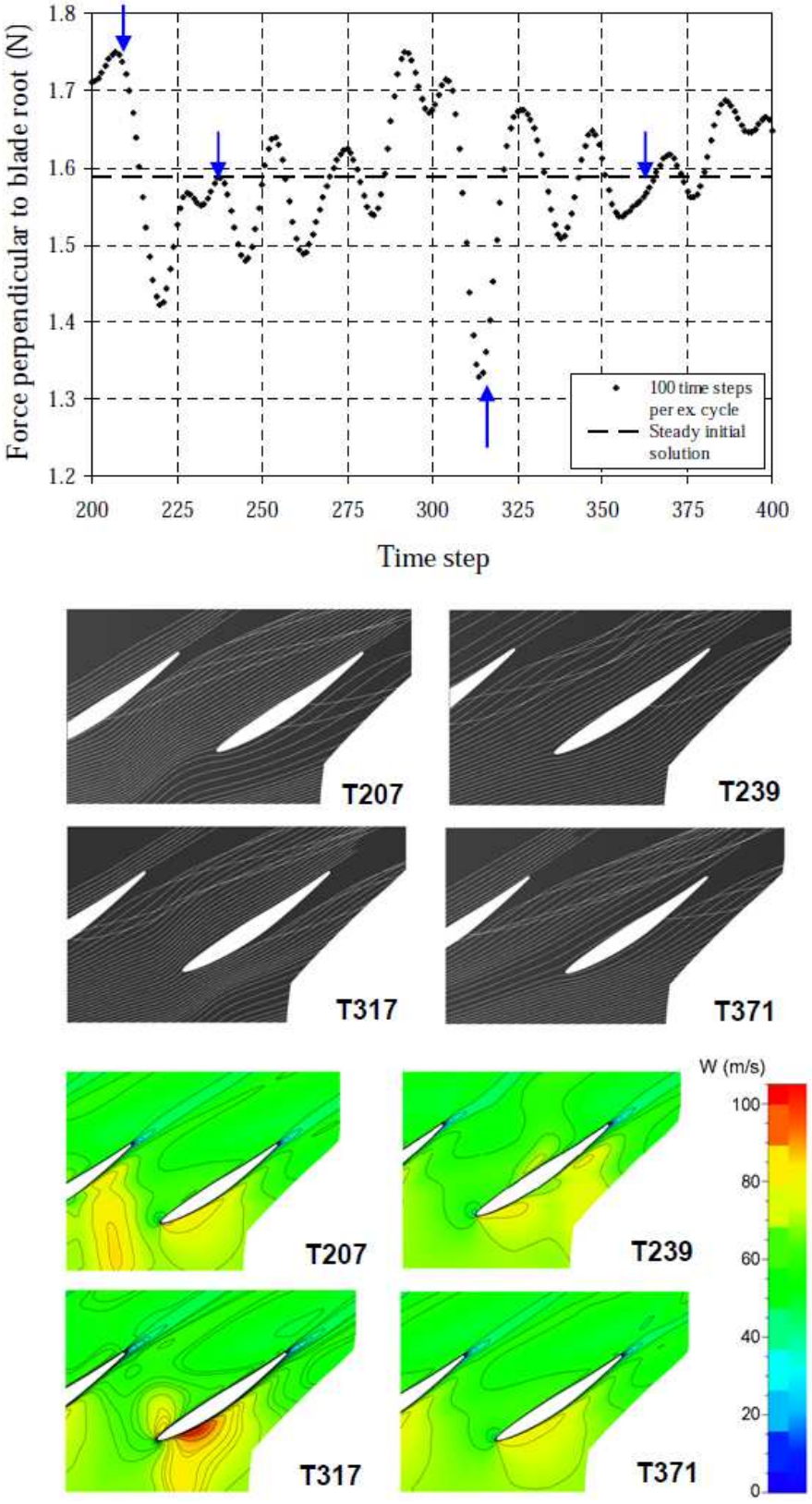

Figure 5.9: Visualisation of relative velocity and stream line contours as a result of 650 Hz axial excitation

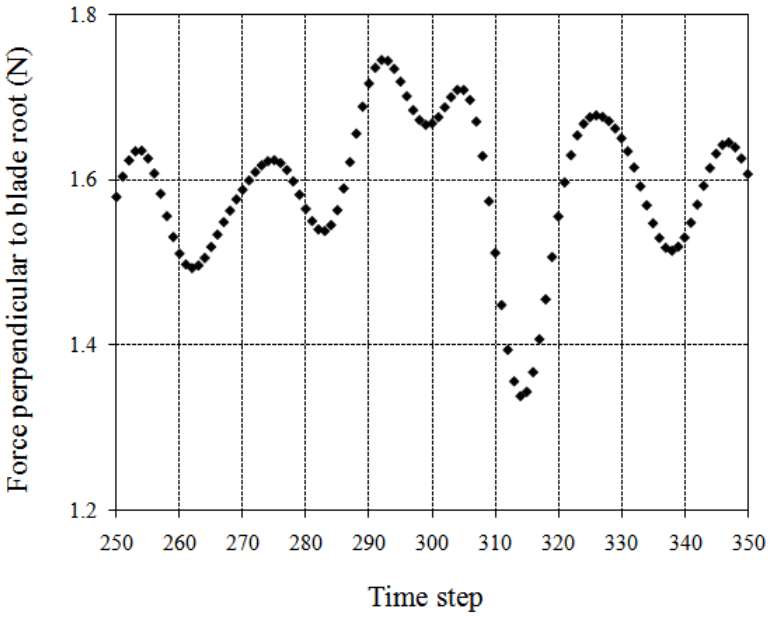

Figure 5.10: Force response time series for 100 time steps to 650 Hz axial excitation

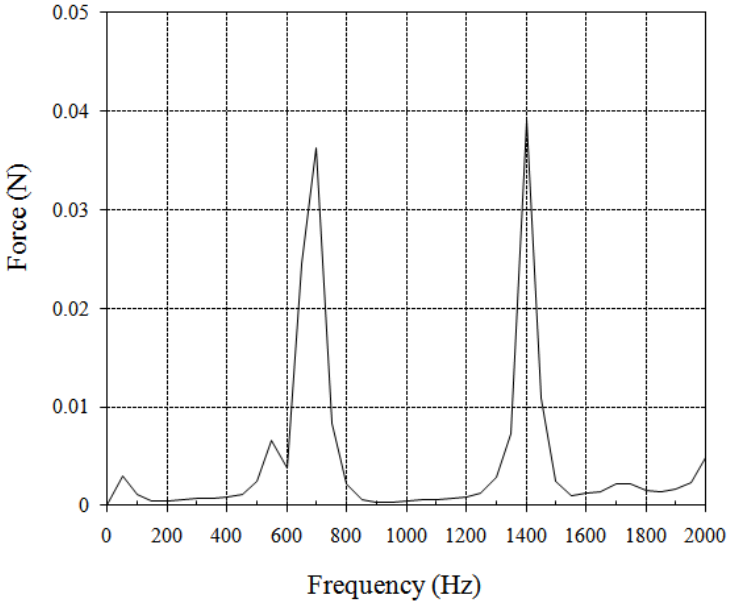

Figure 5.11: FFT of the force response time series to 650 Hz axial excitation

the excitation amplitude. It was therefore decided to investigate the effect of excitation at 1200 Hz, to ensure better distinction from the 700 Hz and 1400 Hz exciter bypass related frequencies. These simulations were all performed using both the 360 angular positions approach, as well as the minimum time step approach (see section 5.6). The 360 angular positions approach produced results that showed the expected excitation frequency more prominently. The results for the 360 angular positions approach will be discussed for the various nozzle configurations.

Figure H.2 is the result of axial excitation at 1200 Hz, expressed as the blade force variation over time. The 1200 Hz simulations were recorded for one revolution consisting of 360 time steps. An FFT of the blade force response (Figure 5.12) shows that the nozzle bypass frequency, 700 Hz, and its first harmonic, 1400 Hz, were the most prominent frequencies at which the blade was excited. The excitation frequency of 1200 Hz was also detectable, but relatively small compared to the nozzle bypass frequency. The 700 Hz nozzle bypass frequency had a peak of 0.04 N, while the 1200 Hz excitation frequency had a peak of only 0.0015 N. This suggests that for this specific frequency and injector mass flow rate setting, the effect of the excitation frequency was small (3.8 %), compared to the excitation effect of the nozzle bypass frequency.

Figure 5.12 shows that several other frequencies, which do not at first glance seem related to the exciter bypass frequency or the excitation frequency, were also very prominent. These frequencies will be discussed in detail in chapter 6.

5.8.2 Radial excitation unsteady simulation results

Figure H.3 in Appendix H, shows the blade force perpendicular to the blade root for 1200 Hz radial excitation. The simulation was performed using the 360 angular positions approach. Figure H.3 shows a mean force of 1.5 N, with peaks of up to 2 N, as the blade passed through the perturbation caused by the radial injected air stream. In the case of radial excitation, the injected air decelerated the inlet air flow because of an air curtain effect, which caused an increase in the incidence angle and a higher blade force.

An FFT of the blade force response (Figure 5.13), shows that the nozzle bypass frequency of 700 Hz and its first harmonic, 1400 Hz, were the most prominent frequencies at which the blade would be excited. The excitation frequency of 1200 Hz was also detected, but with about 37 % of the magnitude of the 700 Hz peak. The 700 Hz nozzle bypass frequency had a peak of 0.17 N, while the 1200 Hz excitation frequency had a peak of 0.064 N.

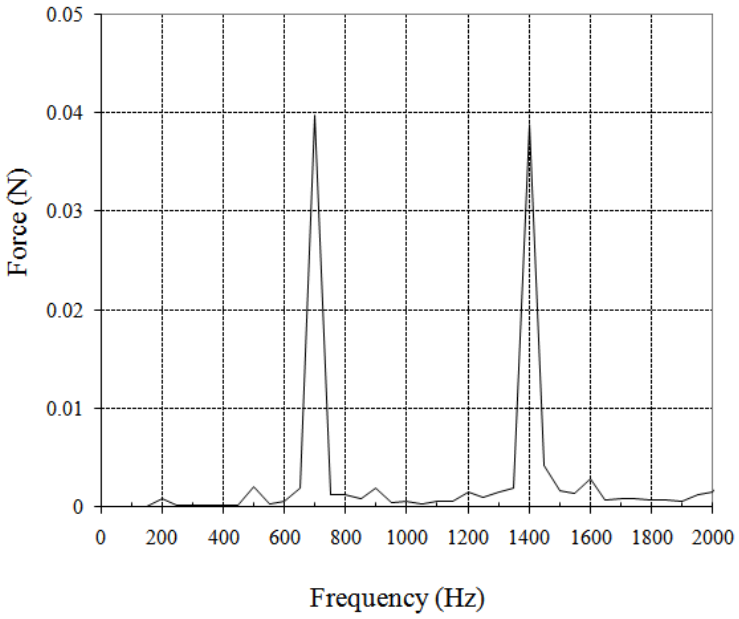

Figure 5.12: FFT of force time series for one revolution response to 1200Hz axial excitation

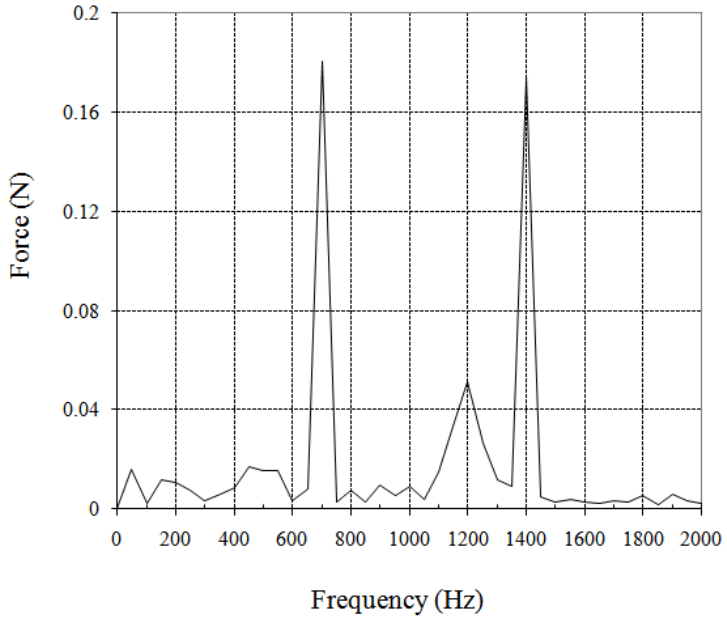

Figure 5.13: FFT of force time series for one revolution response to 1200 Hz Radial excitation

As for axial excitation, other frequencies which do not at first glance seem related to the exciter bypass frequency or the excitation frequency, were also very prominent. These frequencies will be discussed in chapter 6.

5.8.3 Production axial excitation unsteady simulation results

The production axial nozzle was also simulated at 1200 Hz excitation using the 360 angular positions approach. Figure H.4 in Appendix H shows a similar result to that found with the axial nozzle. The graph shows an average force of around 1.7 N and 14 large troughs as the blade passed through the nozzle injection stream. The troughs of low force were caused by the high velocity of the injection stream, causing a lower blade incidence angle. The lower blade incidence angle resulted in a lower force on the blade. Also, in the case of the production axial nozzle, the experimental testing revealed that the velocity perturbation was focussed on the outer third of the blade, which explains the significantly larger force troughs when compared to axial excitation.

An FFT of the blade force response (Figure 5.14), shows that the nozzle bypass frequency of 700 Hz and its first harmonic (1400 Hz) were the most prominent. The excitation frequency of 1200 Hz was also detectable, but extremely small (2.7 %) compared to the nozzle bypass frequency. The 700 Hz nozzle bypass frequency had a peak of 0.26 N, while the 1200 Hz excitation frequency had a peak of only 0.007 N.

The experimental results were assessed again and it was noted that the radial excitation velocity perturbation had a mean value that was relatively close to the mean velocity profile. In the case of the axial excitation nozzles, the velocity perturbations had mean values that were significantly larger than the mean velocity profile.

A more ideal way of excitation with the production axial nozzle was then attempted in an effort to increase the relative magnitude of the excitation frequency response. The nozzle inlet velocity variation was altered in an effort to decrease the excitation perturbation mean value to the point where the perturbation minimum value was equal to the mean velocity profile.

An FFT of the ideal blade force response (Figure 5.15) shows that the exciter nozzle bypass frequency of 700 Hz and its harmonic (1400 Hz), were still very prominent. The excitation frequency was also detectable at about 15 % of the magnitude of the nozzle bypass frequency. This test showed that reducing the mean perturbation value increased the amplitude of the excitation

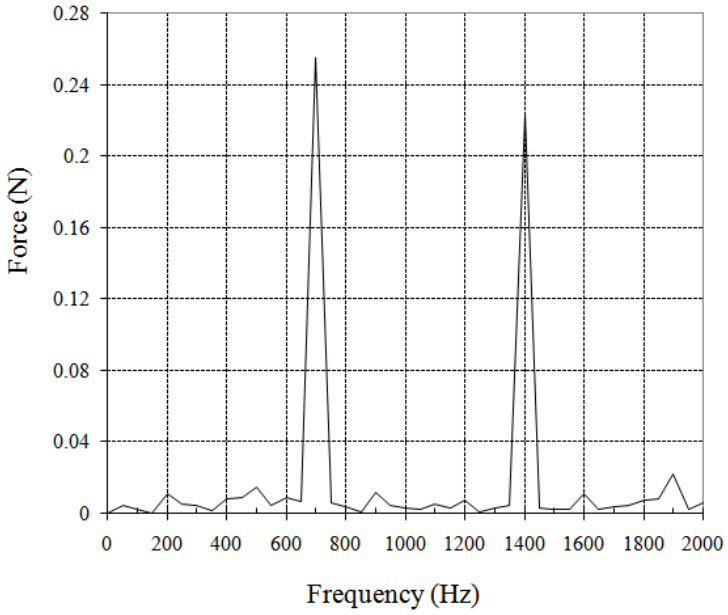

Figure 5.14: FFT of force time series for one revolution response to 1200 Hz Production Axial excitation

frequency relative to the nozzle bypass frequency. The 700 Hz nozzle bypass frequency had a peak of 0.054 N, while the 1200 Hz excitation frequency had a peak of only 0.0084 N.

5.9 Summary of unsteady simulation results

The results from the unsteady simulations showed that the radial nozzle provided the highest level of excitation. Both the axial and production axial nozzles produced detectable, but relatively small blade force responses at the excitation frequency. For the same exciter mass flow setting, the radial nozzle produced an excitation peak of approximately 10 times the magnitude of the other nozzles. For all three types of nozzles however, the nozzle bypass frequency and its first harmonic were the most prominent frequencies present. Compared to its nozzle bypass and first harmonic frequency, the radial nozzle produced the most prominent excitation frequency.

A comparison of the three excitation techniques revealed that the radial excitation velocity perturbation had a mean value that was relatively close to the mean velocity profile. In the case of the axial excitation, the velocity perturbations had mean values that were significantly larger than the mean velocity profile. The ideal production axial excitation case aimed to decrease the excitation perturbation mean value to the point where the perturbation

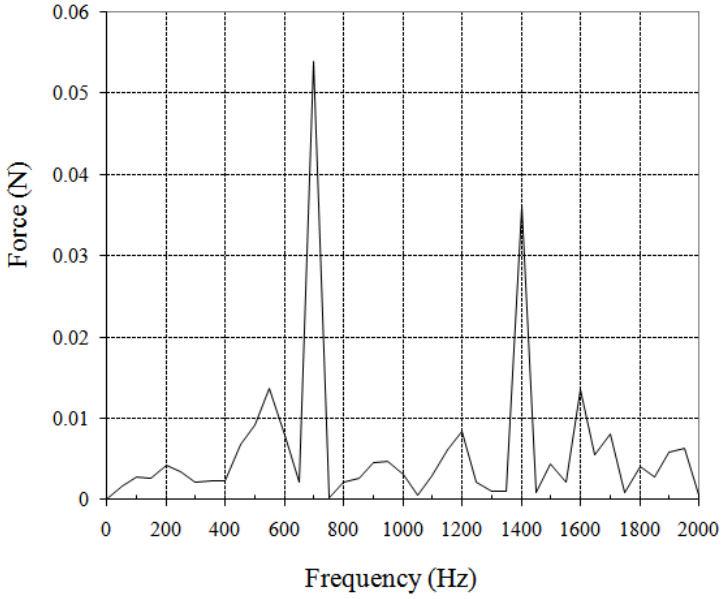

Figure 5.15: FFT of force time series for half a revolution response to and ideal case of 1200 Hz Production Axial excitation

minimum value was equal to the mean velocity profile. The results of this simulation showed that the nozzle bypass frequency and its first harmonic were still very prominent, but that the excitation frequency became more prominent when compared to the original axial and production axial nozzle results.

A further investigation into the presence of the nozzle bypass frequency, the relative magnitude of the excitation frequency response and the presence of other seemingly unrelated frequencies, are described in Chapter 6.

Chapter 6

Computational modelling of the blade force response

6.1 Model set-up and results

In order to gain a more in-depth understanding of the simulation findings discussed in chapter 5, a number of mathematical blade force models were developed. FFTs were performed on these models and then compared to the simulation results.

A simplified replica of blade force response was created by defining a sine wave of 12 Hz with a negative offset (representing the excitation frequency) and multiplying it with a 7 Hz rectangular wave with an upper value of one and a lower value of 0 (representing the 14 nozzle air streams). An offset was then added to the resulting wave so that it formed a wave with a high mean value and sections of the sine profile at the troughs. The final result was a wave similar to the 1200 Hz production axial simulation results.

Figure 6.1 shows the various waves that made up the final wave and also the FFTs of all the waves, including the final resulting wave. The FFT of the final result shows that the bypass frequency of 7 Hz and its harmonics were the most dominant, followed by the 12 Hz excitation frequency and several other seemingly random frequency peaks (2 Hz, 5 Hz, 16 Hz and 19 Hz). Comparing this FFT with the results from the unsteady simulations show, that the random frequencies from the simulation results correspond with those detected on the resulting wave FFT in figure 6.1.

In the Fourier Transform field of study, the frequency-convolution theorem states that, when a function is given by the product of two basic functions, the FFT of that function will be given by the convolution of the FFTs of the two basic functions (Brigham, 1988). In the above mentioned model, the resulting

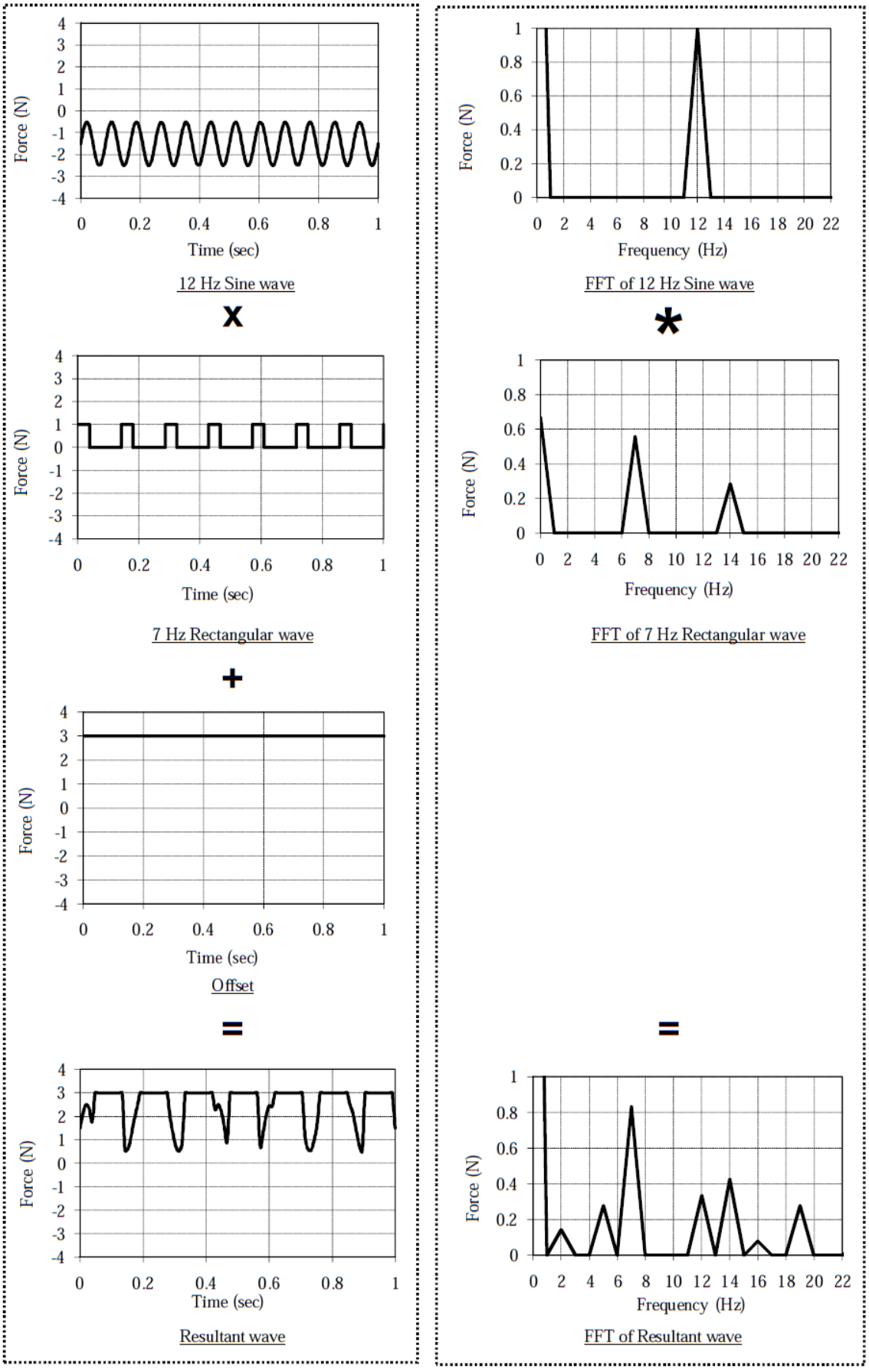

Figure 6.1: Mathematical comparison of production axial excitation (Model of a sine wave with an offset and the resultant wave with an offset)

wave is the product of the 12 Hz and the 7 Hz wave. Therefore, when applying the convolution theorem to the model, the resulting wave FFT is given by the convolution of the FFTs of the 7 Hz and the 12 Hz waves. The presence of various frequencies, other than the blade bypass and excitation frequencies, is therefore the result of convolution and not due to other effects or random anomalies in the simulation.

The theory behind convolution will now be discussed in brief. The function $y(t)$ is given as the convolution of two functions $x(t)$ and $h(t)$ by the following integral (Brigham, 1988):

$$y(t) = \int_{-\infty}^{\infty} x(\tau)h(t-\tau)\,d\tau = x(t) * h(t) \tag{6.1.1}$$

The time-convolution theorem is then given by:

$$x(t) * h(t) \supset X(f)H(f) \tag{6.1.2}$$

To get this result, the Fourier transform of both sides of equation 6.1.1 is formed:

$$\int_{-\infty}^{\infty} y(t)e^{-j2\pi ft}\,dt = \int_{-\infty}^{\infty}\Big[\int_{-\infty}^{\infty} x(\tau)h(t-\tau)\,d\tau\Big]e^{-j2\pi ft}\,dt \tag{6.1.3}$$

which is equivalent to:

$$Y(f) = \int_{-\infty}^{\infty} x(\tau)\Big[\int_{-\infty}^{\infty} h(t-\tau)e^{-j2\pi ft}\,dt\Big]\,d\tau \tag{6.1.4}$$

By using $\sigma = t - \tau$, the term in the brackets becomes:

$$\int_{-\infty}^{\infty} h(\sigma)e^{-j2\pi f(\sigma+\tau)}\,d\sigma = e^{-j2\pi f\tau}\int_{-\infty}^{\infty} h(\sigma)e^{-j2\pi f\sigma}\,d\sigma = e^{-j2\pi f\tau}H(f) \tag{6.1.5}$$

Equation 6.1.4 can then be rewritten as:

$$Y(f) = \int_{-\infty}^{\infty} x(\tau)e^{-j2\pi f\tau}H(f)\,d\tau = H(f)X(f) \tag{6.1.6}$$

Similarly it can be proven that:

$$x(t)h(t) \supset X(f) * H(f) \tag{6.1.7}$$

Figure 6.2 shows a graphical example of the frequency-convolution theorem.

When the frequency-convolution theorem is applied to figure 6.1, it must be kept in mind that the respective FFT graphs only show the positive frequency component. The negative component, which is a mirror image of the positive

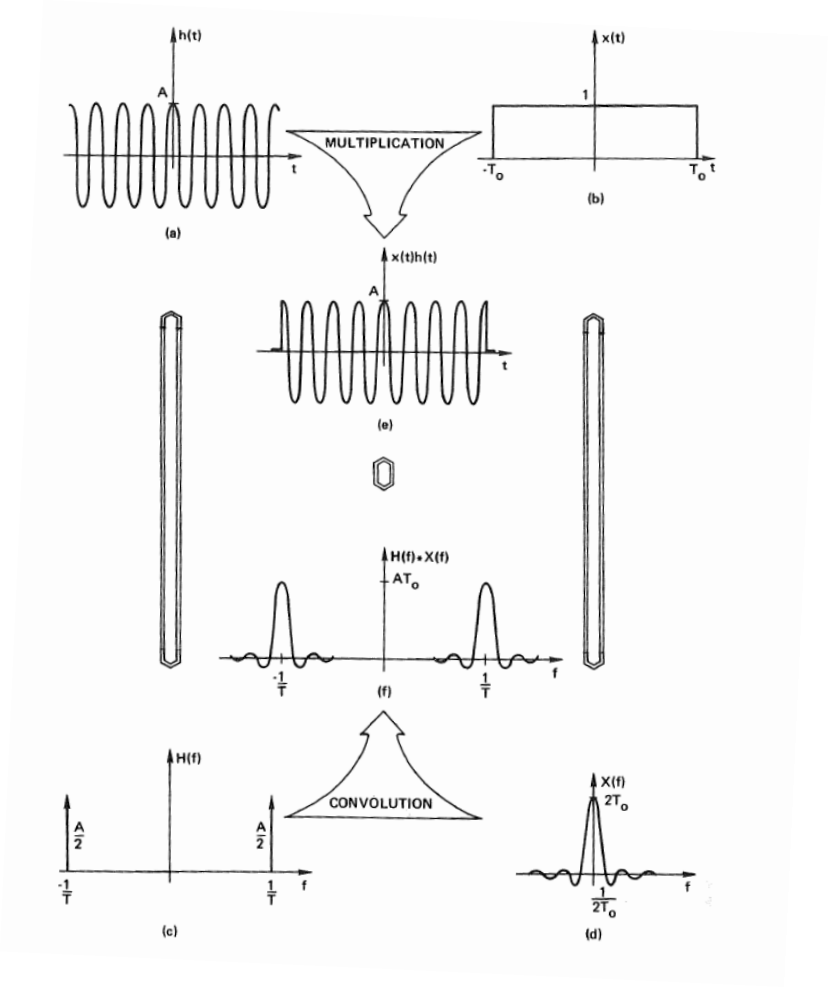

Figure 6.2: Graphical example of the frequency-convolution theorem (Brigham, 1988)

component around the y-axis, is not displayed in this graph. In more practical terms, the convolution of the FFT of the 12 Hz sine wave with the FFT of the 7 Hz rectangular wave, will result in peaks at the following frequencies (p):

Resulting from the -12 Hz peak on the FFT of the sine wave (not shown):

$$p = 7k - 12 \tag{6.1.8}$$

Resulting from the 12 Hz peak on the FFT of the sine wave:

$$p = 7k + 12 \tag{6.1.9}$$

Resulting from the 0 Hz peak on the FFT of the sine wave (mean offset value of the sine wave):

$$p = 7k \tag{6.1.10}$$

where k is the number of the peak on the FFT of the 7 Hz rectangular wave.

For example, if the mean offset is given by $k = 0$, the primary frequency peak of 7 Hz is given by $k = 1$ and the harmonics of 7 Hz are given by k-values larger than 1. If there is no offset of the sine wave, equation 6.1.10 will not produce any peaks. Therefore, if there is no mean offset of the 12 Hz sine wave, the 7 Hz rectangular wave and its harmonics will not be present.

The model in figure 6.1 was then simplified and progressively altered to establish how the presence of nozzle bypass frequency and the other resulting frequencies could be minimised.

In the first alteration, no offset was added to the 12 Hz sine wave, so that it had a mean value of 0. It was then multiplied with a 7 Hz rectangular wave, with an upper value of one and a lower value of 0 (representing the 14 nozzle air streams). No offset was added, so that the resulting wave had a mean value of zero, with sections of the sine wave both positive and negative. The FFT of the resultant wave in figure I.1 shows that the 12 Hz excitation frequency and the other secondary frequencies (2 Hz, 5 Hz, 16 Hz and 19 Hz) were present, but the 7 Hz bypass frequency and its 14 Hz first harmonic were not present.

The next alteration was to create a resulting wave identical to the first alteration. An offset was then added to the resulting wave, so that it had a mean value of 3, with sections of the sine wave above and below the mean value. The FFT of the resultant wave in figure I.2 shows that the 12 Hz excitation frequency and the other secondary frequencies (2 Hz, 5 Hz, 16 Hz and 19 Hz) were present and again the 7 Hz and 14 Hz frequencies were not present.

The third and final alteration was a sine wave of 12 Hz, with an offset of -1.5, multiplied with a 7 Hz rectangular wave as described in the previous cases. In this case, no offset was added to the resulting wave so that it had a mean value of approximately 0, with the sections of the sine wave varying at a mean value of -1.5. The FFT of the resultant wave in figure I.3 shows that the 12 Hz excitation frequency and the other secondary frequencies (2 Hz, 5 Hz, 16 Hz and 19 Hz) were present, but in this case, the 7 Hz and 14 Hz frequencies were more prominent than the excitation frequency.

6.2 Conclusions of computational modelling

It can therefore be concluded that it would not be possible to completely eliminate the secondary frequencies (2 Hz, 5 Hz, 16 Hz and 19 Hz in this model) from the frequency response, by using a finite number of exciters. These frequencies are the result of the convolution of the FFTs of the excitation wave and the rectangular wave.

It can also be concluded that it would be possible to eliminate the exciter nozzle bypass frequency. This can be achieved by utilising an exciter nozzle or any form of technology that will cause a velocity perturbation, with a mean value equal to the mean value of the free stream (not excited) velocity profile. The velocity perturbation must therefore cycle above and below the mean velocity of the free stream.

Chapter 7

Conclusions

The objective of this project was to evaluate the effectiveness a gas injection system as a means of exciting vibration in the rotor blades of an axial compressor. The first part of the project consisted of experimental work to characterise three types of gas injection nozzles (axial, radial and production axial) and to verify a vibration measuring system. The second part of the project consisted of CFD simulations, performed to evaluate the effectiveness of the three injector nozzles as a means of exciting rotor blade vibration.

7.1 Experimental characterisation of injection nozzles

The characterisation of the velocity profile downstream of the radial nozzle showed that, at a constant frequency, an increase in the mass flow rate caused the area of the highest velocity perturbation to be closer to the blade root. Therefore, because of the higher bending moment associated with a force closer to the blade tip, it appeared that a lower radial injector mass flow rate would result in a higher level of blade excitation. Also, at a fixed injector mass flow rate, an increase in frequency resulted in a decrease in the amplitude of the velocity perturbations.

In the case of the axial nozzle, the characterization of the velocity profile downstream of the axial nozzle showed that, for all settings, the maximum velocity perturbation occurred at the 0.208 m radial position (2 mm away from the blade tip). The test results also showed that, for axial excitation, an increase in injector mass flow rate would increase the level of blade excitation and an increase in frequency would decrease the blade excitation level.

Tests to characterise the production axial nozzle revealed that this nozzle was not as successful as the first axial type at producing velocity perturba-

tions that are focussed on the blade tip. Results showed that the maximum velocity perturbation occurred at the 0.19 m radial position, one third of the blade away from the blade tip. The perturbation effect was notable on most of the upper third part of the blade. As with the axial nozzle, results showed that an increase in injector mass flow rate would increase the level of blade excitation and an increase in frequency would decrease the blade excitation level.

7.2 Experimental tests to verify a blade vibration measuring system

The experimental tests to verify the blade vibration measuring system showed that the strain gauges performed satisfactorily as sensors measuring blade vibration. A simple impact test confirmed that the blade natural frequency (the first flapping mode) was accurately measured. The oscillatory blade root stresses were measured while the compressor was operating at various mass flow rate settings, at a speed of 3000 RPM. The test results correlated with the expected behaviour of the blades, as well as with results obtained from previous testing. These results confirmed that the strain gauge and slip ring system worked effectively as a blade vibration and deflection measurement system. Preliminary experimental testing with a single axial injector, with the blade stationary, showed that expected frequencies were detected by the strain gauge measuring system. The results suggested that the concept of blade excitation by means of gas injection would provide sufficient excitation.

7.3 Unsteady simulation of the gas injection vibration exciters

The simulation work started with the evaluation of several aspects of the grid and solver settings. The simulation model was validated by correlating the pressure ratio and mass flow rate relations with measured experimental data. This model was then used as the baseline from which the unsteady simulation models were constructed.

The unsteady simulation models consisted of 3 first stage rotor blades and one exciter. The total number of blades in the stage was decreased from 43 to 42 and the number of exciters from 15 to 14. This was done in order to generate 14 periodic repeating sections, consisting of 3 blades and one exciter. The boundary conditions of the steady inlet velocity profile, the varying nozzle velocity profiles and the outlet pressure were based on measured experimental

data. Unsteady simulations of 1200 Hz excitation were then performed to correlate the axial velocity profiles 10 mm in front of the rotor blades, with the equivalent experimental measurements. The nozzle velocity profiles were iteratively altered until satisfactory velocity profiles were achieved. With a good velocity profile correlation between the experimental testing and simulation models, the blade force response could be analysed.

The results for radial excitation showed that the exciter nozzle bypass frequency of 700 Hz and its first harmonic, 1400 Hz, were the most prominent frequencies at which the blade would be excited. The excitation frequency of 1200 Hz was also detected, but only at about 37% of the magnitude of the 700 Hz peak.

For both the axial and production axial nozzles, the results also showed that the exciter nozzle bypass frequency of 700 Hz and its first harmonic, 1400 Hz, were the most prominent frequencies at which the blade would be excited. For these nozzles, the excitation frequency of 1200 Hz was detectable, but at a mere 3% of the magnitude of the 700 Hz peak. A more ideal case of the production axial nozzle was simulated in an attempt to reduce the effect of the nozzle bypass frequency. The results showed that the exciter nozzle bypass frequency of 700 Hz and its first harmonic remained the most prominent frequencies detected, but that the excitation frequency of 1200 Hz could be increased to 15% of the magnitude of the 700 Hz peak. A comparison of the excitation frequency responses of the various nozzles showed that the radial nozzle produced an excitation peak of approximately 10 times the magnitude of that of the other nozzles, at the same exciter mass flow setting. The simulation results led to the conclusion that the radial nozzle would provide the most effective excitation of the rotor blades of the Rofanco compressor.

A number of other smaller frequency peaks (referred to as secondary frequencies) were also clearly detectable. While they appeared to be at the same position in all the nozzle test results, they were not at first glance related to the exciter bypass frequency or the excitation frequency. The presence of these frequencies and the nozzle bypass frequencies were explained by computational modelling of the blade force response, explained in section 7.4.

7.4 Computational modelling of blade force response

The computational modelling showed that the nozzle bypass frequencies and the secondary frequencies were present as the result of the convolution of the

FFT of the excitation wave and the FFT of a rectangular wave form. The rectangular wave represented the response of the blade as it passed through the localised air flow disturbances, caused by the injectors.

Computational modelling showed that it would be possible to eliminate the exciter nozzle bypass frequency. This could be achieved by utilising an exciter nozzle or any form of technology that would cause a velocity perturbation with a mean value equal to the mean value of the free stream (not excited air stream) velocity profile. In such a case, the magnitude of the velocity disturbance would cycle above and below the mean value of the free stream.

Furthermore, based on the computational modelling findings, it was concluded that it would not be possible to eliminate the secondary frequencies from the frequency response, when using a finite number of exciters.

7.5 Final conclusion

With the experimental testing it was possible to characterise three types of gas injection nozzles. These results formed the basis of the boundary conditions of unsteady CFD simulations that were performed to investigate the effectiveness of a 15 injector exciter system. Based on the unsteady simulation results, it was concluded that it would be possible to excite the desired frequency and that excitation by means of the radial injection nozzle would provide the most effective excitation on the Rofanco compressor. The unsteady simulation results however, also led to the conclusion that the nozzle bypass frequency would provide more excitation than the excitation frequency itself, in all cases. The nozzle bypass frequency amplitude can, to a certain extent, be controlled by varying the compressor speed or by changing the number of exciters, but it remains a concern that the nozzle bypass frequency would cause excitation at undesirable frequencies.

Computational modelling of the blade force response showed that it would be possible, in theory, to eliminate the exciter nozzle bypass frequency by setting the exciter air supply so that the mean excitation velocity is equal to the mean velocity of flow through the compressor. This would however pose the limitation that the exciter air supply rate will then be used to minimise the nozzle bypass frequency and would therefore not be adjustable to vary the intensity of excitation. Furthermore, the computational modelling showed that lower intensity secondary frequencies were present as the result of using a finite number of exciters. These frequencies cannot be eliminated and will have to be considered when using this system for blade excitation at specific frequencies.

Finally, it can be stated that the 15 exciter system would be effective in exciting blade vibration at any desirable frequency up to 1200 Hz, but that it has limitations in the form of other, possibly undesirable frequencies that would have to be managed during experimental testing.

Appendices

Appendix A

Experimental equipment set-up: detail information

A.1 Blade strain gauge attachment position

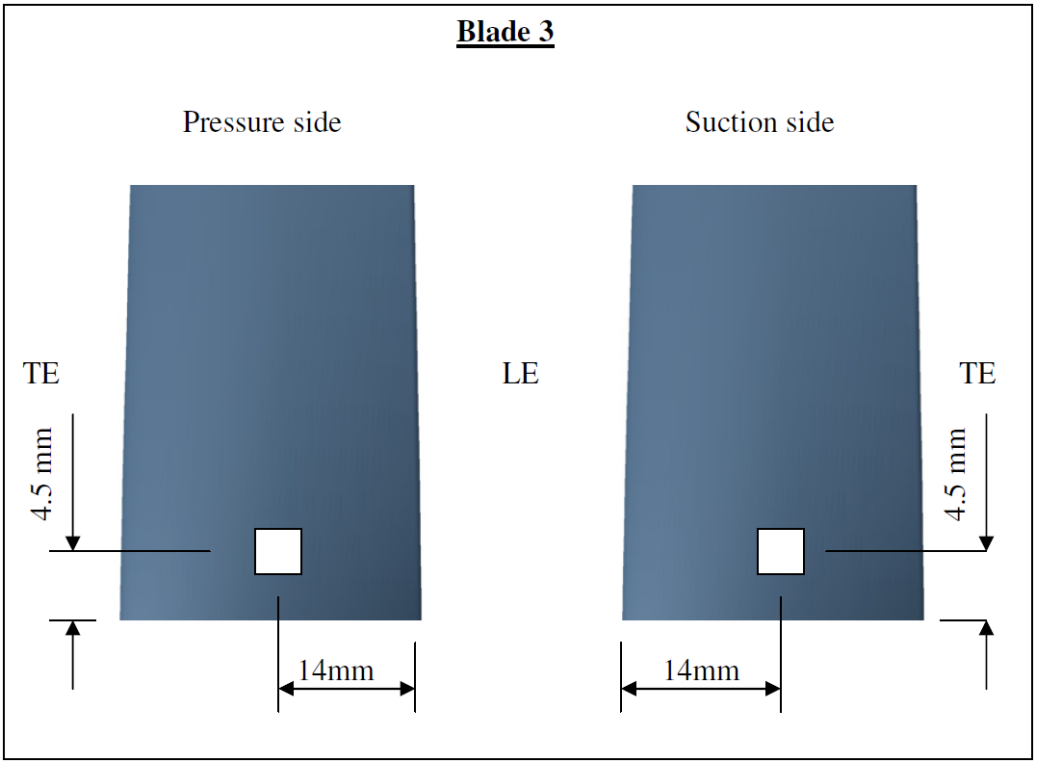

Figure A.1: Strain gauge half bridge attachment positions on blade 3

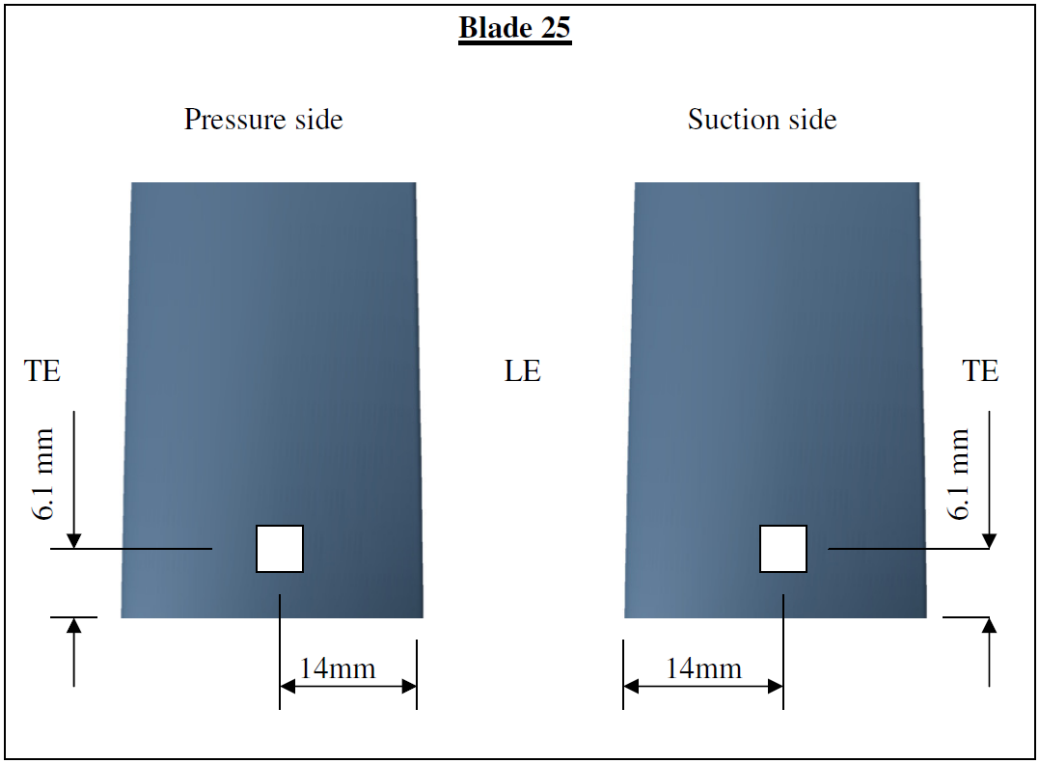

Figure A.2: Strain gauge half bridge attachment positions on blade 25

A.2 Strain gauge technical specifications

- Description: Vishay Micro measurements SR-4 General purpose Strain Gauges
- Grid resistance (Ω): 120.0 ± 0.3%
- TC of Gage factor, %/100°C: +1.2 ± 0.2
- Gage factor @ 24°C: 2.035 ± 0.53%
- Transverse sensitivity: +1.2 ± 0.2

A.3 Exciter nozzles and hot wire sensor set-up

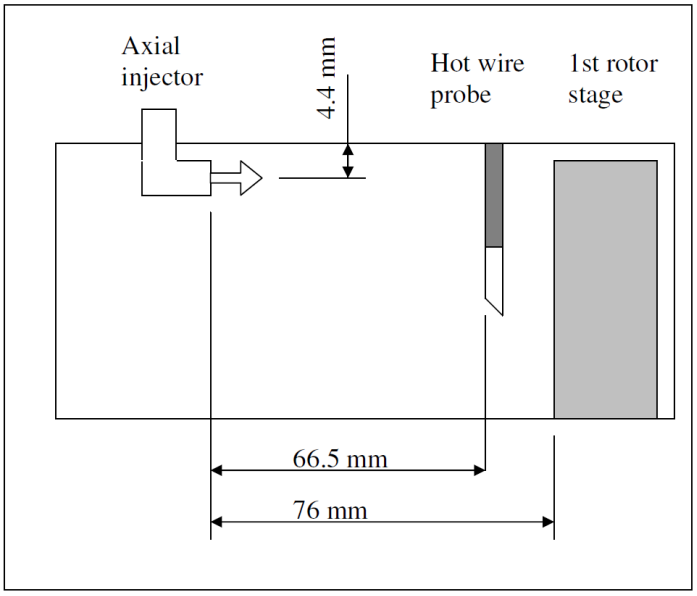

Figure A.3: Position of the hot wire sensor and first stage rotor blade relative to the axial injector nozzle

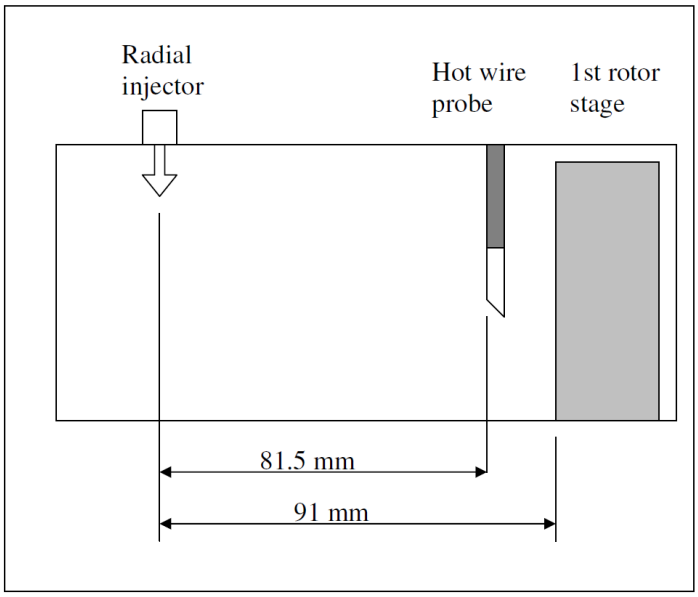

Figure A.4: Position of the hot wire sensor and first stage rotor blade relative to the radial injector nozzle

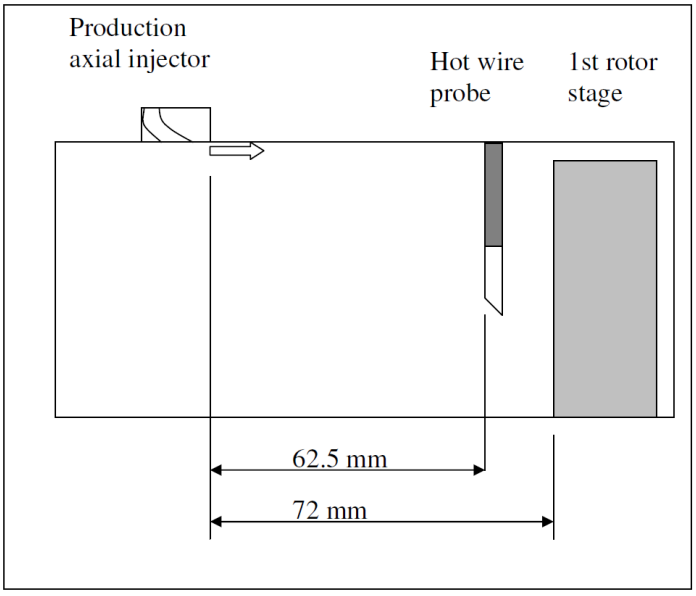

Figure A.5: Position of the hot wire sensor and first stage rotor blade relative to the production axial injector nozzle

A.4 Production axial injector flow direction and temperature measurement set-up

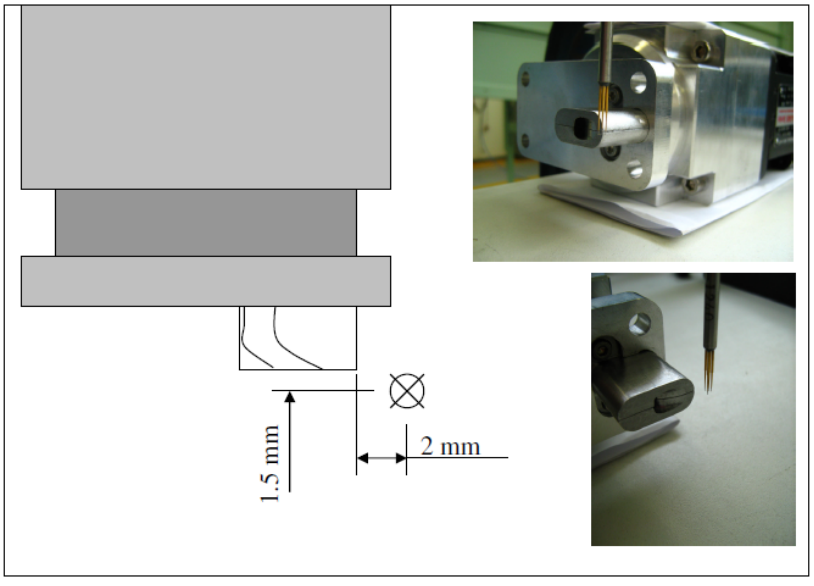

Figure A.6: Position of the hot wire sensor and temperature probe for the production axial injector flow direction and temperature measurements

Appendix B

Results: Axial velocity perturbation graphs

B.1 Axial excitation 60 Hz

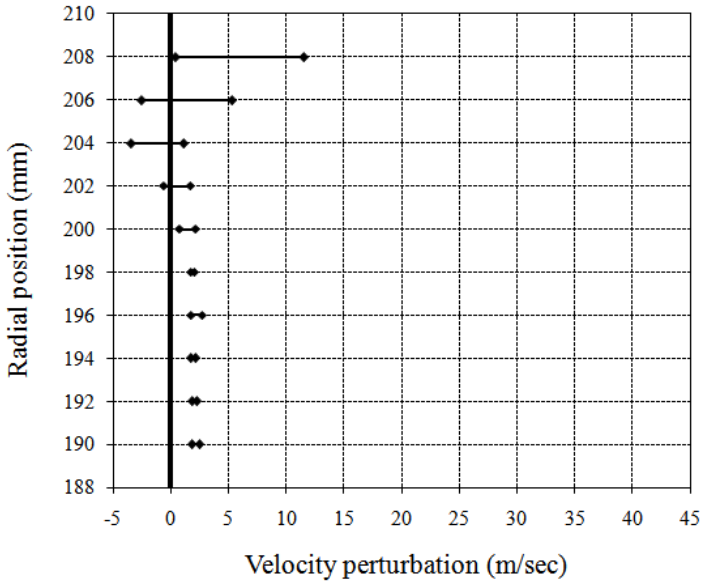

Figure B.1: Axial velocity perturbation relative to mean velocity for various radial positions with 60 Hz axial excitation with a mass flow rate of 13.8 x 10^{-3} kg/sec

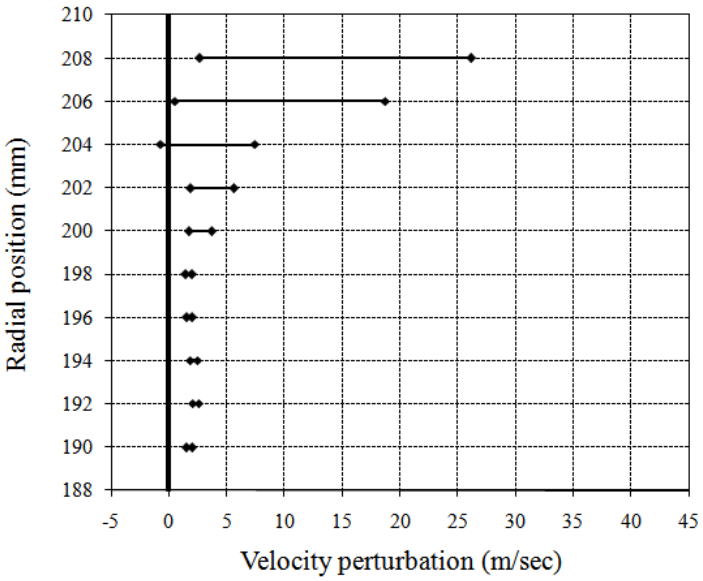

Figure B.2: Axial velocity perturbation relative to mean velocity for various radial positions with 60 Hz axial excitation with a mass flow rate of 19.9 x 10^{-3} kg/sec

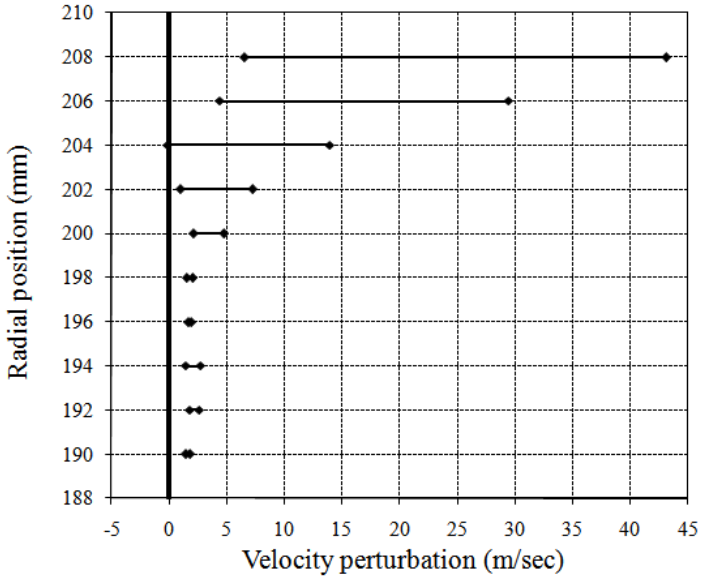

Figure B.3: Axial velocity perturbation relative to mean velocity for various radial positions with 60 Hz axial excitation with a mass flow rate of 23.8 x 10^{-3} kg/sec

B.2 Axial excitation 650 Hz

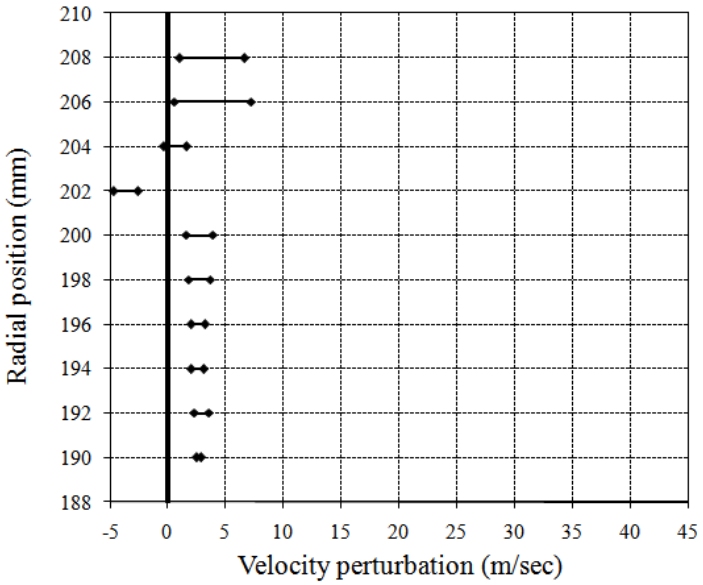

Figure B.4: Axial velocity perturbation relative to mean velocity for various radial positions with 650 Hz axial excitation with a mass flow rate of 13.8 x 10^{-3} kg/sec

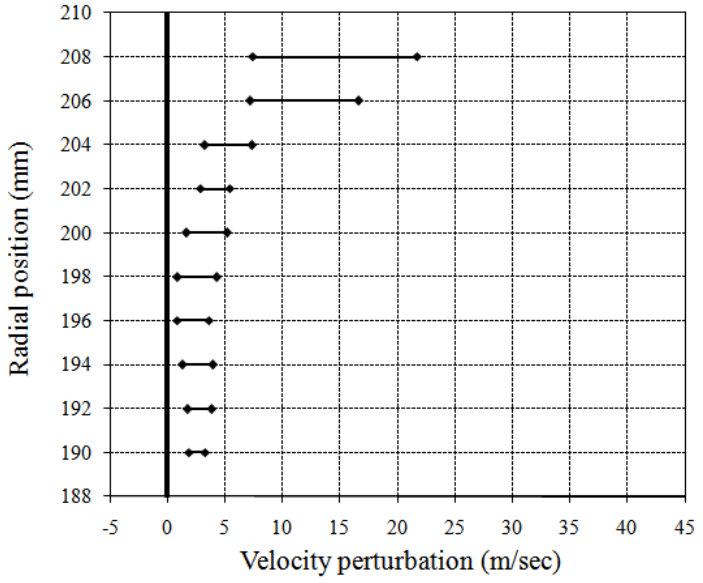

Figure B.5: Axial velocity perturbation relative to mean velocity for various radial positions with 650 Hz axial excitation with a mass flow rate of 19.9 x 10^{-3} kg/sec

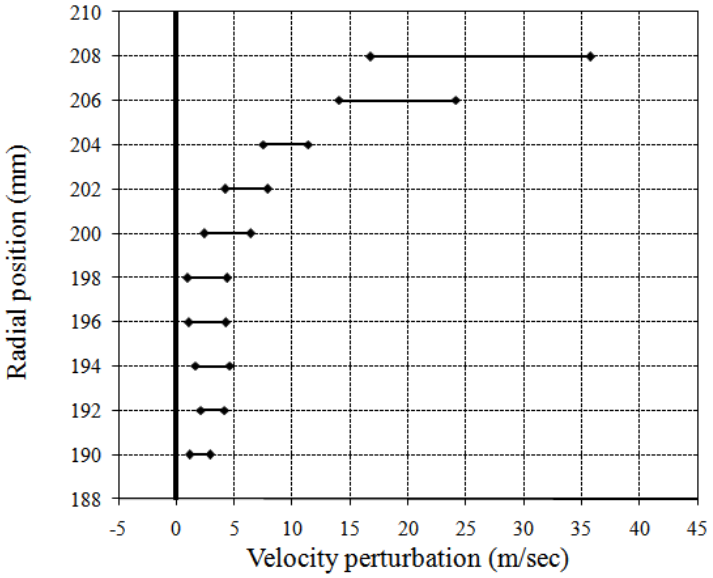

Figure B.6: Axial velocity perturbation relative to mean velocity for various radial positions with 650 Hz axial excitation with a mass flow rate of 23.8 x 10^{-3} kg/sec

B.3 Axial excitation 1200 Hz

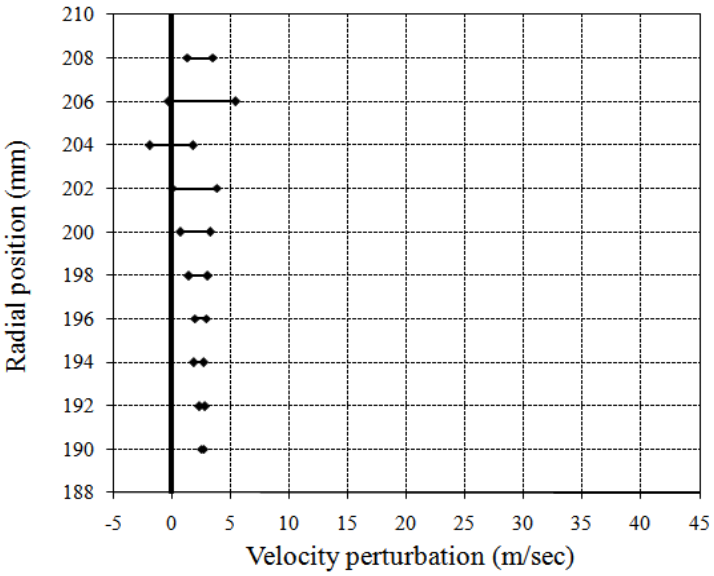

Figure B.7: Axial velocity perturbation relative to mean velocity for various radial positions with 1200 Hz axial excitation with a mass flow rate of 13.8 x 10^{-3} kg/sec

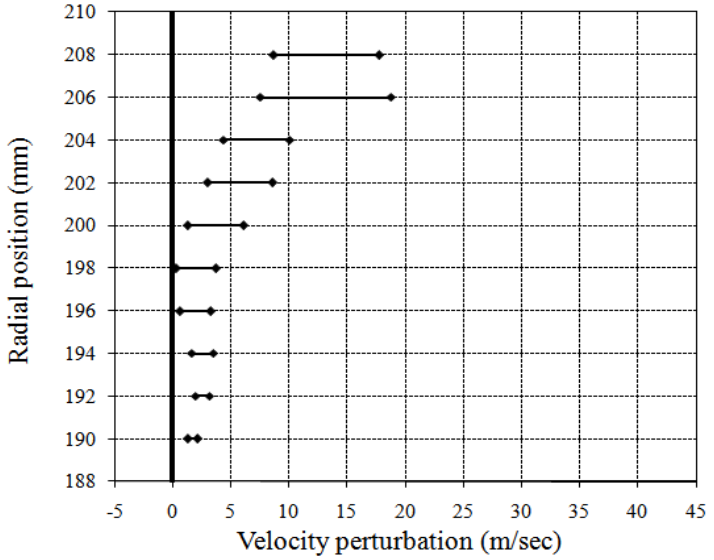

Figure B.8: Axial velocity perturbation relative to mean velocity for various radial positions with 1200 Hz axial excitation with a mass flow rate of 19.9 x 10^{-3} kg/sec

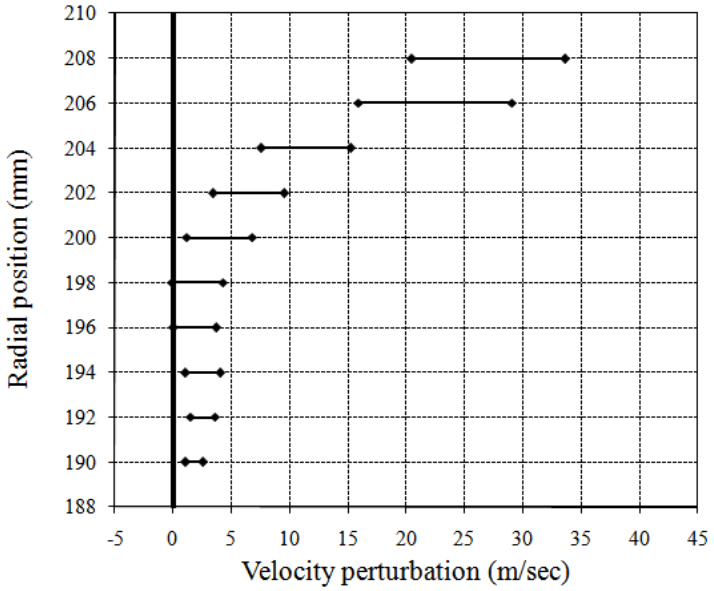

Figure B.9: Axial velocity perturbation relative to mean velocity for various radial positions with 1200 Hz axial excitation with a mass flow rate of 23.8 x 10^{-3} kg/sec

Appendix C

Results: Radial velocity perturbation graphs

C.1 Radial excitation 60 Hz

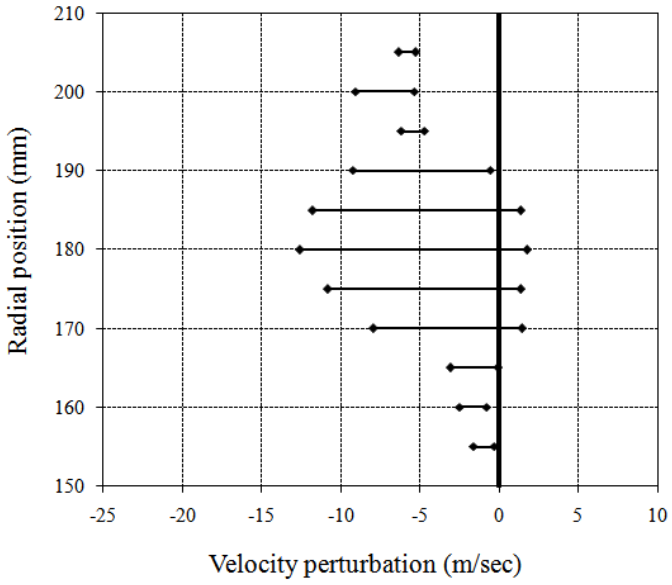

Figure C.1: Radial velocity perturbation relative to mean velocity for various radial positions with 60 Hz radial excitation with a mass flow rate of 13.8 x 10^{-3} kg/sec

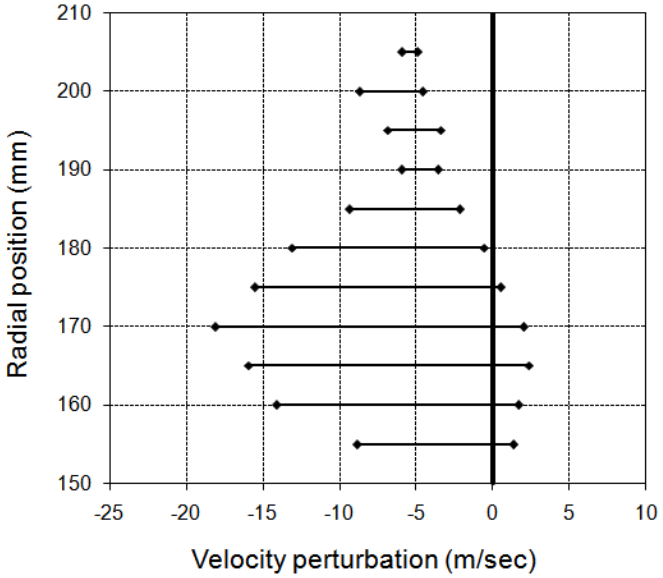

Figure C.2: Radial velocity perturbation relative to mean velocity for various radial positions with 60 Hz radial excitation with a mass flow rate of 19.9 x 10^{-3} kg/sec

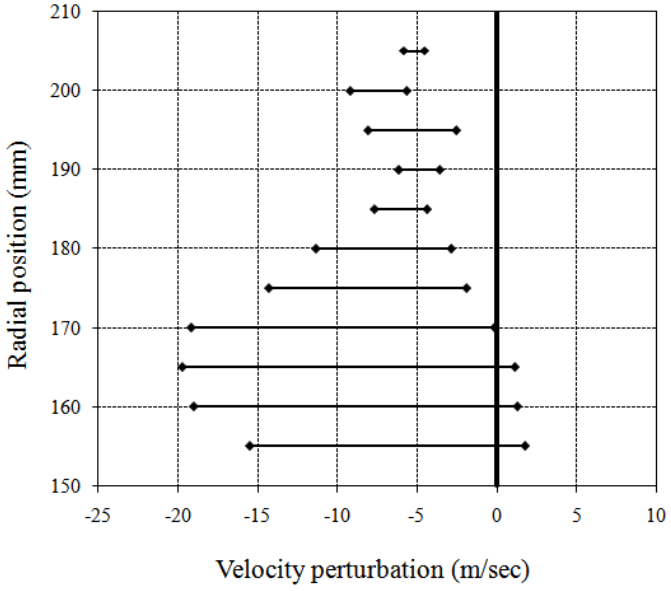

Figure C.3: Radial velocity perturbation relative to mean velocity for various radial positions with 60 Hz radial excitation with a mass flow rate of 23.8 x 10^{-3} kg/sec

C.2 Radial excitation 650 Hz

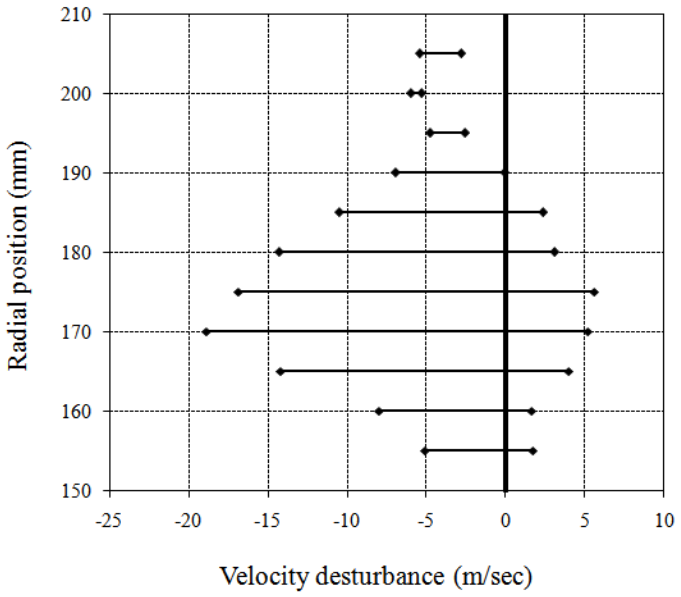

Figure C.4: Radial velocity perturbation relative to mean velocity for various radial positions with 650 Hz radial excitation with a mass flow rate of 13.8 x 10^{-3} kg/sec

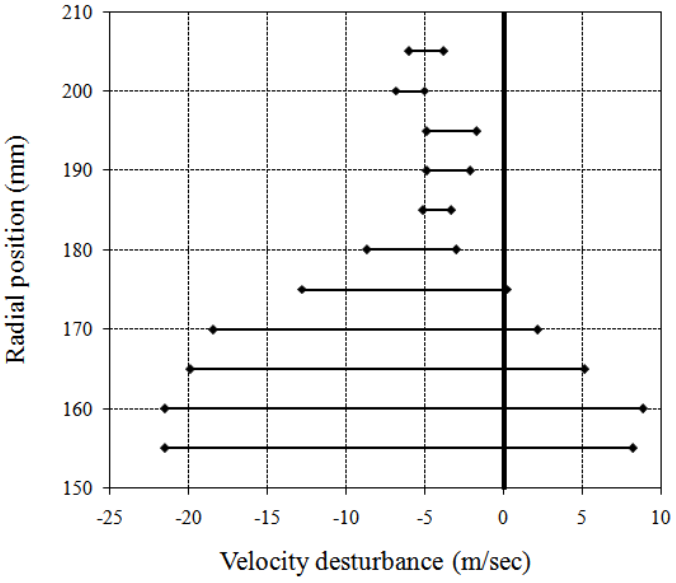

Figure C.5: Radial velocity perturbation relative to mean velocity for various radial positions with 650 Hz radial excitation with a mass flow rate of 19.9 x 10^{-3} kg/sec

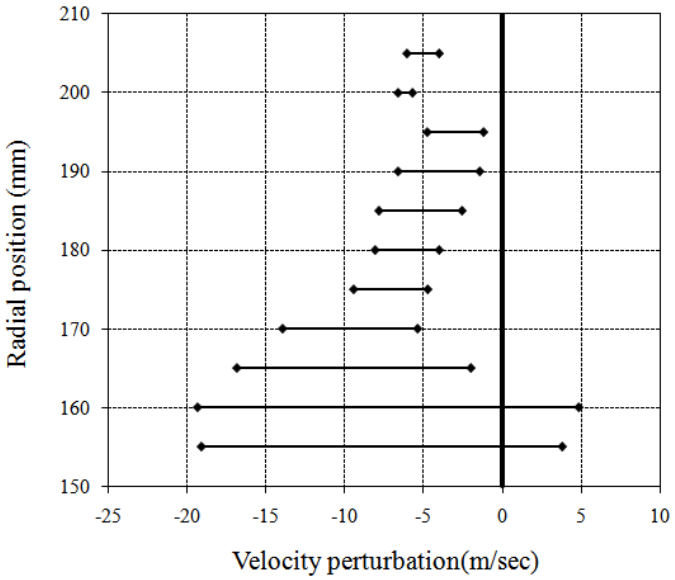

Figure C.6: Radial velocity perturbation relative to mean velocity for various radial positions with 650 Hz radial excitation with a mass flow rate of 23.8 x 10^{-3} kg/sec

C.3 Radial excitation 1200 Hz

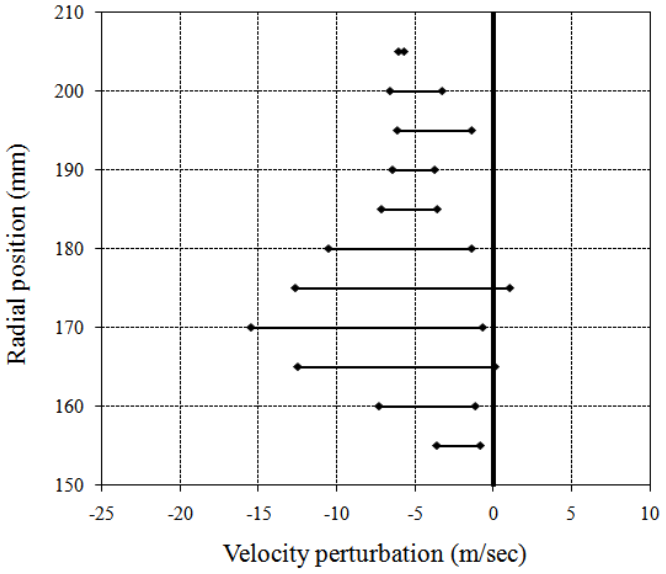

Figure C.7: Radial velocity perturbation relative to mean velocity for various radial positions with 1200 Hz radial excitation with a mass flow rate of 13.8 x 10^{-3} kg/sec

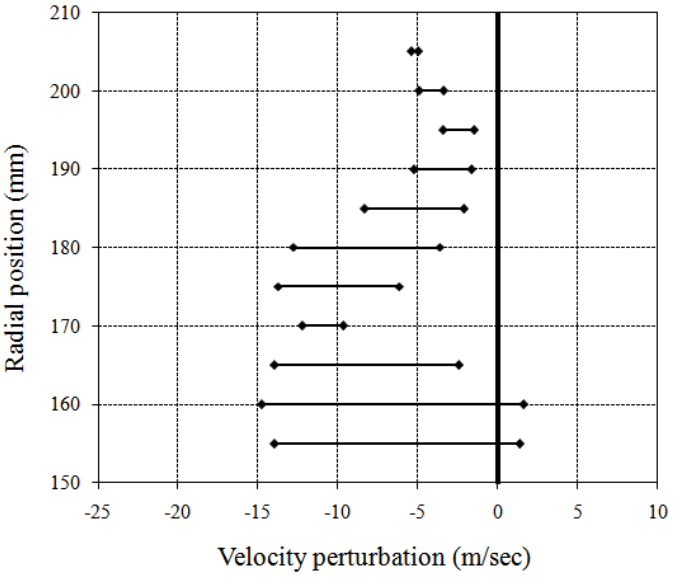

Figure C.8: Radial velocity perturbation relative to mean velocity for various radial positions with 1200 Hz radial excitation with a mass flow rate of 19.9 x 10^{-3} kg/sec

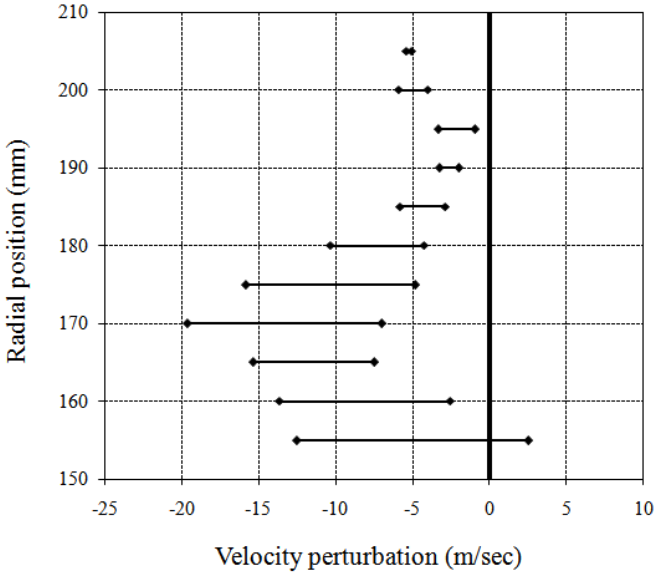

Figure C.9: Radial velocity perturbation relative to mean velocity for various radial positions with 1200 Hz radial excitation with a mass flow rate of 23.8 x 10^{-3} kg/sec

Appendix D

Results: Production nozzle axial velocity perturbation graphs

D.1 Axial excitation 60 Hz (production nozzle)

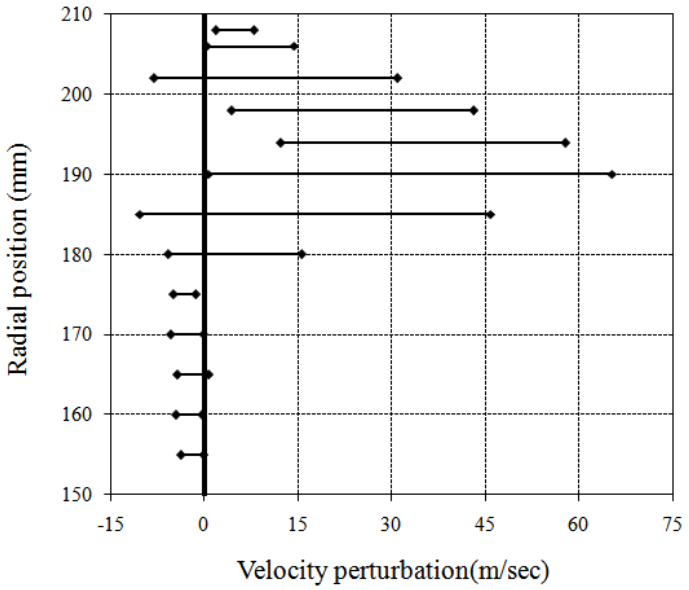

Figure D.1: Production nozzle axial velocity perturbation relative to mean velocity for various radial positions with 60 Hz axial excitation with a mass flow rate of 23.8 x 10^{-3} kg/sec

D.2 Axial excitation 650 Hz (production nozzle)

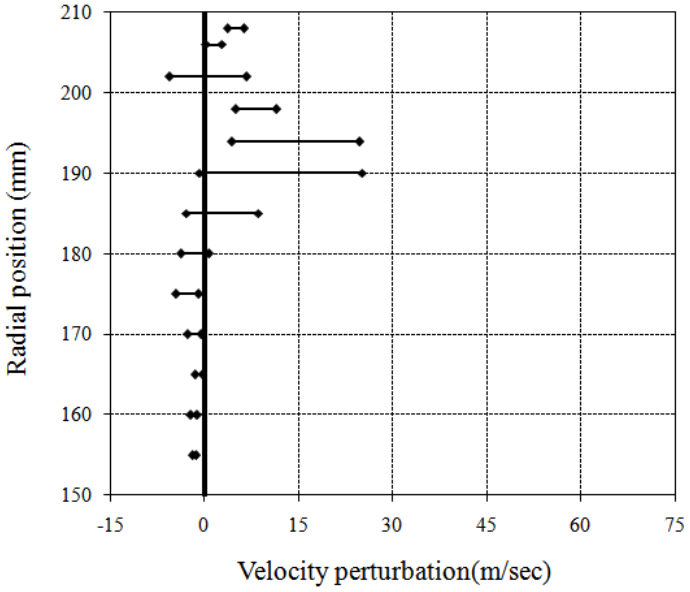

Figure D.2: Production nozzle axial velocity perturbation relative to mean velocity for various radial positions with 650 Hz axial excitation with a mass flow rate of 13.8 x 10^{-3} kg/sec

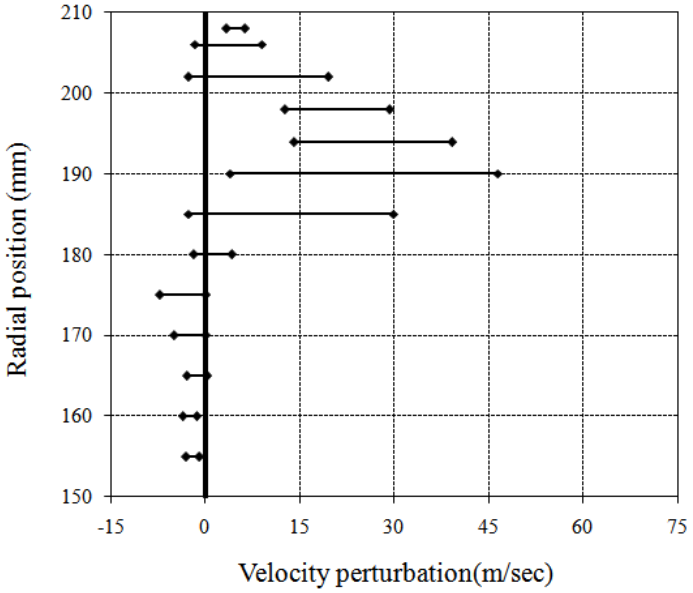

Figure D.3: Production nozzle axial velocity perturbation relative to mean velocity for various radial positions with 650 Hz axial excitation with a mass flow rate of 19.9 x 10^{-3} kg/sec

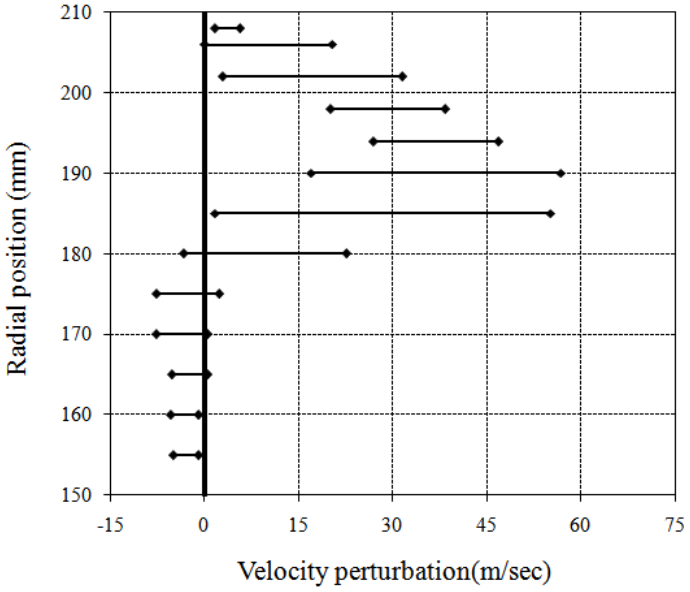

Figure D.4: Production nozzle axial velocity perturbation relative to mean velocity for various radial positions with 650 Hz axial excitation with a mass flow rate of 23.8 x 10^{-3} kg/sec

D.3 Axial excitation 1200 Hz (production nozzle)

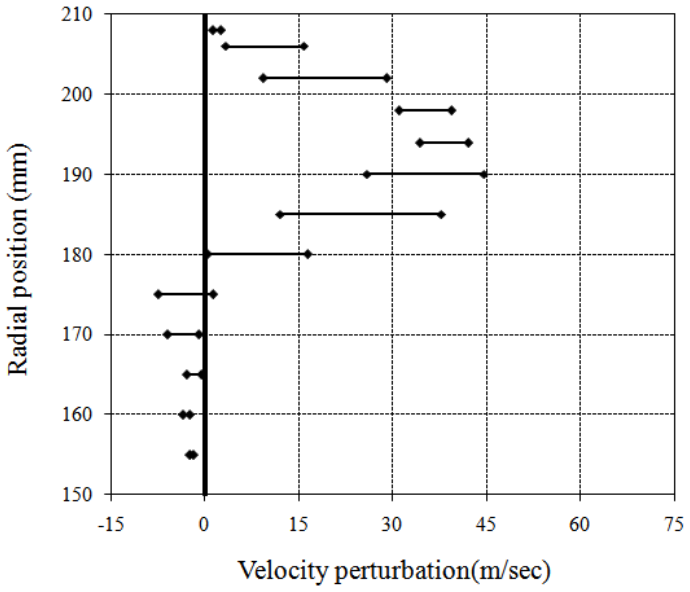

Figure D.5: Production nozzle axial velocity perturbation relative to mean velocity for various radial positions with 1200 Hz axial excitation with a mass flow rate of 23.8 x 10^{-3} kg/sec

Appendix E

Blade vibration testing: additional detail information

E.1 Half-bridge strain gauge calibration

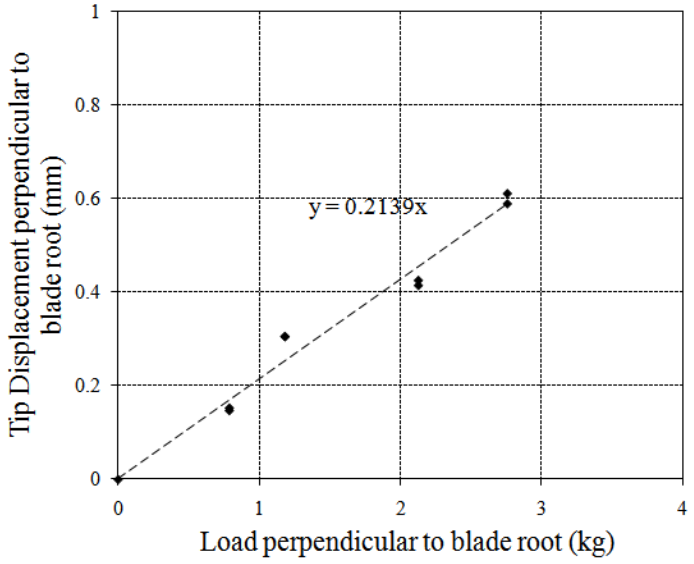

Figure E.1: Blade 3 point load perpendicular to blade root vs tip displacement perpendicular to blade root

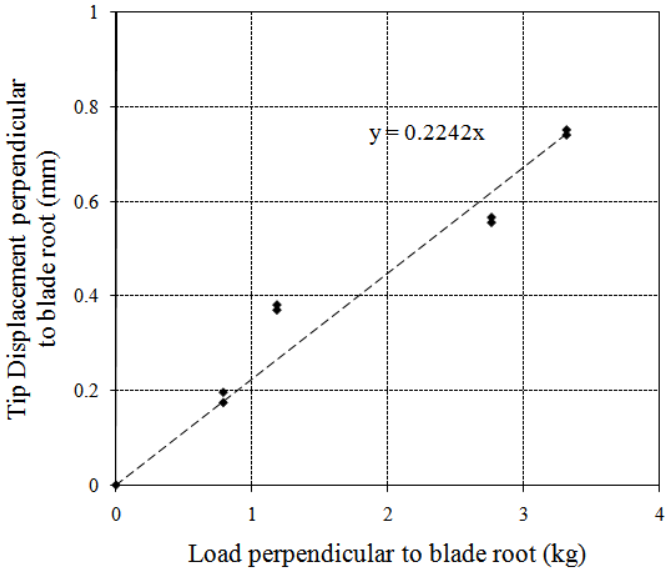

Figure E.2: Blade 25 point load perpendicular to blade root vs tip displacement perpendicular to blade root

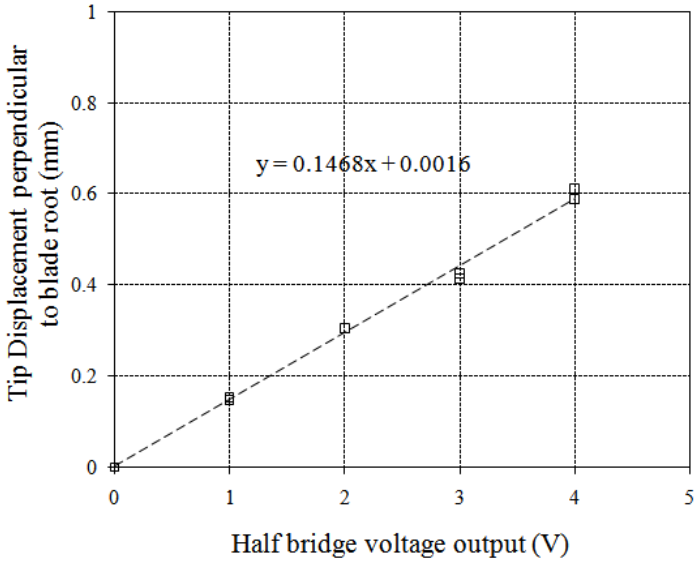

Figure E.3: Blade 3 tip displacement perpendicular to blade root vs half-bridge voltage output

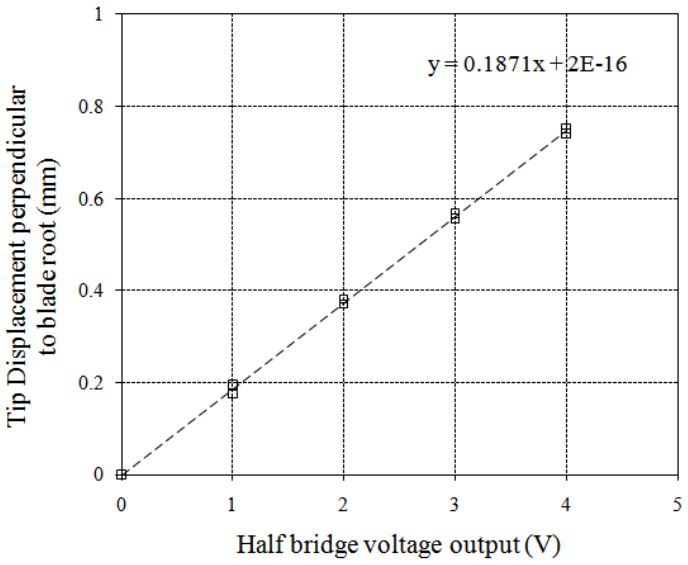

Figure E.4: Blade 25 tip displacement perpendicular to blade root vs half-bridge voltage output

E.2 Phase 2: Single exciter test FFT summary graphs

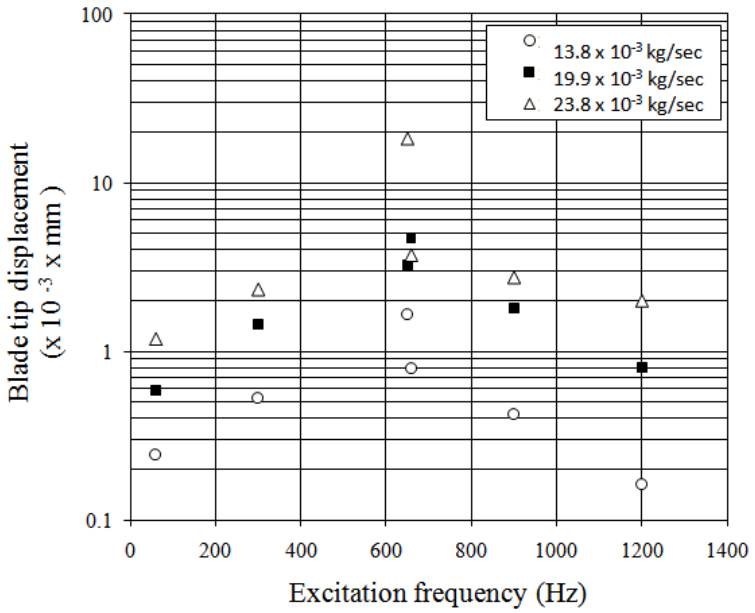

Figure E.5: Summary of blade 3 tip displacement vibration amplitude at the blade natural frequency plotted for various excitation frequencies and supply mass flow rates

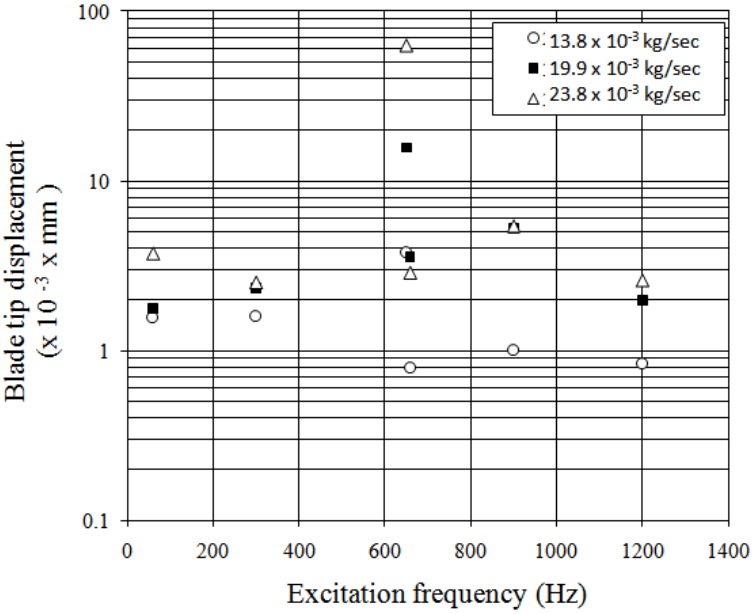

Figure E.6: Summary of blade 25 tip displacement vibration amplitude at the blade natural frequency plotted for various excitation frequencies and supply mass flow rates

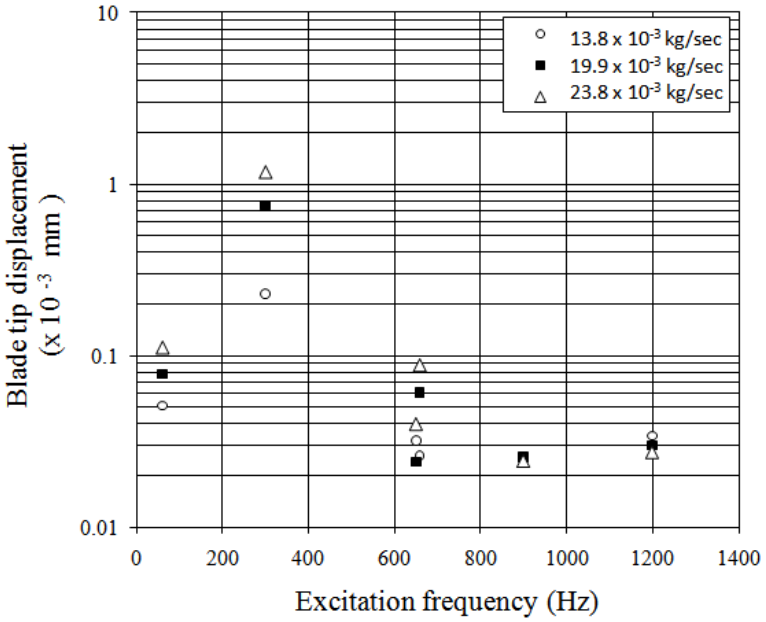

Figure E.7: Summary of blade 3 tip displacement vibration amplitude at the excitation first harmonic frequency plotted for various excitation frequencies and supply mass flow rates

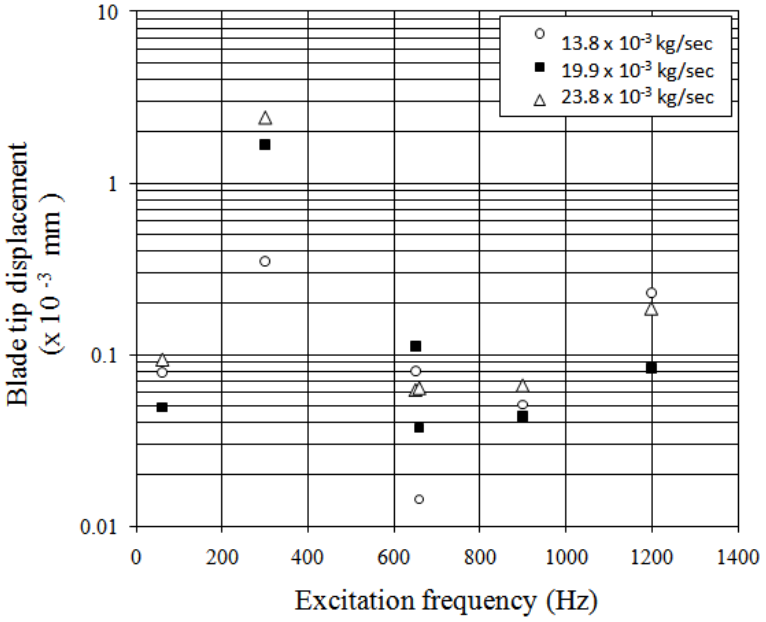

Figure E.8: Summary of blade 25 tip displacement vibration amplitude at the excitation first harmonic frequency plotted for various excitation frequencies and supply mass flow rates

Appendix F

Evaluation of variation on simulation baseline model

F.1 Effect of the number of flow paths

All grid settings were the same as described in section 5.2.1, except for the number of flow paths. The grid is constructed of rectangular cells that form layers of cells with the same height. The cells are in effect stacked in layers from the hub to the casing in a radial direction. These layers are also referred to as flow paths. Two variations in the number of flow paths were investigated. The first was a higher number of flow paths than the base line (called Flow path 61/73) and the second was lower than the base line model (called Flow path 29/33). For the generation of the Flow path 29/33 model, the number of flow paths were decreased iteratively until a point where the grid parameters exceeded the grid quality requirements as mentioned in table 5.2. Flow path 29/33 was the smallest grid that was within the Numeca prescribed quality requirements. The model details are as follows:

- Flow path 61/73: 61 flow paths for stator stages and 73 flow paths for rotor stages
- Flow path 33/45: 33 flow paths for stator stages and 45 flow paths for rotor stages

The solver was set up with exactly the same settings as the base line model settings described in section 5.2.1. The result was that Flow path 61/73 performed exactly the same as the base line model, producing a pressure ratio of 1.031 at a mass flow rate of 2.63 kg/sec. Flow path 29/33 produced a pressure ratio of 1.0311 at a mass flow rate of 2.63 kg/sec - slightly higher than the base line model.

F.2 Effect of the wall cell width

All grid settings were as described in section 5.2.1, except for the wall cell width. During the Wizard grid generation process, the wall cell thickness was specified as 0.00512 mm. This variation was determined by changing the velocity variable V_{ref} in equation 5.2.1 to 66.5 m/sec, the relative velocity of flow over the rotating blade. The relative velocity over the blade was calculated as follows:

$$W_1 = \sqrt{C_a^2 + U^2} \tag{F.2.1}$$

where C_a is the axial velocity of 35 m/sec and U, the tangential velocity is calculated as:

$$U = \Omega r_1 \tag{F.2.2}$$

where r_1 is the mid span radius of 0.18 m and Ω, the angular velocity of the blade:

$$\Omega = \frac{\pi N}{60} \tag{F.2.3}$$

where N, the rotation speed is 3000 RPM. The value for Ω was therefore 157.08 rad/sec.

The solver was set up with the same settings as the base line model settings described in section 5.2.1. The result was that the new model, named Wall Cell 5.12μm performed exactly as the base line model, producing a pressure ratio of 1.031 at a mass flow rate of 2.63 kg/sec.

The effect of the wall cell width was also evaluated with respect to the y^+ values produced by the two models. Using the CFView module in Numeca, a graphic display of the y^+ value distribution on the first rotor blade for the two models was obtained. Figure F.1 shows that the Wall Cell 5.12μm model produced y^+ values that varied between 0.5 and 1, very similar to the y^+ values produced by the base line model (Wall Cell 8.5μm). Therefore, based on the y^+ value distribution, the two settings performed equally well.

F.3 Solver setting: Rotor/Stator interface

To evaluate the effect of the rotor/stator interface coupling, the Rotor-Stator interface in the Rotating Machinery section of FINE™/Turbo was set to Conservative Coupling. All settings were as described in section 5.2.1.

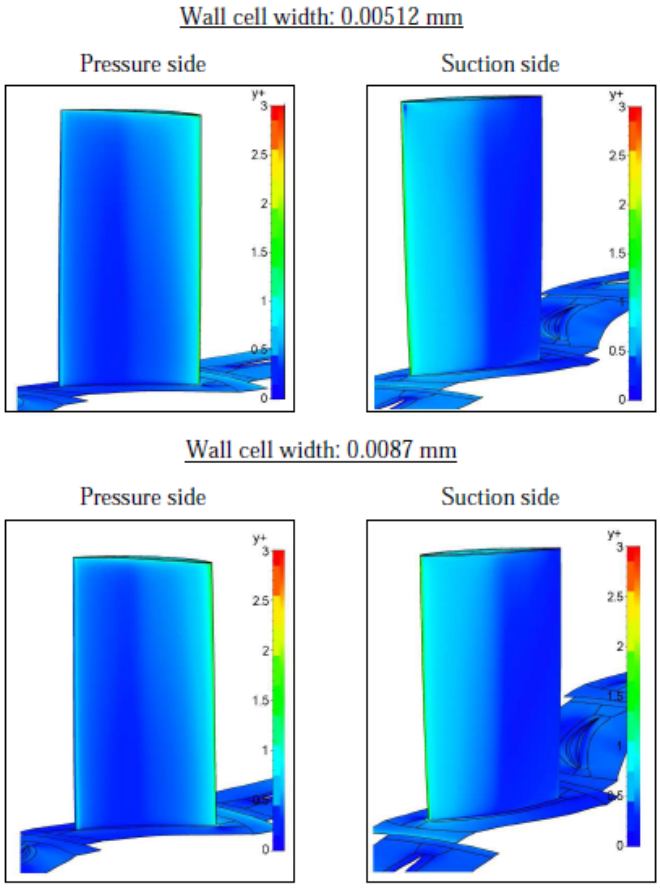

Figure F.1: Plot of y^+ values for simulations with wall width settings of 0.00512 mm and 0.0085 mm respectively

The solution produced a pressure ratio of 1.031 at a mass flow rate of 2.63 kg/sec, exactly the same as the base line model.

F.4 Velocity profile as boundary condition

The last evaluation of the base line model performance was to define a different type of boundary condition. Instead of specifying the mass flow rate, the inlet boundary condition was defined as a pre-defined velocity profile. For the unsteady simulations, this profile was specified so that results could be compared to experimental results. This test provided valuable input data for the more complex simulations that will be described in the next few sections. The velocity profile was obtained by measuring the axial velocity profile in front of the first rotor stage with a hot wire anemometer. The anemometer was traversed in a radial direction to obtain the velocity magnitudes for a number of radial positions. The details of this test, the equipment and how the results

were obtained are provided in section 4.4 and in appendix J in the attached CD.

The base line grid with a wall cell width of 0.00512 mm was used for the simulation. All other mesh settings were as described in the mesh set-up description in section 5.2.1.

The model solver was set-up in FINE™/Turbo, using the same settings as the base line set-up described in section 5.2.1, except that the experimentally measured profile given by figure 4.11 was defined as the velocity magnitude in the z-direction (Vz). The outlet boundary condition was defined by specifying the pressure of 101300 Pa and imposing a radial equilibrium at a radius of 0.18 m.

As with previous tests, the solution was considered as converged when the mass flow rate balance was less than 3 orders of the mass flow rate magnitude. The result was a mass flow rate of 3.01 kg/sec, which was slightly higher than the measured mass flow rate of 2.8 kg/sec.

Appendix G

Correlation between experimental and simulation axial velocity profiles

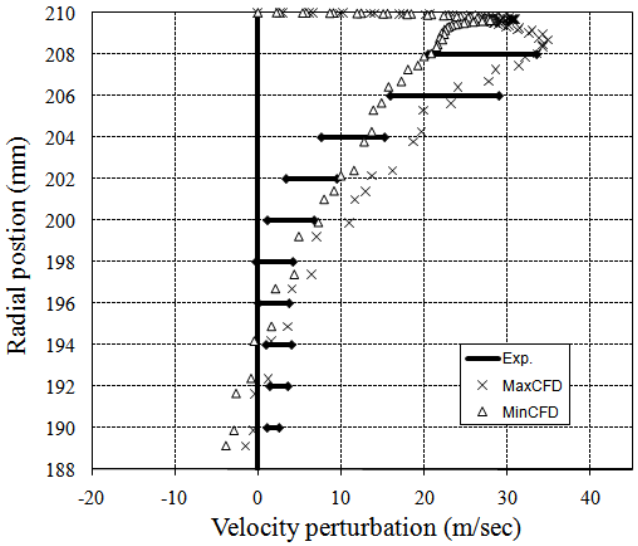

Figure G.1: Axial velocity perturbation relative to the mean velocity for 1200 Hz axial excitation: Experimental vs CFD results

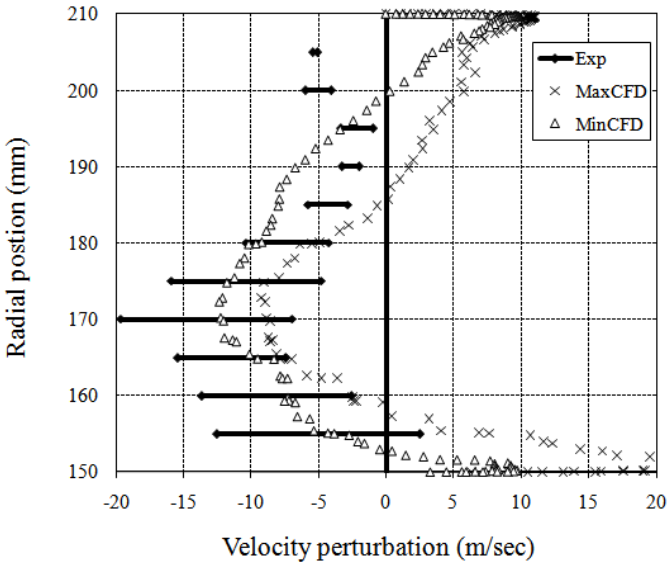

Figure G.2: Axial velocity perturbation relative to the mean velocity for 1200 Hz radial excitation: Experimental vs CFD results

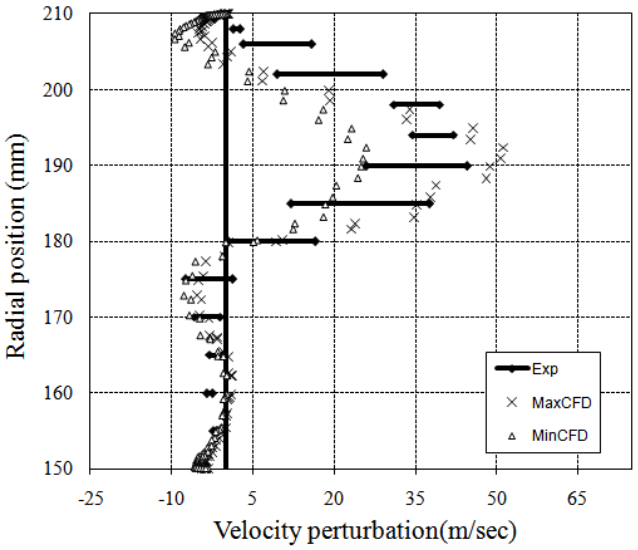

Figure G.3: Axial velocity perturbation relative to the mean velocity for 1200 Hz production axial excitation: Experimental vs CFD results

Appendix H

Results: Simulation results force time series and force FFTs

H.1 Force response to 650 Hz axial excitation

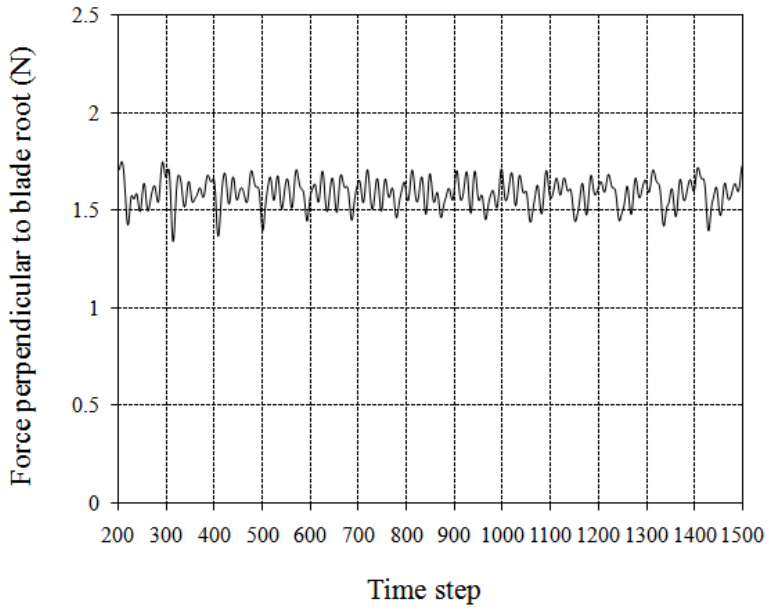

Figure H.1: Force time series for one revolution response to 650 Hz Axial excitation

H.2 Force response to 1200 Hz axial excitation

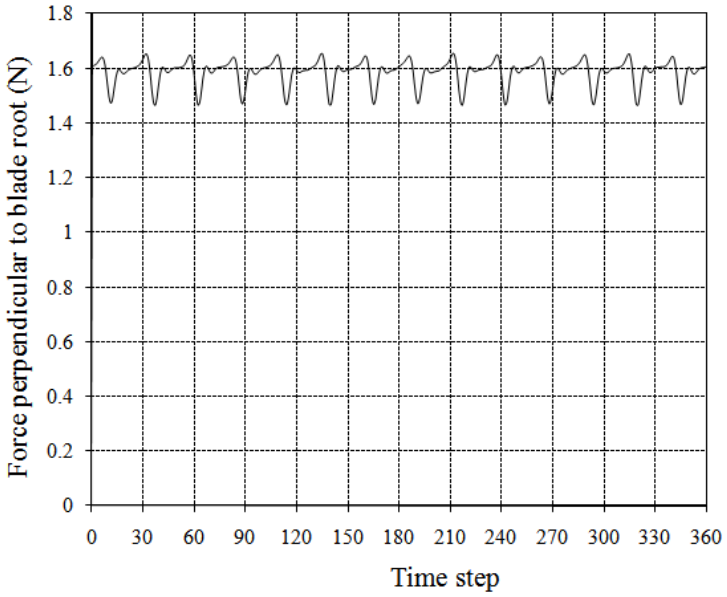

Figure H.2: Force time series for one revolution response to 1200 Hz Axial excitation

H.3 Force response to 1200 Hz Radial excitation

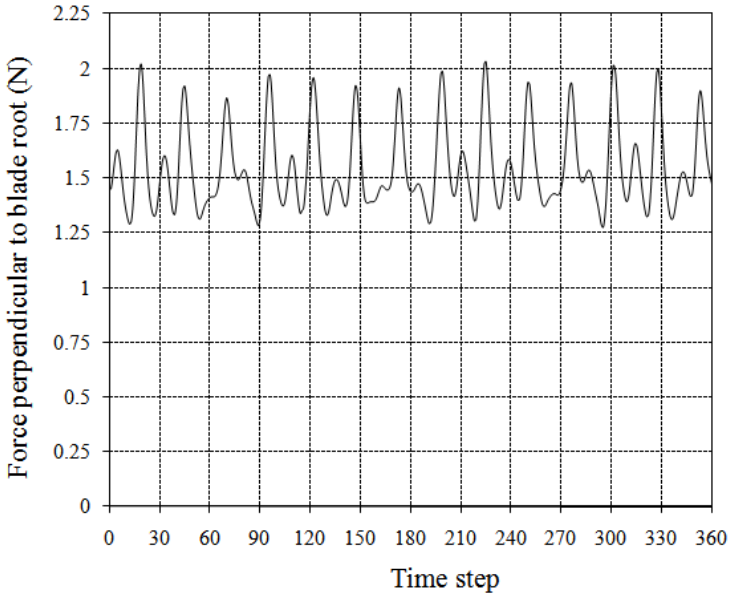

Figure H.3: Force time series for one revolution response to 1200 Hz Radial excitation

H.4 Force response to 1200 Hz Production Axial excitation

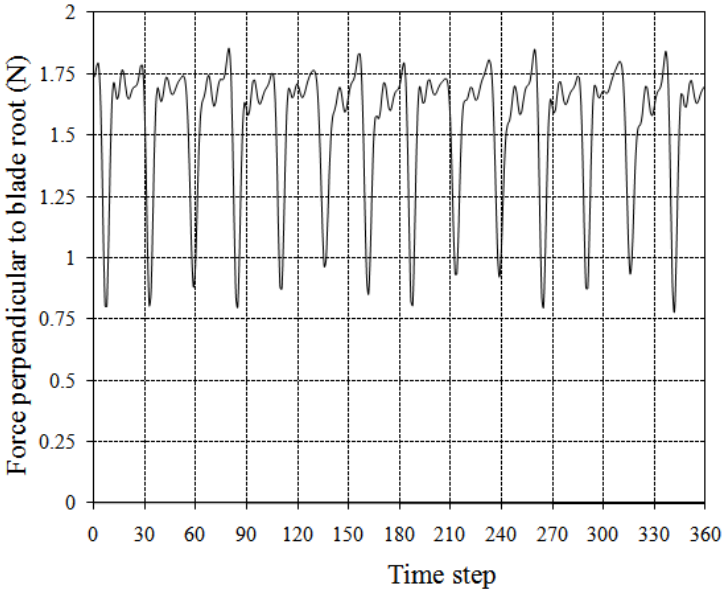

Figure H.4: Force time series for one revolution response to 1200 Hz Production Axial excitation

Appendix I

Results of mathematical modelling of blade force frequency response

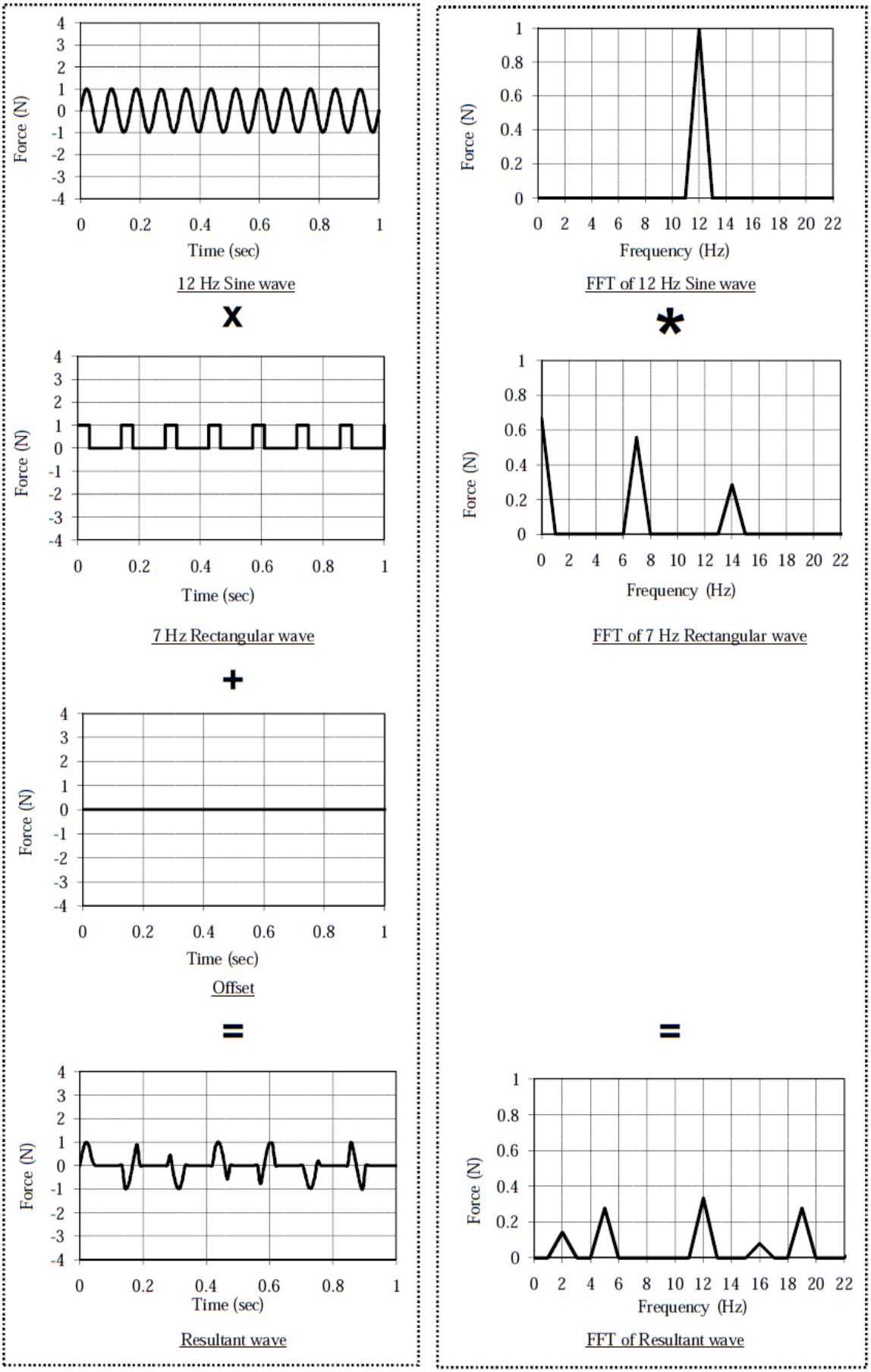

Figure I.1: Mathematical model of a sine wave with no offset and the resultant wave with no offset

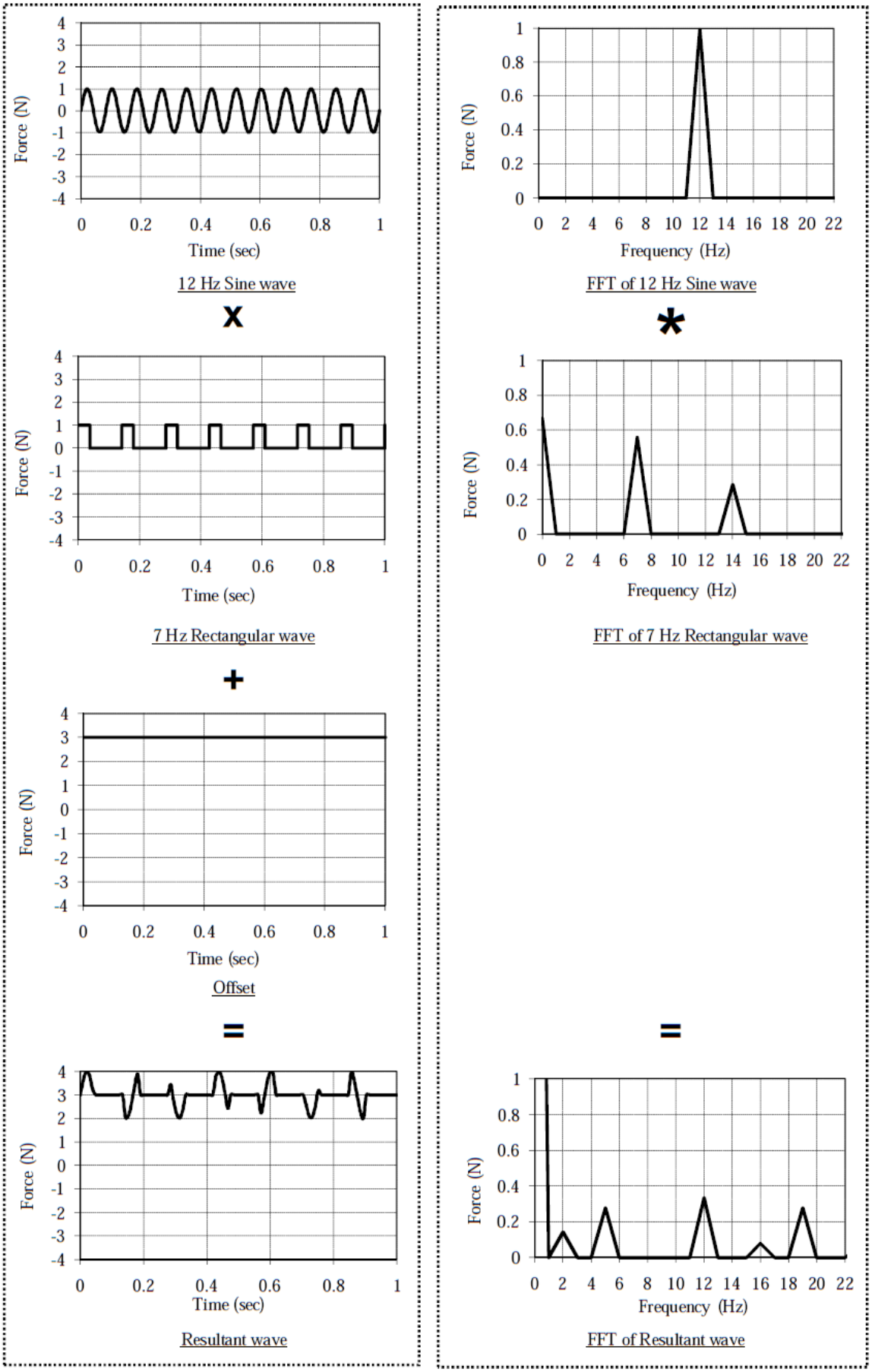

Figure I.2: Mathematical model of a sine wave with no offset and the resultant wave with an offset

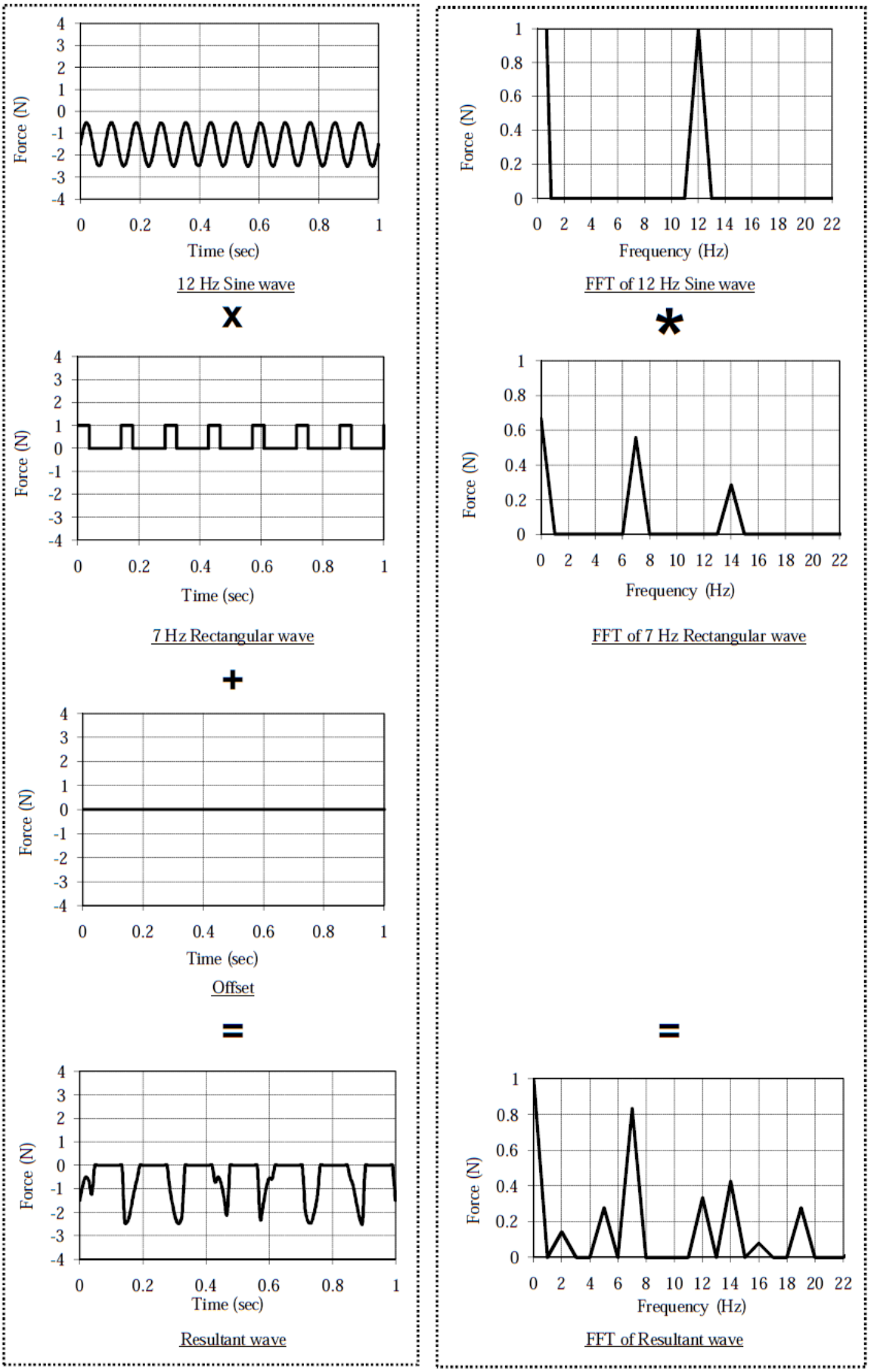

Figure I.3: Mathematical model of a sine wave with an offset and the resultant wave with no offset

Appendix J

Mean axial velocity profile verification

In section 4.4.4 the axial velocity profile is given by figure 4.11. This profiles looks significantly different to the profile that was measured and documented by Roos (1995). Two other operating points were also measured. In both cases the profile looks similar to figure 4.11. It was suspected that the profile was the result of a lack of sealing around the hot film probe, which resulted in leakage through the casing and subsequently a different axial velocity profile. Figure J.1 shows that the axial velocity profile is not significantly affected by improved sealing around the hot film probe.

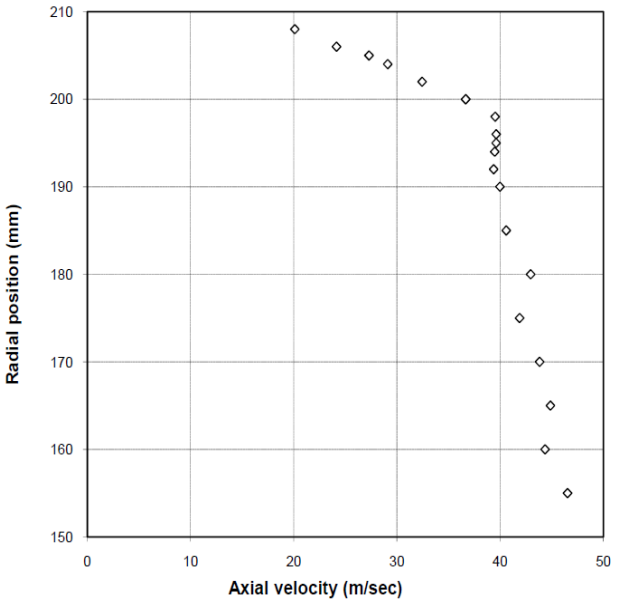

Figure J.1: Mean axial velocity for various radial positions at a mass flow rate of 2.77 kg/sec (second measurement)

Appendix K

Results: FFT of Axial velocity perturbation

K.1 Axial excitation 60 Hz

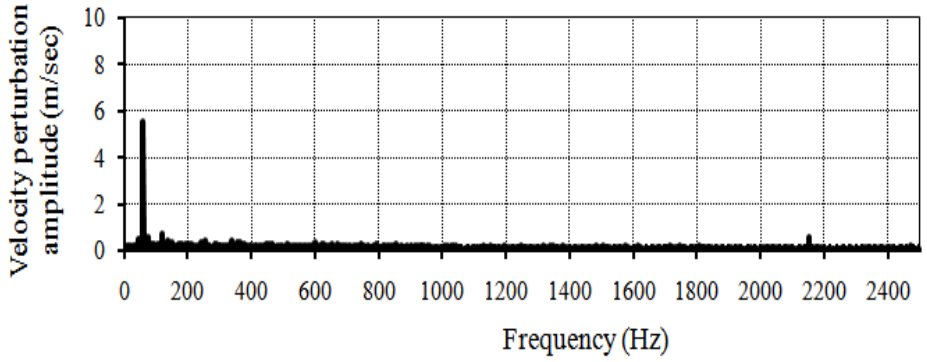

Figure K.1: FFT of axial velocity perturbation, 58 mm radial position, 60 Hz excitation, mass flow rate of 13.8 x 10^{-3} kg/sec

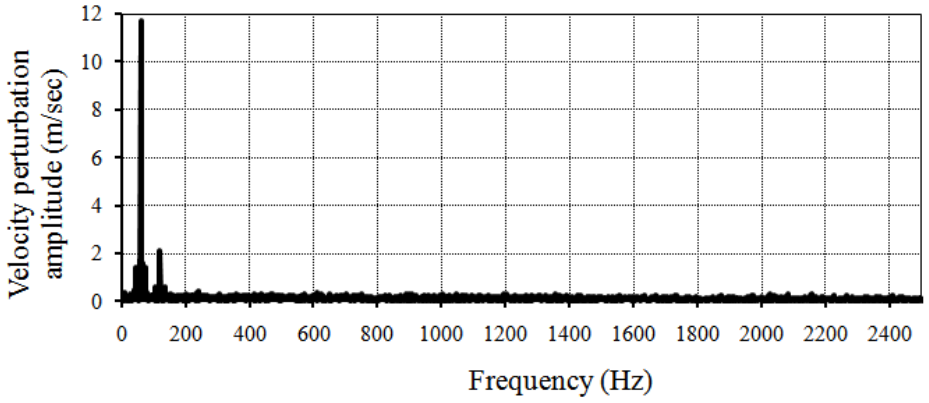

Figure K.2: FFT of axial velocity perturbation, 58 mm radial position, 60 Hz excitation, mass flow rate of 19.9 x 10^{-3} kg/sec

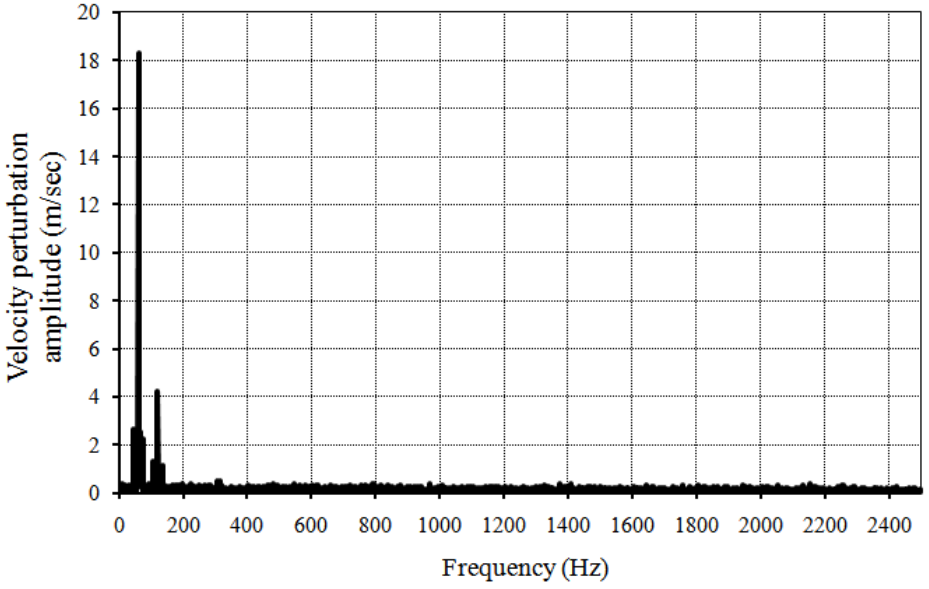

Figure K.3: FFT of axial velocity perturbation, 58 mm radial position, 60 Hz excitation, mass flow rate of 23.8 x 10^{-3} kg/sec

K.2 Axial excitation 650 Hz

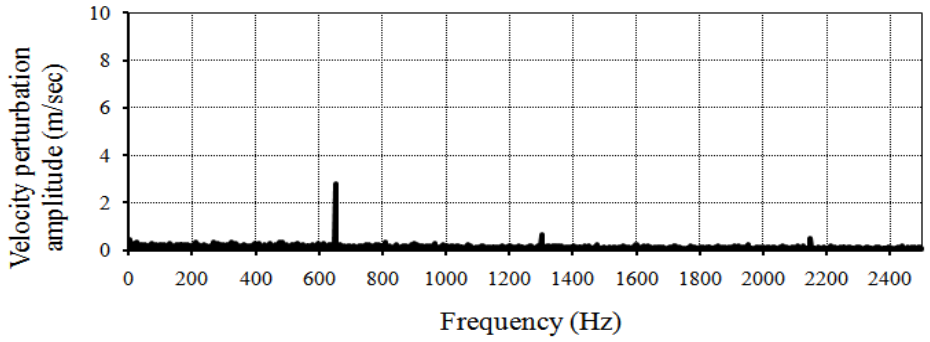

Figure K.4: FFT of axial velocity perturbation, 58 mm radial position, 650 Hz excitation, mass flow rate of 13.8 x 10^{-3} kg/sec

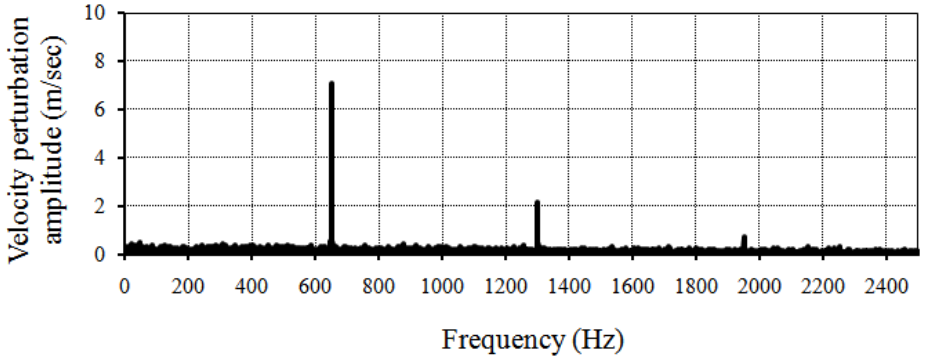

Figure K.5: FFT of axial velocity perturbation, 56 mm radial position, 650 Hz excitation, mass flow rate of 19.9 x 10^{-3} kg/sec

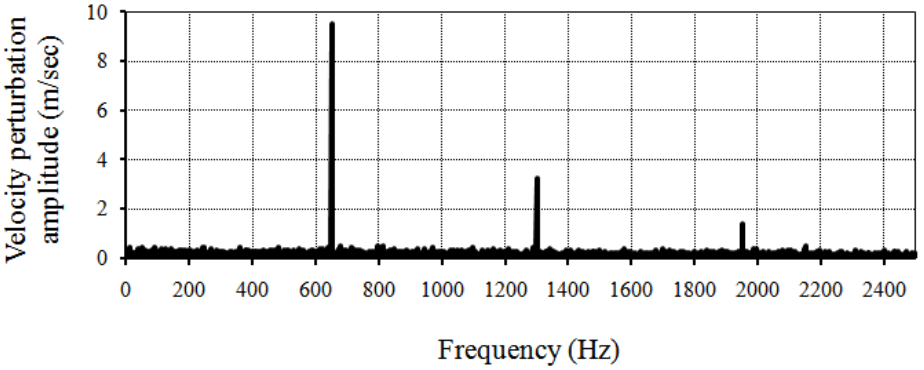

Figure K.6: FFT of axial velocity perturbation, 56 mm radial position, 650 Hz excitation, mass flow rate of 23.8 x 10^{-3} kg/sec

K.3 Axial excitation 1200 Hz

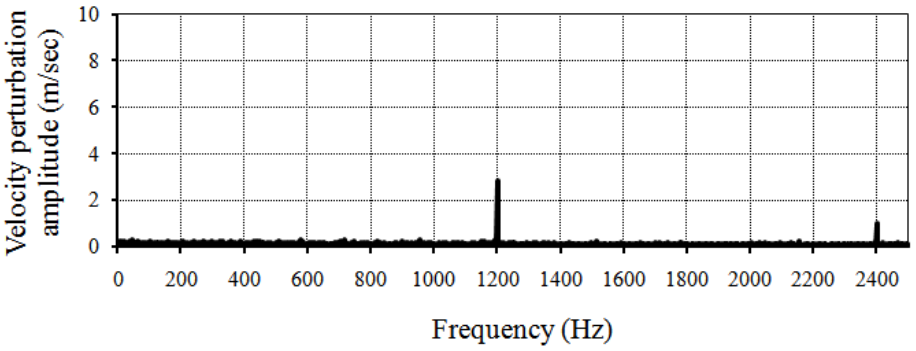

Figure K.7: FFT of axial velocity perturbation, 58 mm radial position, 1200 Hz excitation, mass flow rate of 13.8 x 10^{-3} kg/sec

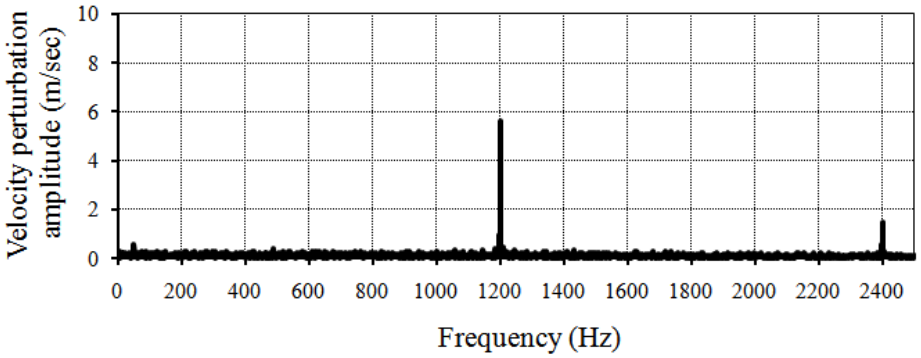

Figure K.8: FFT of axial velocity perturbation, 56 mm radial position, 1200 Hz excitation, mass flow rate of 19.9 x 10^{-3} kg/sec

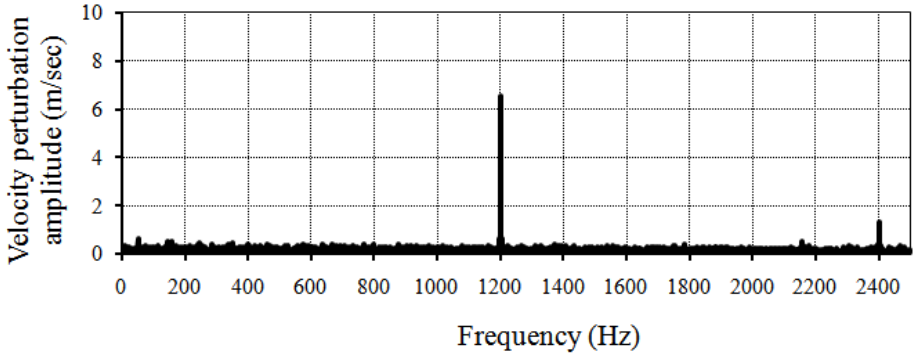

Figure K.9: FFT of axial velocity perturbation, 56 mm radial position, 1200 Hz excitation, mass flow rate of 23.8 x 10^{-3} kg/sec

Appendix L

Results: FFT of Radial velocity perturbation

L.1 Radial excitation 60 Hz

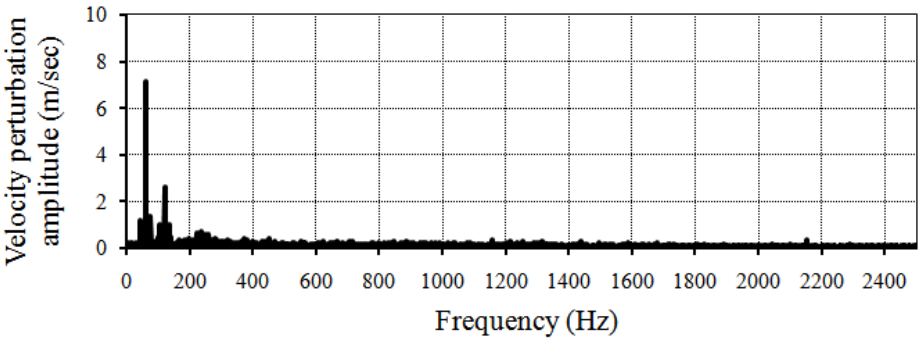

Figure L.1: FFT of radial velocity perturbation, 30 mm radial position, 60 Hz excitation, mass flow rate of 13.8 x 10^{-3} kg/sec

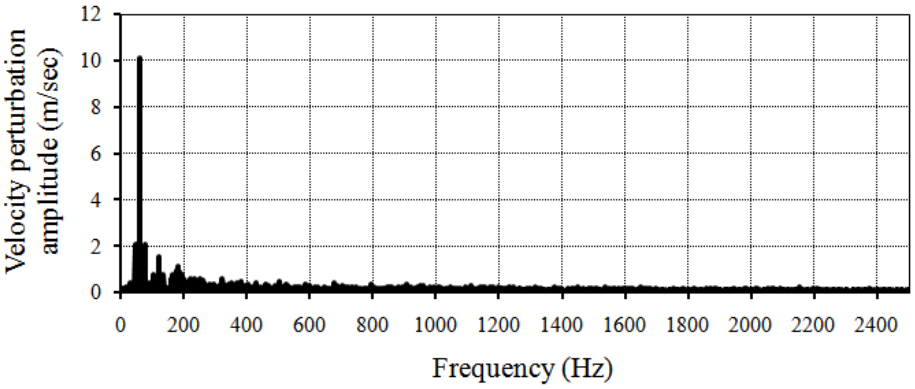

Figure L.2: FFT of radial velocity perturbation, 20 mm radial position, 60 Hz excitation, mass flow rate of 19.9 x 10^{-3} kg/sec

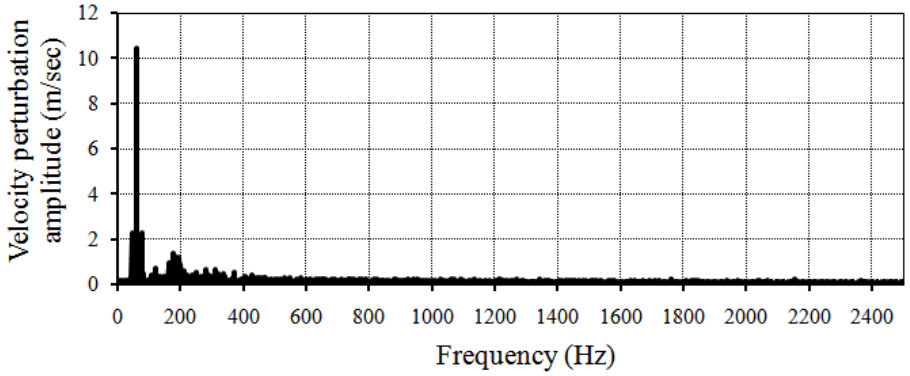

Figure L.3: FFT of radial velocity perturbation, 15 mm radial position, 60 Hz excitation, mass flow rate of 23.8 x 10^{-3} kg/sec

L.2 Radial excitation 650 Hz

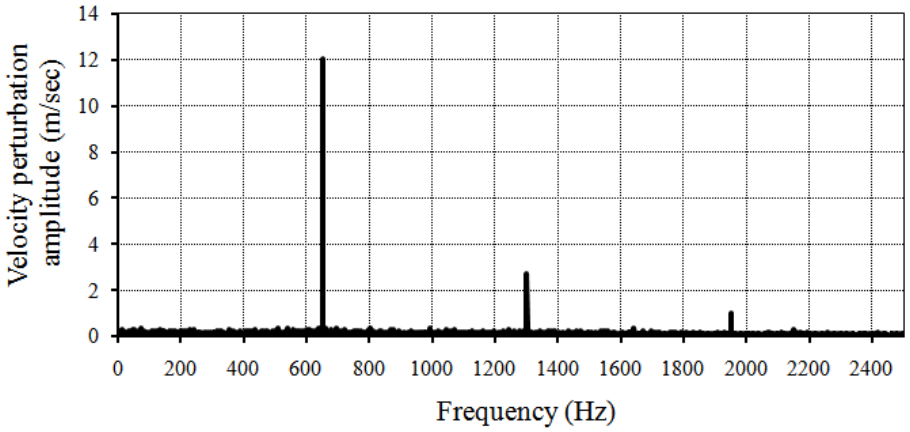

Figure L.4: FFT of radial velocity perturbation, 20 mm radial position, 650 Hz excitation, mass flow rate of 13.8 x 10^{-3} kg/sec

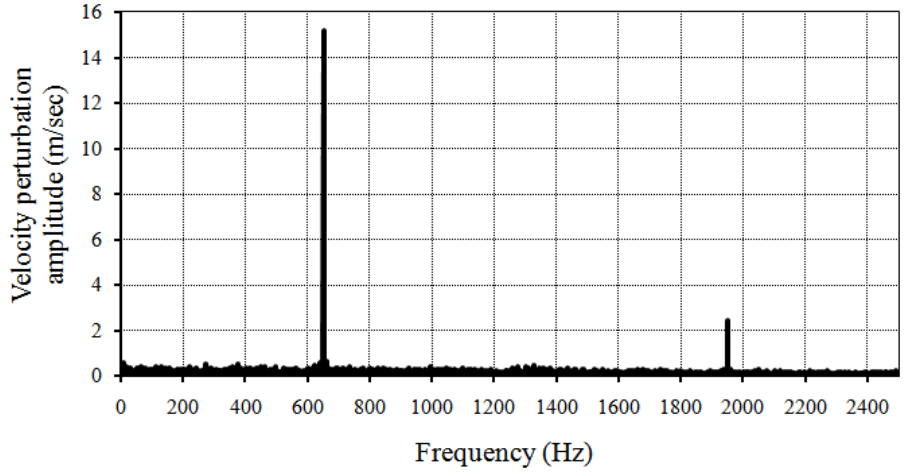

Figure L.5: FFT of radial velocity perturbation, 10 mm radial position, 650 Hz excitation, mass flow rate of 19.9 x 10^{-3} kg/sec

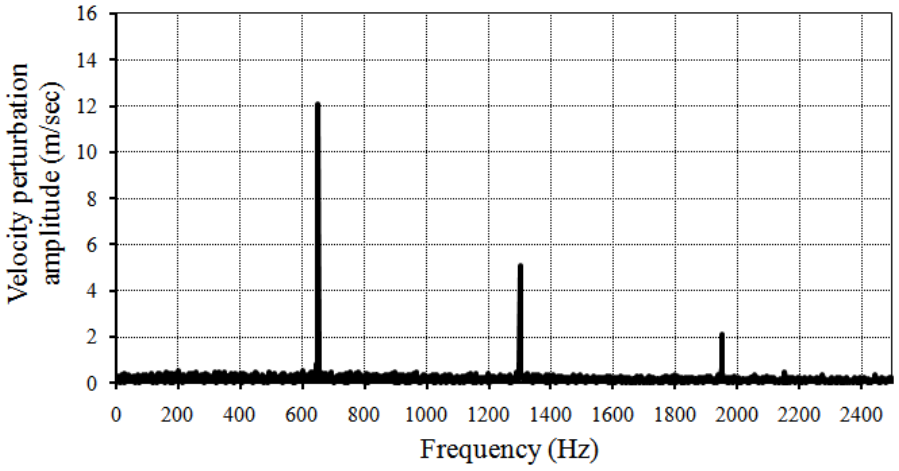

Figure L.6: FFT of radial velocity perturbation, 10 mm radial position, 650 Hz excitation, mass flow rate of 23.8 x 10^{-3} kg/sec

L.3 Radial excitation 1200 Hz

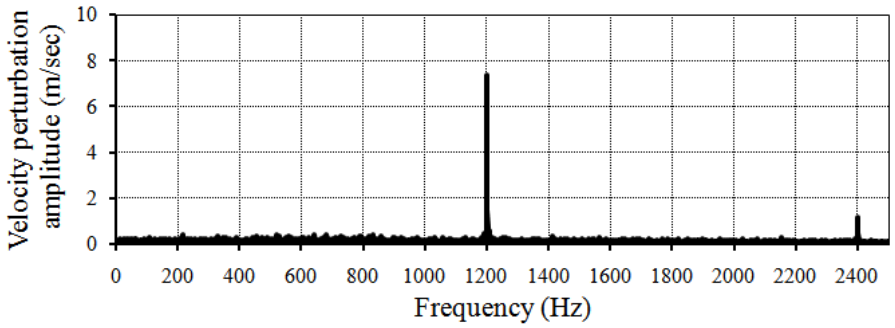

Figure L.7: FFT of radial velocity perturbation, 20 mm radial position, 1200 Hz excitation, mass flow rate of 13.8 x 10^{-3} kg/sec

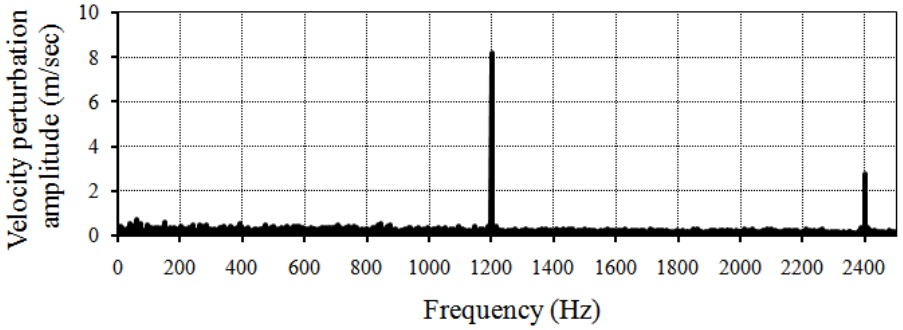

Figure L.8: FFT of radial velocity perturbation, 10 mm radial position, 1200 Hz excitation, mass flow rate of 19.9 x 10^{-3} kg/sec

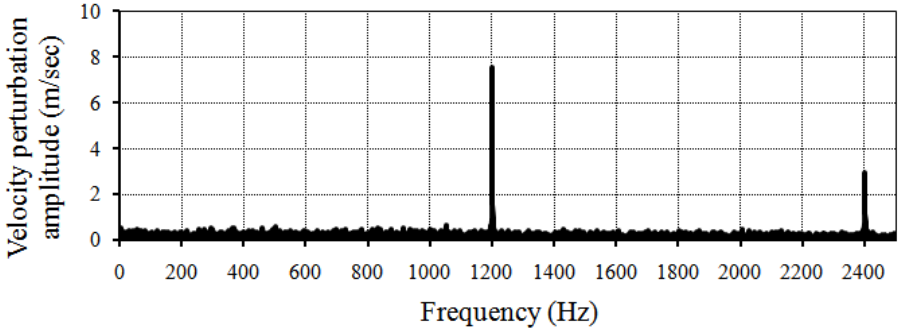

Figure L.9: FFT of radial velocity perturbation, 5 mm radial position, 1200 Hz excitation, mass flow rate of 23.8 x 10^{-3} kg/sec

Appendix M

Results: Exciter nozzle outlet velocity variations

M.1 Radial nozzle

M.1.1 60 Hz excitation

Refer to figure 4.12 in section 4.5 of chapter 4.

M.1.2 650 Hz excitation

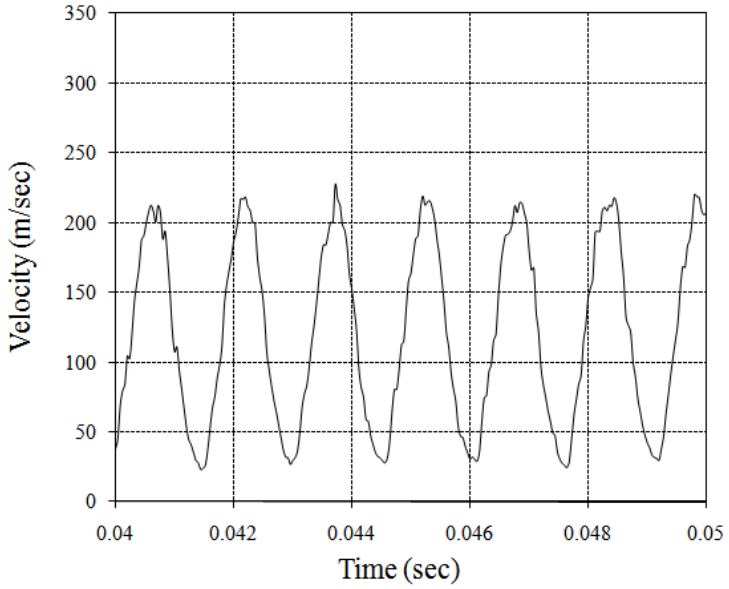

Figure M.1: Radial nozzle velocity profile near the nozzle outlet with a 650 Hz excitation and a supply a mass flow rate of 13.8 x 10^{-3} kg/sec

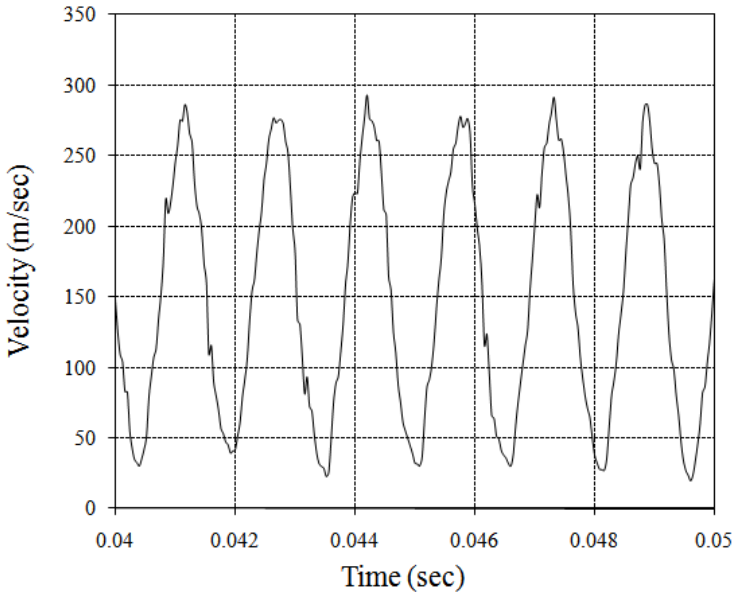

Figure M.2: Radial nozzle velocity profile near the nozzle outlet with a 650 Hz excitation and a supply mass flow rate of 19.9 x 10^{-3} kg/sec

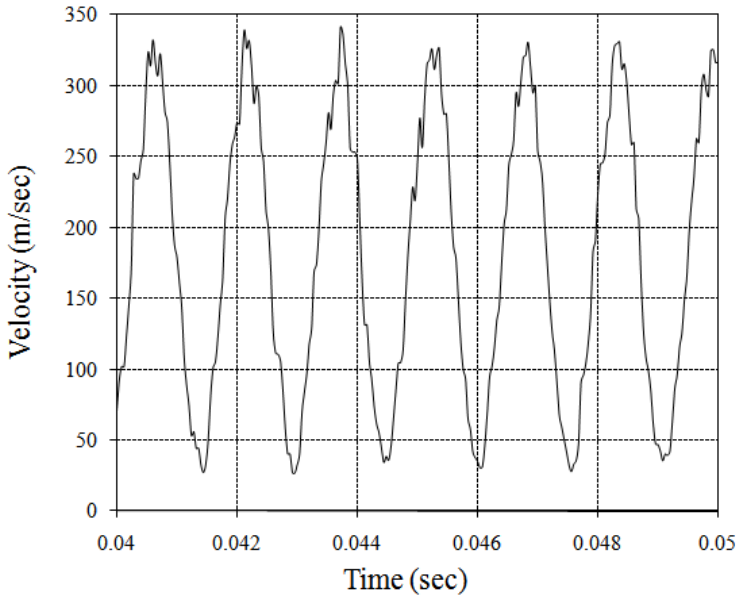

Figure M.3: Radial nozzle velocity profile near the nozzle outlet with a 650 Hz excitation and asupply mass flow rate of 23.8 x 10^{-3} kg/sec

M.2 1200 Hz excitation

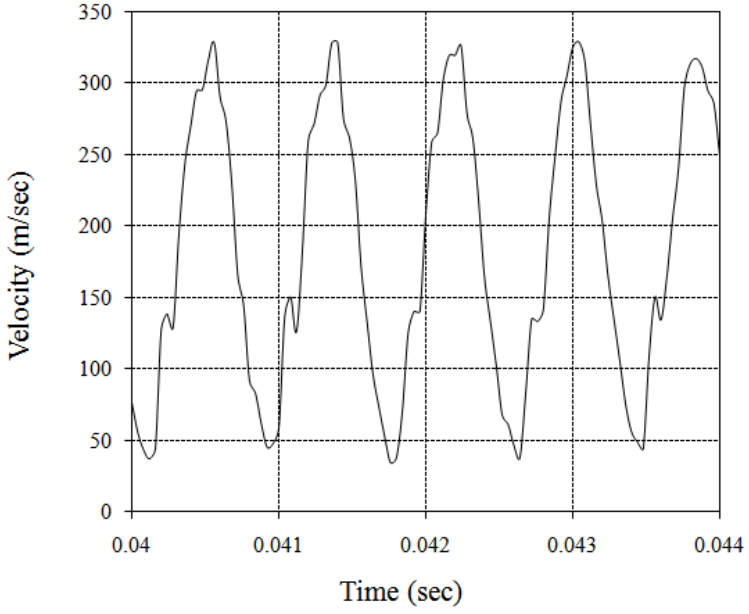

Figure M.4: Radial nozzle velocity profile near the nozzle outlet with a 1200 Hz excitation and a supply mass flow rate of 23.8 x 10^{-3} kg/sec

M.3 Production axial nozzle

M.3.1 60 Hz excitation

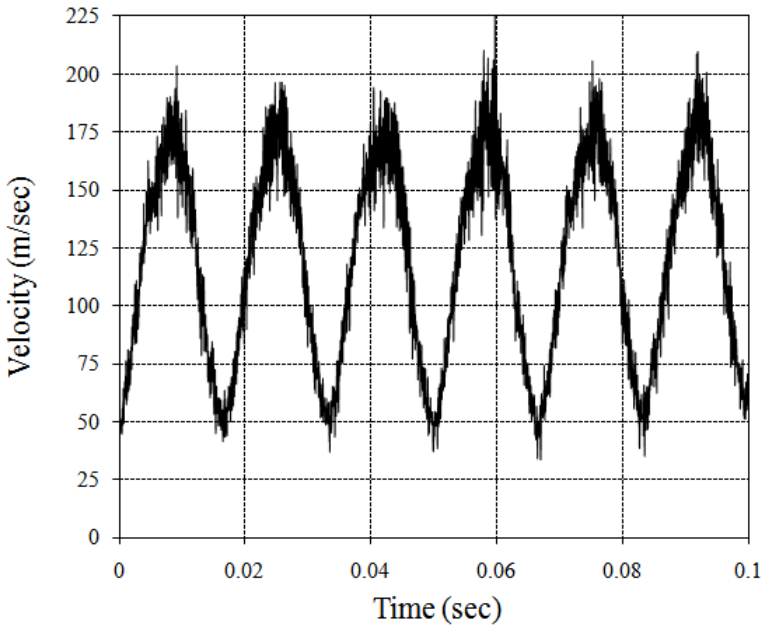

Figure M.5: Production nozzle velocity profile near the nozzle outlet with a 60 Hz excitation and asupply mass flow rate of 23.8 x 10^{-3} kg/sec

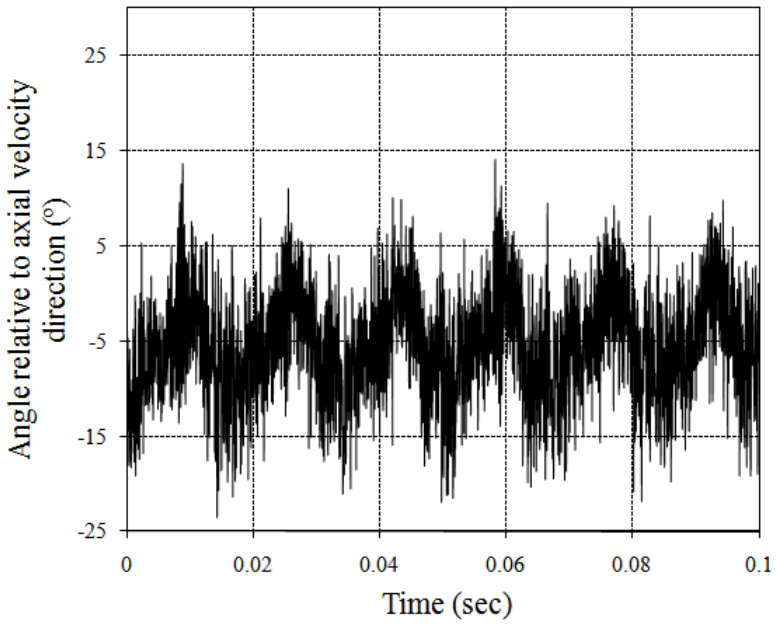

Figure M.6: Production nozzle velocity outflow angle near the nozzle outlet with a 60 Hz excitation and a supply mass flow rate of 23.8 x 10^{-3} kg/sec

M.3.2 650 Hz excitation

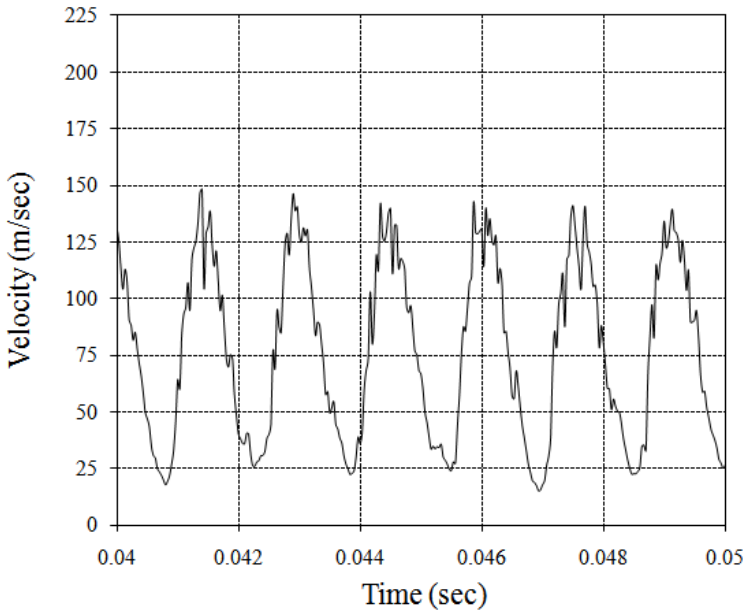

Figure M.7: Production nozzle velocity profile near the nozzle outlet with a 650 Hz excitation and supply a mass flow rate of 13.8 x 10^{-3} kg/sec

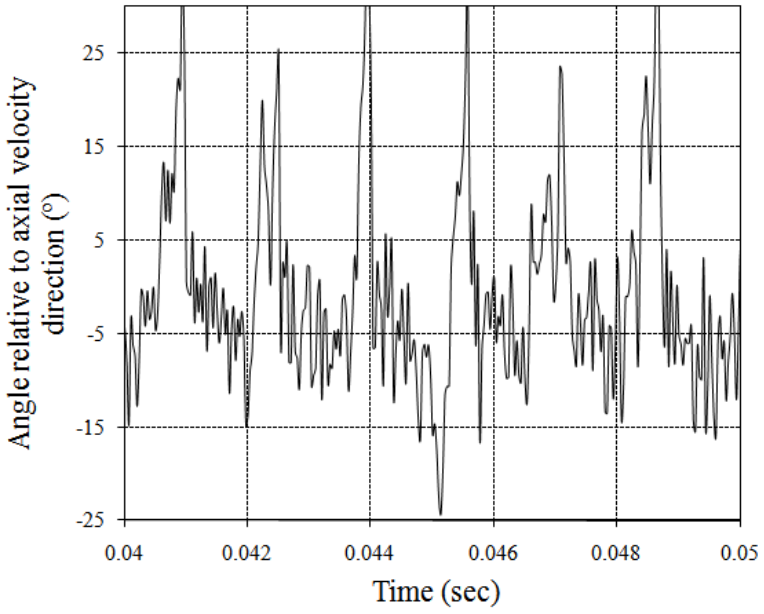

Figure M.8: Production nozzle velocity outflow angle near the nozzle outlet with a 650 Hz excitation and a supply mass flow rate of 13.8 x 10^{-3} kg/sec

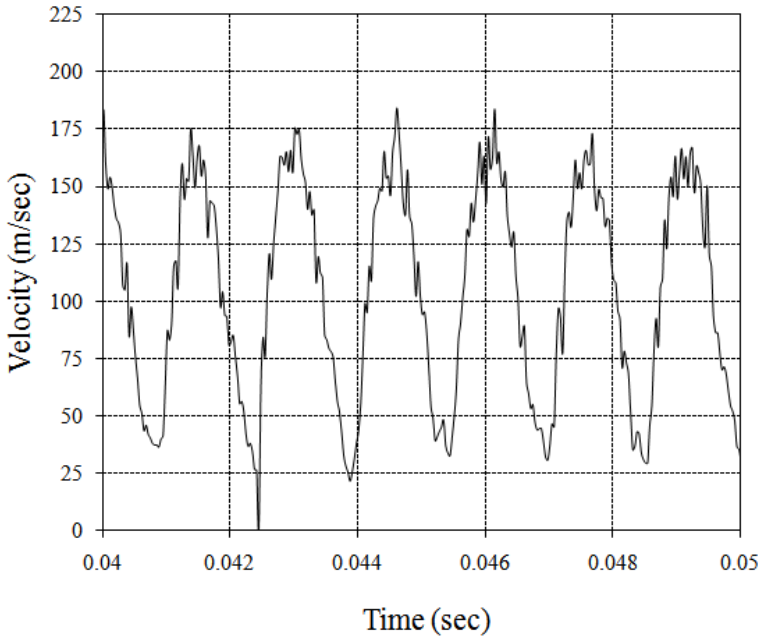

Figure M.9: Production nozzle velocity profile near the nozzle outlet with a 650 Hz excitation and a supply mass flow rate of 19.9 x 10^{-3} kg/sec

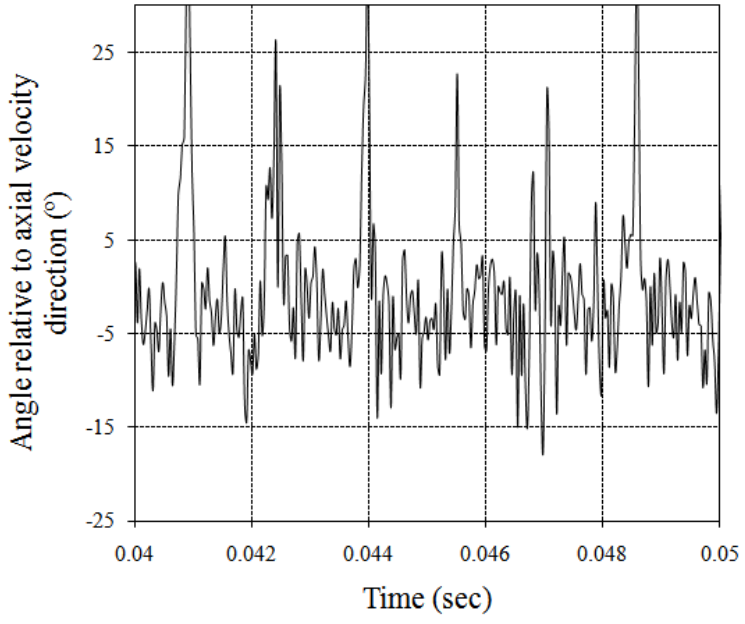

Figure M.10: Production nozzle velocity outflow angle near the nozzle outlet with a 650 Hz excitation and a supply mass flow rate of 19.9 x 10^{-3} kg/sec

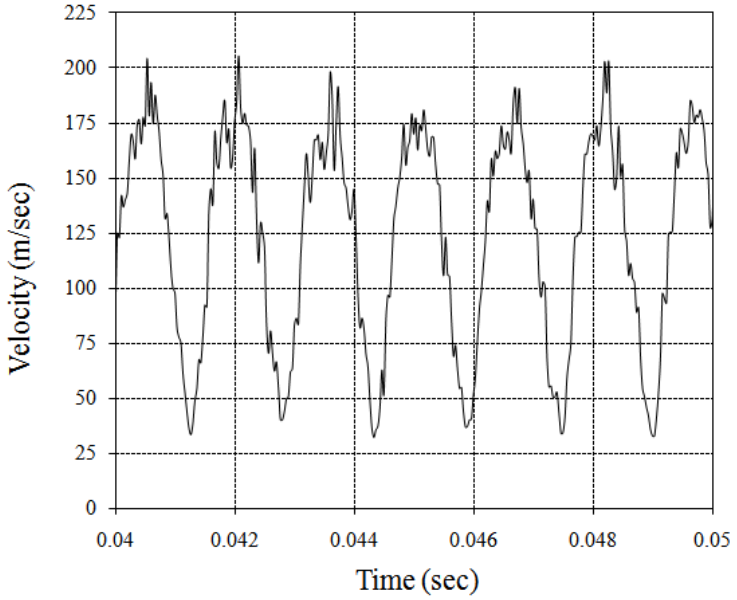

Figure M.11: Production nozzle velocity profile near the nozzle outlet with a 650 Hz excitation and asupply mass flow rate of 23.8 x 10^{-3} kg/sec

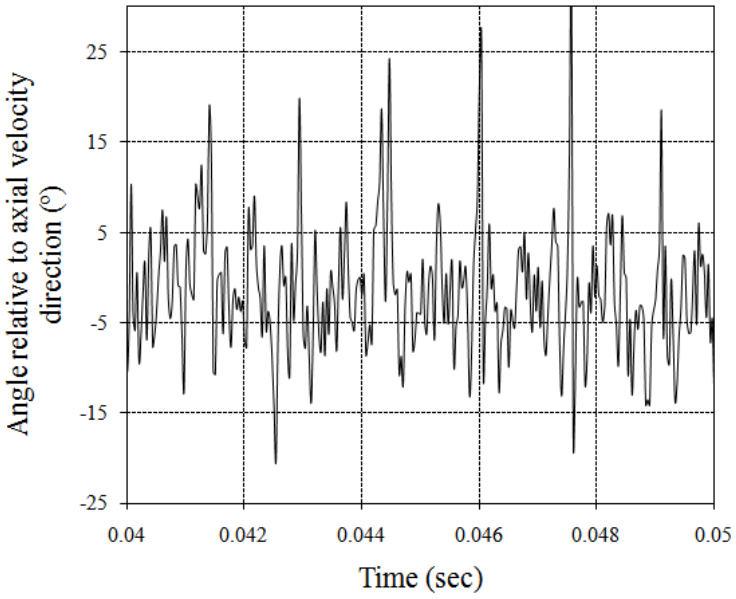

Figure M.12: Production nozzle velocity outflow angle near the nozzle outlet with a 650 Hz excitation and a supply mass flow rate of 23.8 x 10^{-3} kg/sec

M.4 1200 Hz excitation

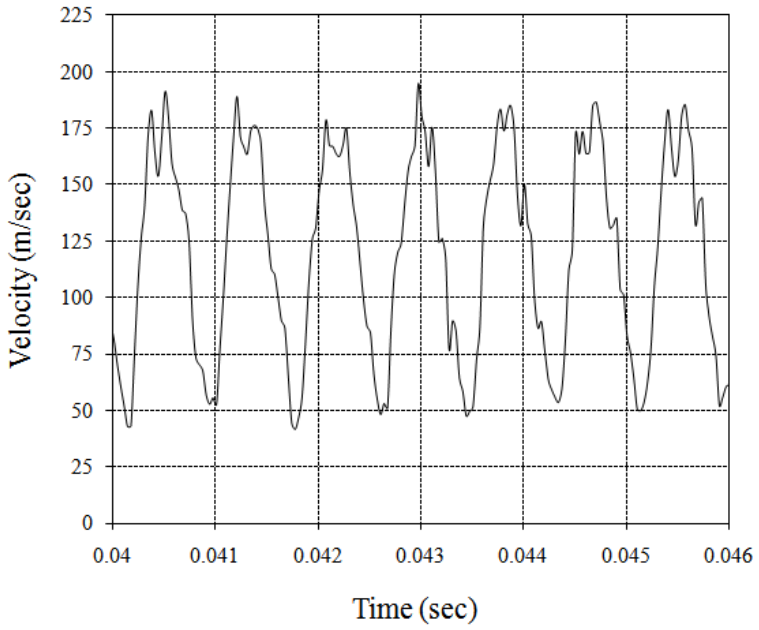

Figure M.13: Production nozzle velocity profile near the nozzle outlet with a 1200 Hz excitation and a supply mass flow rate of 23.8 x 10^{-3} kg/sec

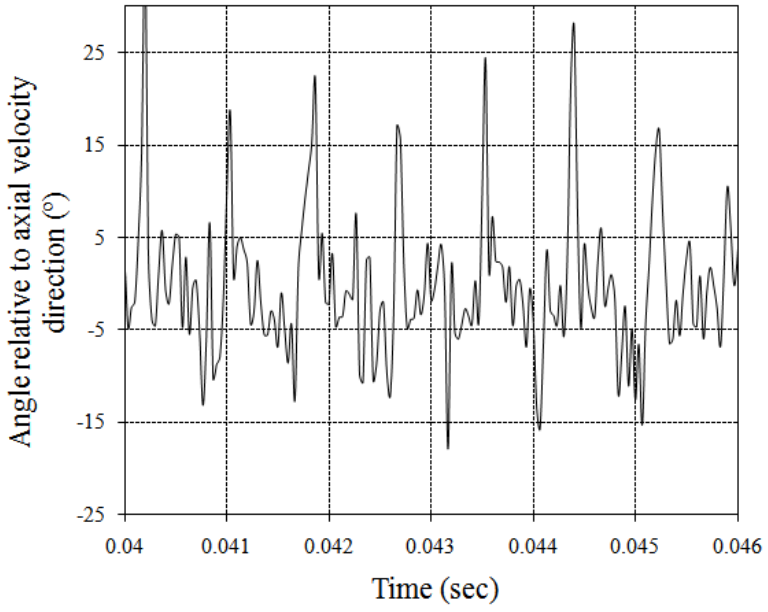

Figure M.14: Production nozzle velocity outflow angle near the nozzle outlet with a 1200 Hz excitation and a supply mass flow rate of 23.8 x 10^{-3} kg/sec

M.5 Axial nozzle

M.5.1 60 Hz excitation

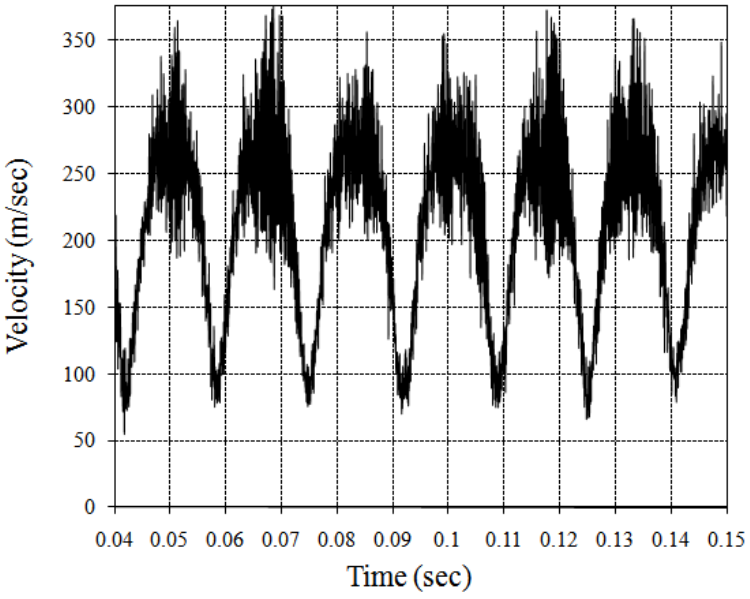

Figure M.15: Axial nozzle velocity profile near the nozzle outlet with a 60 Hz excitation and a supply mass flow rate of 23.8 x 10^{-3} kg/sec

M.5.2 650 Hz excitation

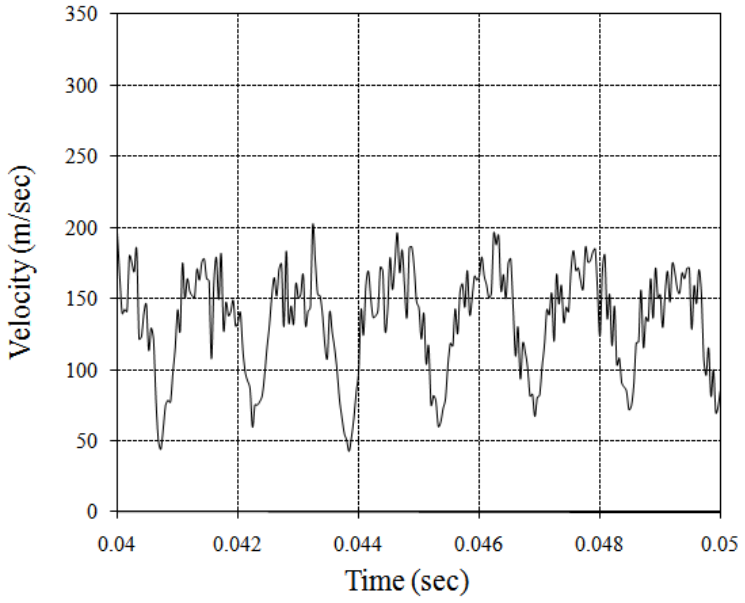

Figure M.16: Axial nozzle velocity profile near the nozzle outlet with a 650 Hz excitation and a supply a mass flow rate of 13.8 x 10^{-3} kg/sec

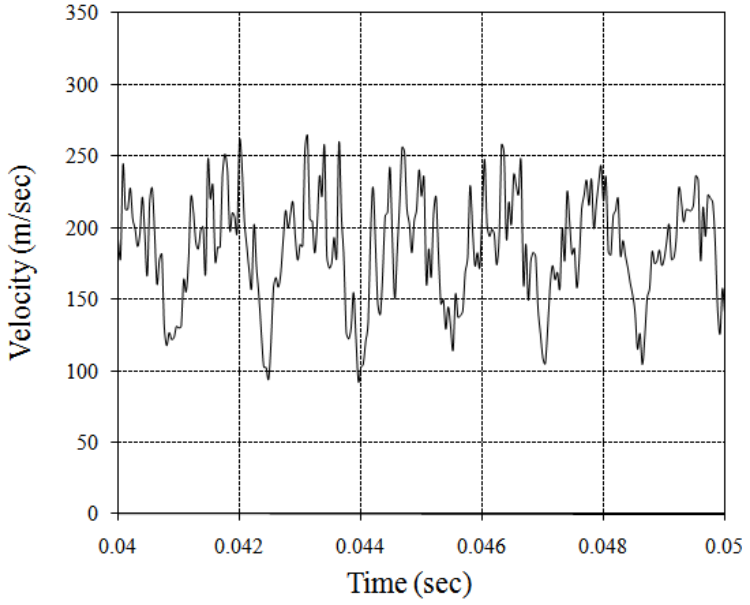

Figure M.17: Axial nozzle velocity profile near the nozzle outlet with a 650 Hz excitation and a supply mass flow rate of 19.9 x 10^{-3} kg/sec

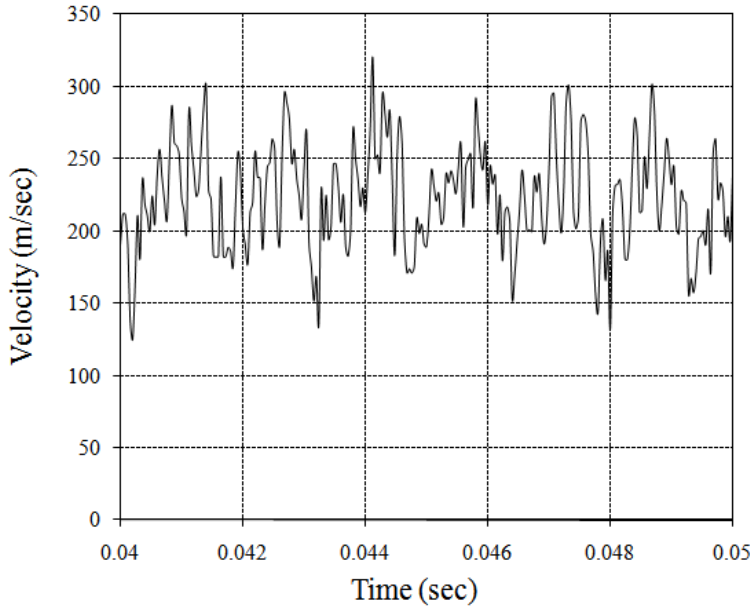

Figure M.18: Axial nozzle velocity profile near the nozzle outlet with a 650 Hz excitation and asupply mass flow rate of 23.8 x 10^{-3} kg/sec

M.6 1200 Hz excitation

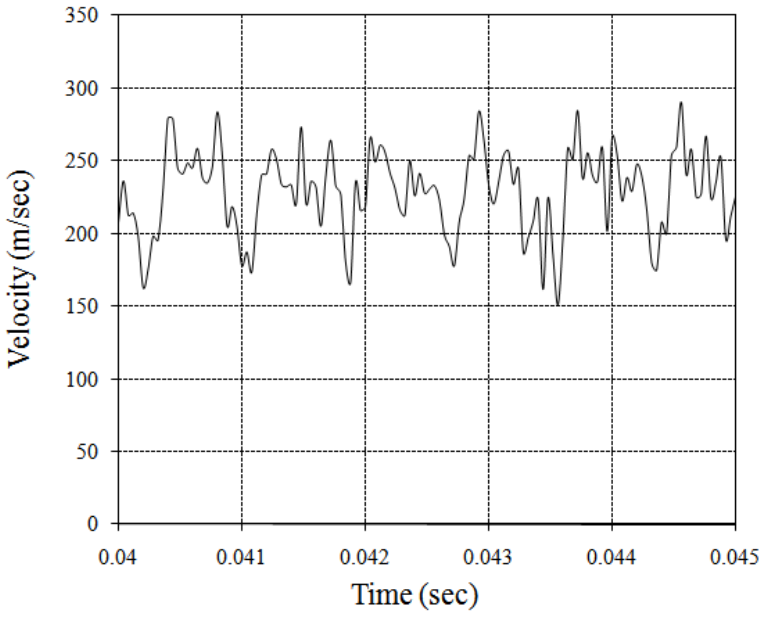

Figure M.19: Axial nozzle velocity profile near the nozzle outlet with a 1200 Hz excitation and a supply mass flow rate of 23.8 x 10^{-3} kg/sec

Appendix N

Mesh set-up detailed information

N.1 Axial mesh

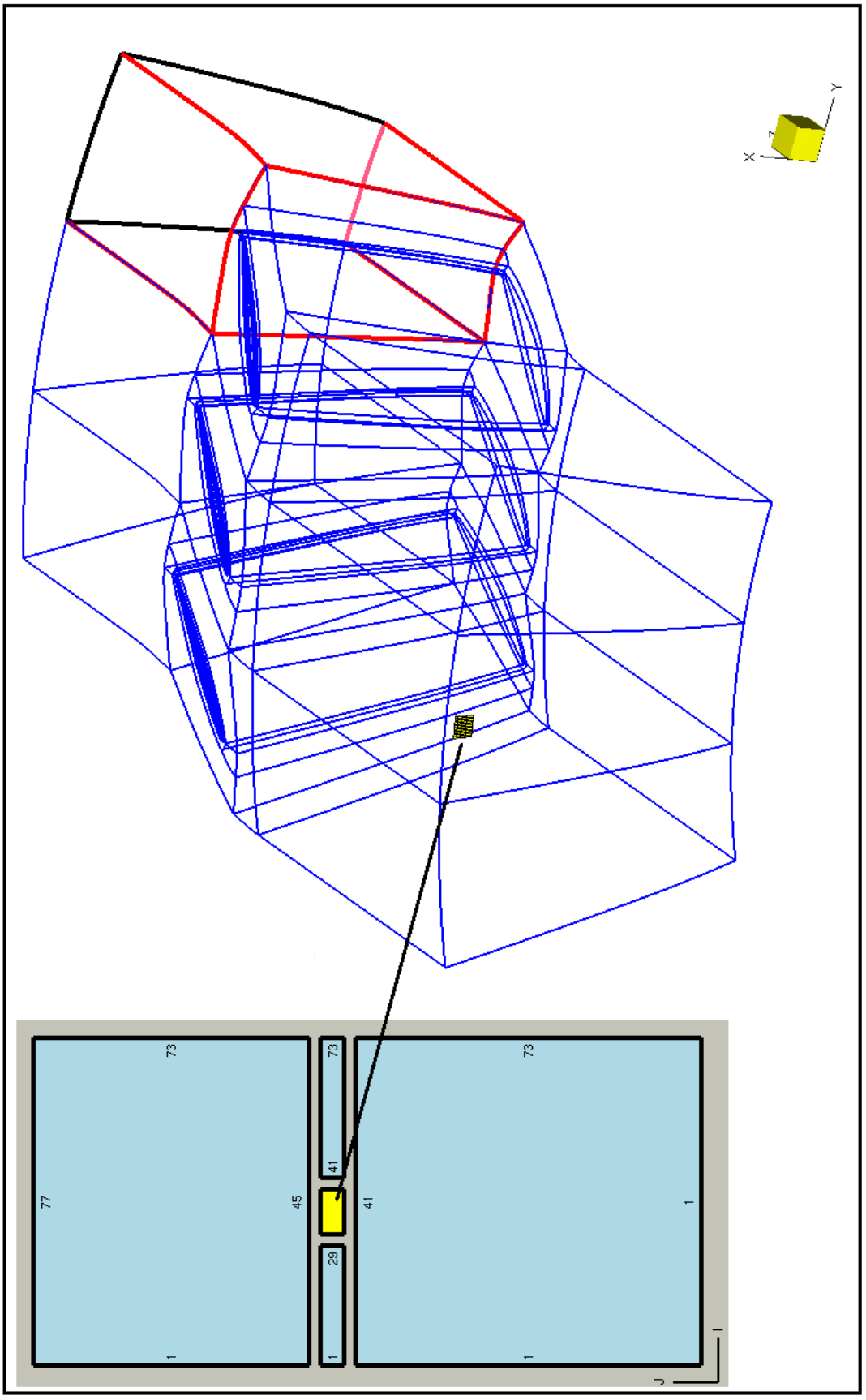

Figure N.1: Patch edit details for creation of axial injector inlet boundary condition

N.2 Production axial mesh

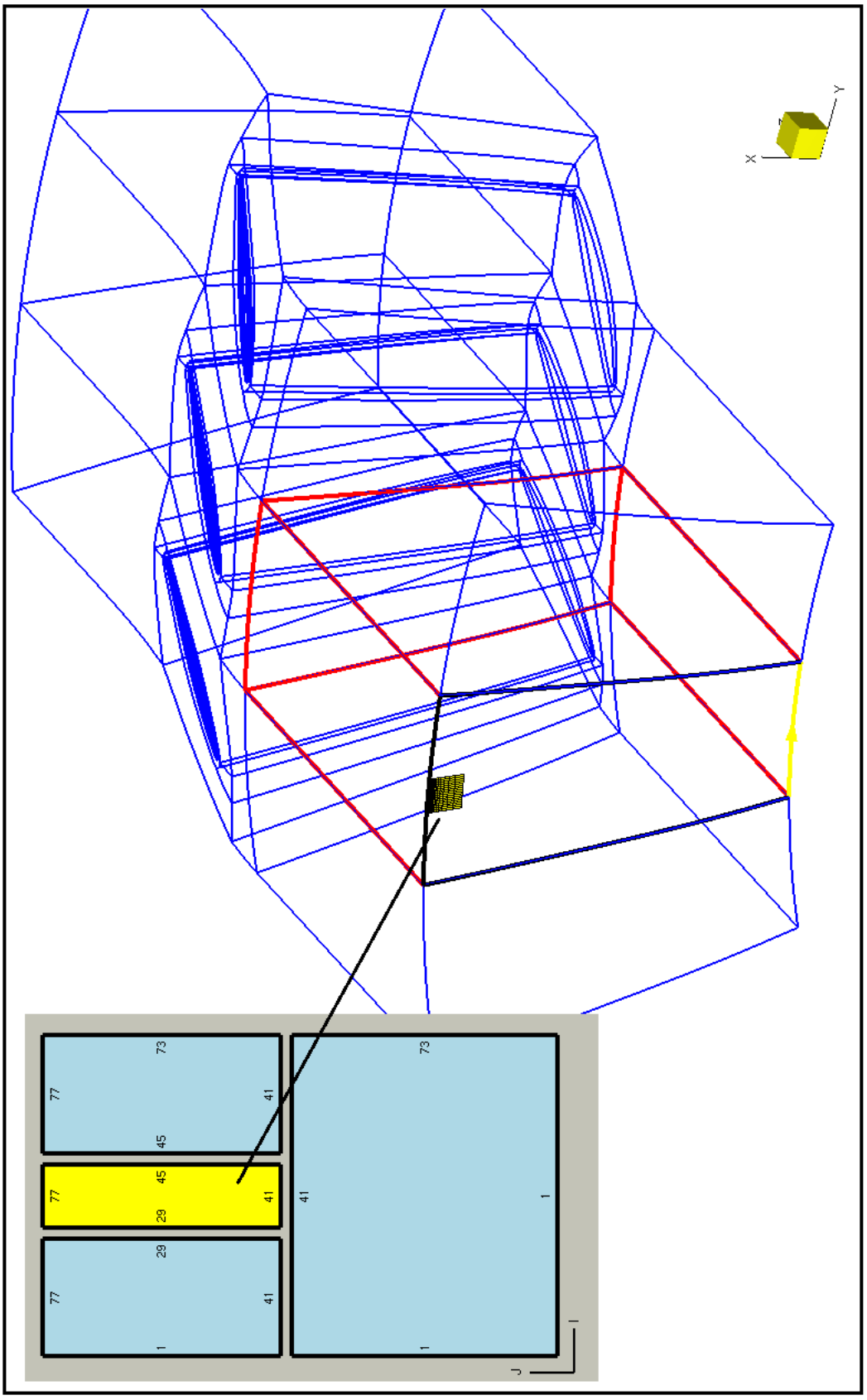

Figure N.2: Patch edit details for creation of production axial injector inlet boundary condition

N.3 Radial mesh

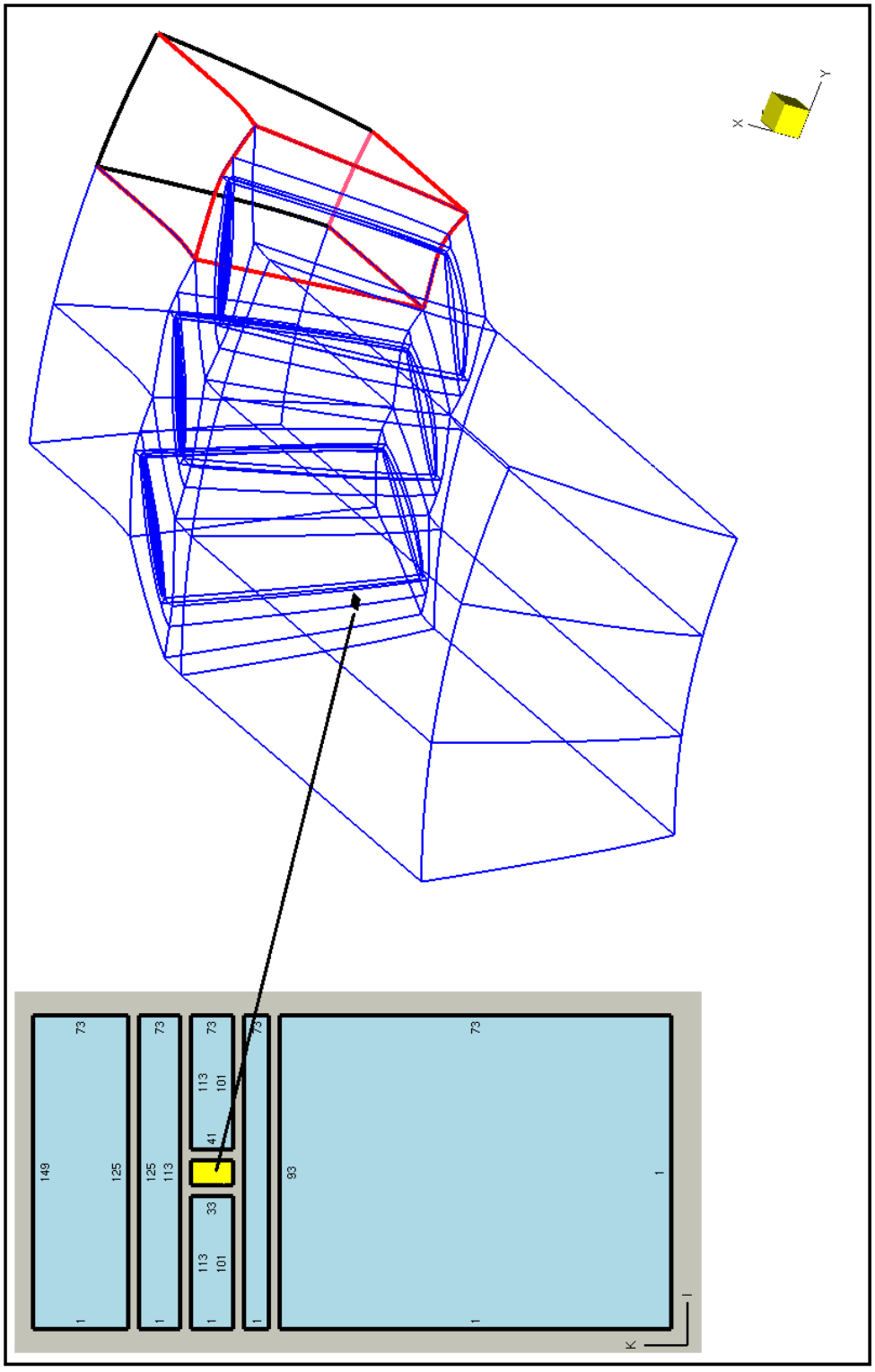

Figure N.3: Patch edit details for creation of radial injector inlet boundary condition

List of References

(2010 May). *Numeca FINE™/Turbo v8.7 User Manual*. Numeca International. Documentation v8b.

Agenbach, W. (1991). *Ontwerp van n generiese fladdermodel*. Master's thesis, Stellenbosch University.

Armstrong, E.K. and Stevenson, R.E. (1960). Some practical aspects of compressor blade vibration. *Journal of the Royal Aeronautical Society*, vol. 64.591, p. 20.

Ball, S., Ashforth-Frost, S., Jambunathan, K. and Whitney, C. (1999). Appraisal of a hot-wire temperature compensation technique for velocity measurements in non-isothermal flows. *International Journal of Heat and Mass Transfer*, vol. 42, pp. 3097–3102.

Brigham, E. (1988). *The Fast Fourier Transform and its applications*. Prentice Hall.

Cumpsty, N. (1989). *Compressor Aerodynamics*. Harlow.

Duvenhage, J. (2009). Die ontwerp en installering van 'n stelsel om fladder in 'n aksiaalrotor te meet. Tech. Rep., Stellenbosch University.

El-Aini, Y., deLaneuville, R., Soner, V. and Capeco, V. (1997). High-cycle fatigue of turbomachinery components - industry perspective. *AIAA*, vol. 97, p. 3365.

Ghouti, L., Adewusi, S., Al-Nassar, M. and Abdlsamad, M. (2003). Experiments on the extraction of blade vibration signature from the shaft torsion vibration signals. *Journal of Quality in Maintenance Engineering*, vol. 9.2, pp. 144–159.

Gill, A. (2006). *A comparison between stall prediction models for axial flow compressors*. Master's thesis, University of Stellenbosch.

Heath, S. and Imregun, M. (1996). An improved single-parameter tip-timing method for turbomachinery blade vibration measurements using optical laser probes. *International Journal of Mechanical Sciences*, vol. 38, p. 1047 to 1058.

Holzinger, F., Ostlund, J. and Martensson, H. (2008). *Excitation System Concepts*. Technische Universitat Darmstadt, Darmstadt. Technical report.

Japikse, D. and Baines, N. (1994). *Introduction to turbomachines*. Concept ETI Inc. and Oxford University Press.

Kayran, A. (2007). Flight flutter testing and aeroelastic stability of aircraft. *Aircraft Engineering and Aerospace Technology: An International journal*, vol. 79/5, pp. 494 – 506.

Kielb, R. (1998 January). Unsteady flows: An aeroelastic blade design perspective. In: *ERCOFTAC Turbomachinery Seminar and Workshop*. ERCOFTAC, Aussois, France.

Knappet, D. and Garcia, J. (2008). Blade tip timing and strain gauge correlation on compressor blades. In: *Proceedings of the Institution of Mechanical Engineers*, vol. Part G, pp. 497–506.

Lawson, C. and Ivey, P. (2005). Turbomachinery blade vibration amplitude measurement through tip timing with capacitance tip clearance probes. *Sensors and Actuators*, vol. 118.1, pp. 14–25.

Ravinesh, C., Mi, J. and Graham, J. (2007). The influence of nozzle-exit geometric profile on statistical properties of a turbulent plane jet. *Experimental Thermal and Fluid Science*, vol. 32, pp. 545–559.

Roos, T. (1995). *A prediction method for flow in axial compressors*. Master's thesis, University of Stellenbosch.

Sayers, A. (1990). *Hydraulic and Compressible Flow Turbomachines*. McGraw-Hill.

Scanlan, R. and Rosenbaum, R. (1951). *Introduction to the study of aircraft vibration and flutter*. The Macmillan Company.

Wegman, E., Van Zyl, L. and Rossouw, P. (2009). Project future deliverable report: Excitation system definition. Tech. Rep., CSIR.

White, R. and Walker, J. (1982). *Noise and Vibration*. Ellis Horwood Limited.